The Dissertation Committee for John Robert Dowdle
certifies that this is the approved version of the following dissertation:

Statistical Thermodynamics of Solvophobic Solvation in Water and Simpler Liquids

Committee:

Peter J. Rossky, Supervisor

Thomas M. Truskett

Dmitrii E. Makarov

Charles B. Mullins

Venkat Ganesan

Statistical Thermodynamics of Solvophobic Solvation in Water and Simpler Liquids

by

John Robert Dowdle, B.S., M.S.

DISSERTATION

Presented to the Faculty of the Graduate School of

The University of Texas at Austin

in Partial Fulfillment

of the Requirements

for the Degree of

DOCTOR OF PHILOSOPHY

THE UNIVERSITY OF TEXAS AT AUSTIN

December 2011

Dedicated to my loving wife, Erin

Acknowledgments

First, I would like to thank my advisor, Peter, for giving me the opportunity to pursue this work and for providing me with the guidance, resources, and criticism necessary to complete it. I have never met someone with a greater depth and breadth of scientific knowledge than Peter, nor have I known anyone with a more keen scientific intuition. His comments and criticisms always cut straight to the heart of the issue, and he always found a way to provide the criticism that I needed while also instilling in me the confidence required to keep going. It was a great privilege to work for someone as talented as Peter, and I will always be proud to say that I completed my dissertation under Peter Rossky.

My committee members and several chemical engineering professors were very helpful to me during my time in graduate school. I am especially grateful to Tom Truskett for meeting with me on several occasions, sharing ideas and insights into liquid state theory, and pointing me to useful literature. Several ideas in this dissertation arose from conversations I had with Tom. I am also grateful for the opportunity to help teach the graduate statistical thermodynamics course under Buddie Mullins. I learned a lot about teaching and scientific research in general from Buddie. I would also like to thank Professor Henry Ashbaugh of the Department of Chemical Engineering at

Tulane University for providing us with the results of his extensive calculations on cavity formation in the Lennard-Jones liquid.

I am of course very grateful to our financial sponsors. This work would not have been possible without the financial support of the National Science Foundation's Collaborative Research in Chemistry program. Additional financial support was provided by the Cockrell School of Engineering. In particular, I would like to thank Mr. W. A. "Tex" Moncrief, Jr. for his generous financial support.

Several members of the Rossky group contributed useful discussions, criticisms, and insights that benefitted my work. I am especially grateful to Richard Darst, who shared an immense amount of knowledge on computation, programming, and internet memes. Ashwin Dalvi was always willing to offer his thoughts on any scientific issues that arose, and I never ceased to be amazed at how regularly he produced profound and creative ideas. Silvina Matysiak and Adam Willard were especially knowledgeable of water and hydrophobicity, and I am grateful for the numerous discussions we shared. Lauren Kapcha and Adam Willard were particularly helpful in critiquing the presentation of my results. Many enjoyable office conversations, lunches, and coffee breaks were shared with group members including Mike Bedard-Hearn, Tyler Hone, Sangik Cho, Michelle Figgs, Fabio Sterpone, Adam Willard, Richard Darst, and Ashwin Dalvi. Most of all, I am grateful for the lasting friendships I have established with my Rossky group colleagues, and I feel truly privileged to have worked with such talented, motivated, and genuinely thoughtful people.

I have been very fortunate to have such a supportive and loving family. My parents in particular have been tremendously supportive in my academic endeavors, and I would never have made it here without them. From a young age they encouraged me to pursue my interests, and they always believed in me, even when I didn't believe in myself. I cannot thank them enough for their enduring love and support. I am also thankful for the good times I have had in Austin with my brother, Walt, my sister, Shellie, my brother-in-law, Lewis, and the girls—Kamrynn, Amanda, and Emory. It has been wonderful to be in Austin with all of them during my time in graduate school.

Most of all I would like to thank my wife, Erin. She has stood by my side unwaveringly throughout my journey through graduate school, which has covered two schools, over two thousand miles, and long, long time. She provided the primary financial support during our time here in Austin. Never once did I feel pressure from her; never once did she complain. None of this would have been possible without her dedication, love, and support. In addition, on July 14th, 2010, she gave birth to our precious baby girl, Shea Lynn. I look forward to every moment I will have with Erin, Shea, and our family, and I will be forever grateful for the devotion Erin has given to me over these years in graduate school.

Statistical Thermodynamics of Solvophobic Solvation in Water and Simpler Liquids

Publication No. _____

John Robert Dowdle, Ph.D.
The University of Texas at Austin, 2011

Supervisor: Peter J. Rossky

Temperature, pressure, and length scale dependence of the solvation of simple solvophobic solutes is investigated in the Jagla liquid, a simple liquid consisting of particles that interact via a spherically symmetric potential combining hard and soft core interactions. The results are compared with identical calculations for a model of a typical atomic liquid, the Lennard-Jones (LJ) potential, and with predictions for hydrophobic solvation in water using the recently developed cavity equation of state [6] and the extended simple point charge model [11].

We find that the Jagla liquid captures the qualitative thermodynamic behavior of hydrophobic hydration as a function of temperature and pressure for both small and large length scale solutes. In particular, for both the Jagla liquid and water, we observe temperature-dependent enthalpy and entropy of solvation for all solute sizes as well as a negative solvation entropy for sufficiently small solutes at low temperature. This feature of water-like solvation is

distinct from the strictly positive and temperature independent enthalpy and entropy of cavity solvation observed in the Lennard-Jones fluid. The results suggest that a competition between two energy scales that favors low-density, open structures as temperature is decreased is an essential interaction of a liquid that models hydrophobic hydration.

In addition the Jagla liquid dewets surfaces of large radii of curvature less readily than the Lennard-Jones liquid, and the so-called "length scale crossover" in solvation, whereby solvation free energies change from scaling with the solute volume to scaling with the solute surface area, occurs at length scales that are larger relative to the solvent size. Both features reflect a greater flexibility or elasticity in the Jagla liquid structure than that of a typical liquid, similar to water's ability to maintain its hydrogen bond network. The implications of the differences in crossover behavior between water-like and typical liquids are examined in the context of a simple thought experiment on the aggregation of solvophobic solutes that builds on ideas from Chandler [18] and Rajamani *et al.* [73]. We find that water-like crossover behavior exposes a size range of solvophobic aggregates to destabilization upon cooling and pressurizing, which may thereby precipitate phenomena such as cold and pressure denaturation of proteins.

Statistics of density fluctuations, void space, and pair distributions are analyzed for molecular-scale volumes. The pair distribution functions are used to provide an estimate of the size of the Jagla particle with a physical basis. The void distributions are observed to be distinct in the three liquids, with

low temperature distributions in the LJ and Jagla liquids demonstrating a high degree of skewness. The void distributions observed in LJ liquid are hard sphere-like, while those of water and the Jagla liquid exhibit a higher degree of density inhomogeneity relative to a hard sphere system. The well-known Gaussian behavior of density fluctuations in molecular volumes in water is not generally observed in other liquids, as evidenced by the fact that this behavior is not consistently observed in either the LJ or the Jagla liquids.

An exploratory study of the effects of explicit solvent on the sequence energy landscape of model heteropolymers has been performed. For a fixed set of configurations, the energy landscape of all possible sequences taken from a two letter alphabet consisting of only solvophilic and solvophobic monomers is characterized at different solvent temperatures. Non-trivial solvent and temperature effects are manifest in the distribution of sequences, confirming that the negation of these effects may have profound consequences on designability.

Contents

List of Tables

List of Figures

Chapter 1

Introduction

Among the many anomalous properties of liquid water is the solvation behavior of small apolar solutes, which is characterized at ambient conditions by an unfavorable entropy of transfer from vapor phase to water and an atypical decrease in solubility with increasing temperature. This behavior contrasts with typical solvents, which more readily accommodate apolar compounds as thermal fluctuations increase. The enthalpy of transfer for non-polar solutes to low-temperature water is actually negative and favorable, but the solubility is dominated by the entropic penalty. These characteristics change as a function of temperature and solute size. At sufficiently high temperatures the enthalpy is large and unfavorable and is only partially compensated for by favorable transfer entropies. Similarly, for sufficiently large solutes, the poor solubility is dominated by the unfavorable enthalpy associated with the formation of an interface, which overcomes the favorable entropy gain.

More generally, the unfavorable free energy change associated with the transfer of apolar solutes to water (and therefore the corresponding poor solubilities) results from the formation of the cavity volume required to accommodate the solute and the concomitant solvent structural changes in the so-

lute's vicinity (see Fig. 1.1). This process of cavity formation and solvent reorganization is known as hydrophobic hydration, and the affected solvent volume in the vicinity of the solute is referred to as the solvation shell. Hydrophobic solutes in solution experience a net force of attraction, known as the hydrophobic interaction, due to the reduction in solvation shell volume (and hence free energy) that is achieved by their association. The hydrophobic effect specifically refers to this tendency for apolar compounds to aggregate in solution, a process that is widely accepted to have critical importance in the self-assembly and stabilization of many biological structures including proteins and cell membranes [54, 88].

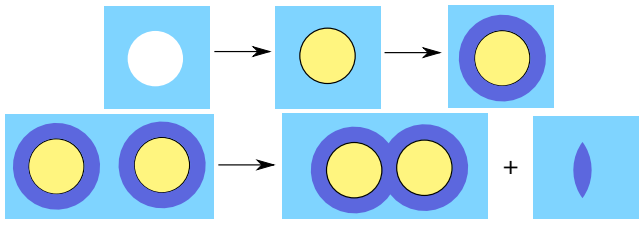

Figure 1.1: (*top*) Caricature of hydrophobic hydration of a simple hydrophobe and (*bottom*) hydrophobic association of a pair of hydrophobic solutes.

An extensive body of literature dating back to the early 20th century shows significant progress in the understanding of the fundamental features of hydrophobic phenomena and their role in biology (for a recent review, see [5]). Despite this rich literature on the subject, there is still much debate over the physical origins of hydrophobic behavior. Traditional views such as the "iceberg" picture of Frank and Evans [29], which attributes the negative entropies of transfer of small apolar solutes to increased ice-like structure and

hydrogen bonding in the solvation shell, have been brought into question by recent experimental and computational studies [5]. Consequently, claims about the relevance of the "iceberg" picture to hydrophobic phenomena such as the cold denaturation of globular proteins still generate lively debate [24, 25, 40].

Recent theoretical work has refocused attention in the field to the difference in size-dependence of the solvation free energy for small and large solutes [44–46, 61, 73]. Specifically, it was demonstrated that the solvation free energies of simple hard sphere solutes in water undergo a crossover in size dependence at about 1 nm. For solutes of size smaller than 1 nm, the solvation free energy scales with the volume of the solute, while for larger solutes it scales with the surface area. This crossover behavior, sketched in Fig. 1.2, is general to all liquids far from the critical point and near liquid-vapor coexistence, but the length scale of the crossover in water is greater than that of simple liquids like the Lennard-Jones (LJ) liquid [46]. This is attributed to water's propensity to create space throughout its hydrogen bonding network (Fig. 1.3).

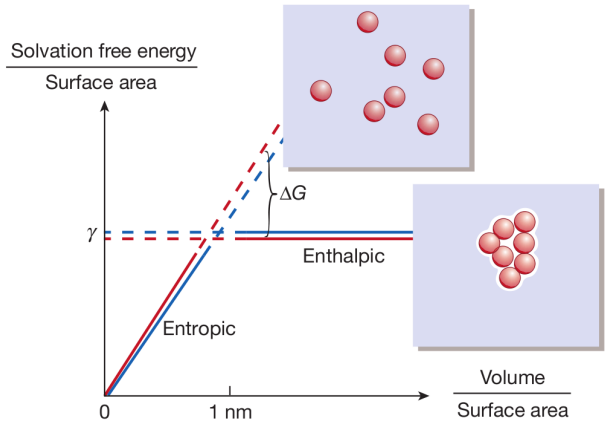

Figure 1.2: Qualitative representation of the so-called length scale crossover in solvation and the driving force for hydrophobic assembly (adapted from [18]). The solvation free energy scaled by the solute surface area is plotted versus the solute size. Red lines represent a warm temperature and blue lines indicate a cool temperature. γ is the liquid-vapor surface tension. For sufficiently large numbers of small solutes the aggregation free energy (ΔG) is negative and favorable.

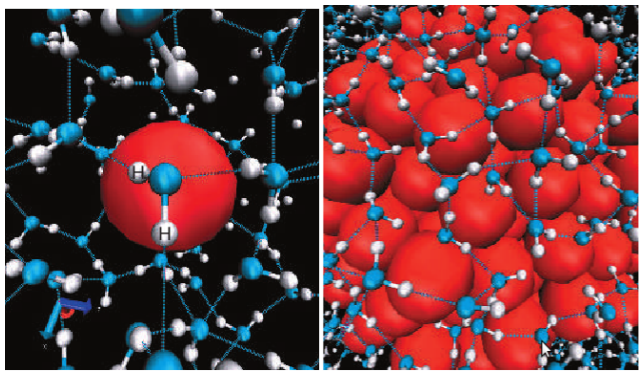

Figure 1.3: The structure of water near small and large hydrophobic solutes [18]. (*Left*) Small hydrophobes are able to fit in the available space of the liquid without causing water molecules to sacrifice hydrogen bonds. The solvation free energy in this case is mostly entropic. (*Right*) Extended hydrophobic surfaces however, such as that of a cluster of small hydrophobes, cause water molecules near the surface to break hydrogen bonds and reorganize. In this case, the solvation free energy is dominated by the enthalpy of interface formation.

Traditional explanations of hydrophobic behavior and water-like anomalies in general place emphasis on the orientational interactions of water molecules (hydrogen bonding) and the accompanying tendency for tetrahedral structure. However, a recently introduced family of spherically symmetric potentials consisting of two characteristic length scales (the Jagla model [52, 53]) has demonstrated thermodynamic, dynamic, and structural water-like anomalies [103, 104]. The Jagla model has also been shown to have water-like solvation thermodynamics [16]. In particular, the solubility of simple hard sphere solutes in the Jagla liquid is a non-monotonic function of the temperature, and furthermore, a polymer composed of such solutes has a solvent-induced collapsed state with a stability diagram in the pressure-temperature plane reminiscent

of that of a globular protein in water. These results confirm that orientational interactions are not necessary to produce these features of water-like solvation behavior and suggest that the presence of two competing length scales could be a fundamental physical feature of hydrophobic hydration.

Questions still remain however, about the similarities between solvation in the Jagla liquid and water. In particular, what are the energetic and entropic contributions to the solvation free energy in the Jagla liquid and are they similar to those of water? Over what length scales do the analogies in solvation behavior between the two liquids extend? Is the length scale crossover behavior in the Jagla liquid similar to other simple liquids, or does it also mimic that of water? And what, if anything, is common to the microscopic mechanisms governing water-like solvation behavior in the Jagla liquid and water? We address all of these questions in the following chapters.

In addition, we seek to remedy the curious dearth of systematic comparisons in the literature of apolar solvation phenomena in water with the same quantities in other small molecule liquids. We compare results for water and the Jagla liquid to results for the LJ liquid wherever possible. In doing so we hope to clarify what is indeed unique to water-like solvation and what is common in typical liquids.

Lastly, we will use the Jagla liquid as a proxy to investigate solvent effects on the problem of molecular design—that is, given a target structure of a molecule and an alphabet of monomer types, what is the sequence arrangement that produces a stable molecule with the desired structure? This problem is

one of the grand challenges of computational biology and protein engineering as well as materials science; its solution holds promise for far-reaching applications in areas ranging from materials assembly to targeted drug design. Due to its extraordinary computational complexity and scope, most models for the design problem have focused on coarse-grained implicit solvent effects through the use of effective contact potentials, which are in essence monomer-monomer potentials of mean force. One such model is the simple HP model of Lau and Dill [58], which consists of a two-letter alphabet of only hydrophobic and hydrophilic monomers. Hydrophobic pairs within a certain distance make a negative contribution to the overall system energy, and all other types of pair interactions are free energy neutral. Despite its simplicity, the HP model captures the main features of hydrophobic collapse: those sequences which permit the polymer to isolate hydrophobic interactions in the core form stable globular structures. Contact potentials such as those used in the HP model are valid at only one thermodynamic state however, since potentials of mean force are in general state-dependent [80]. Furthermore, it is known that potentials of mean force are not, in fact, pairwise-additive [94]. To gain understanding of the limitations of these assumptions, we seek to characterize the explicit effects of solvent-solute interactions on the sequence energy landscape of simple heteropolymers consisting of only solvophobic and solvophilic monomers in the Jagla solvent.

This dissertation is organized as follows. In Chapter 2 we derive the statistical thermodynamic framework for the analyses of solvophobic solva-

tion used in all subsequent chapters. In Chapter 3 solvation of small to large length scale solutes is investigated along the liquid-vapor coexistence curve of the Jagla liquid and compared to similar results for water and the LJ liquid. Molecular-scale density fluctuations and distribution functions of the aforementioned liquids are probed in detail in Chapter 4 in order to understand the similarities and differences in the microscopic mechanisms of solvation. In Chapter 5 we consider the length scale crossover and its relation to the thermodynamic stability of solvophobic aggregates. Chapter 6 investigates solvent effects on the sequence energy landscape of simple heteropolymers. Conclusions and future directions are given in Chapter 7.

Chapter 2

Solvation Thermodynamics

2.1 Introduction

The purpose of the present chapter is to introduce and precisely define the solvation quantities of interest in all subsequent studies presented in this dissertation. The notation and derivations closely follow the presentation given in recent papers by Ben-Amotz, Stell, and Widom [6–9]. We are most interested in the chemical potential of the solute, since all solvation thermodynamic functions can be obtained from the chemical potential and its derivatives. For simplicity, we will be concerned with the solvation of idealized spherical solutes with no internal degrees of freedom. Hence, the following derivations do not address any effects of the solvation process on internal degrees of freedom. The chemical potential is defined and its related thermodynamic functions are derived in Section 2.2. Solubility is defined in Section 2.3 and its temperature dependence is expressed in terms of the solvation thermodynamic functions. The case of cavity (purely repulsive, hard-core) solutes is considered in Section 2.4 and first-order perturbation theory corrections for weak attractive interactions are derived in Section 2.5.

2.2 The Chemical Potential at Infinite Dilution and Related Thermodynamic Functions

Consider a two-component system consisting of N_u molecules of a dilute solute, labeled u, and N_v molecules of a solvent, labeled v, at some fixed temperature, T, and volume, V (*i.e.*, in the canonical ensemble). At infinite dilution the chemical potential of the solute is

$$\begin{aligned}\mu_u &\equiv \lim_{N_u \to 0} \left\{ \left(\frac{\partial A}{\partial N_u} \right)_{T,V,N_v} \right\} \\ &= A(T, V, N_v, N_u = 1) - A(T, V, N_v, N_u = 0),\end{aligned} \tag{2.1}$$

where A is the Helmholtz free energy of the system and the last equality assumes the thermodynamic limit. The excess chemical potential is

$$\begin{aligned}\mu_u^x &\equiv \lim_{N_u \to 0} \left\{ \left(\frac{\partial A^x}{\partial N_u} \right)_{T,V,N_v} \right\} \\ &= A^x(T, V, N_v, N_u = 1) - A^x(T, V, N_v, N_u = 0),\end{aligned} \tag{2.2}$$

where

$$A^x(T, V, N_v, N_u) = A(T, V, N_v, N_u) - A^{(ig)}(T, V, N_v, N_u) \tag{2.3}$$

and $A^{(ig)}(T, V, N_v, N_u)$ is the ideal gas (ig) limit in which all interparticle interactions are "turned off" while the volume, composition and temperature are fixed. Hence, $\mu_u^x = \mu_u - \mu_u^{(ig)}$ represents the contribution to the chemical potential due to "turning on" all intermolecular interactions. The translational degrees of freedom of the solute are not affected by this process. Assuming in addition that the internal degrees of freedom are not affected, μ_u^x becomes

identical to Ben-Naim's solvation free energy, $\Delta\mu^*$, for transferring a *stationary* solute from an ideal gas phase to a condensed phase [10].

Following Widom's potential distribution theorem and decomposing the configurational energy of the system as $U = \Phi + \Psi$, where Φ is the total potential energy of all solvent-solvent interactions and Ψ is the total potential energy of all solute-solvent interactions, we may also write the excess chemical potential as [7, 97, 99]

$$\mu_u^x = -k_B T \ln \mathbf{B}_u = -k_B T \ln \langle e^{-\beta\Psi} \rangle_0 = k_B T \ln \langle e^{\beta\Psi} \rangle. \tag{2.4}$$

Here, $\beta = 1/k_B T$ where k_B is Boltzmann's constant, and the notation $\langle \dots \rangle_0$ indicates an ensemble average taken under the condition that the solvent molecules do not interact with the solute, while the absence of a subscript indicates the usual ensemble average taken with all molecules fully coupled. The quantity $\mathbf{B}_u \equiv \langle e^{-\beta\Psi} \rangle_0 = 1/\langle e^{\beta\Psi} \rangle$ is called the "insertion factor" and governs the solvation thermodynamics. The latter equality of Eq. (2.4) may be written as

$$\mu_u^x = \langle \Psi \rangle + k_B T \ln \langle e^{\beta\delta\Psi} \rangle = \epsilon_\mu - T s_\mu, \tag{2.5}$$

where $\delta\Psi \equiv \Psi - \langle \Psi \rangle$ is the fluctuation of the solute-solvent interaction energy from its mean value. Notice that since $\langle e^x \rangle \geq e^{\langle x \rangle}$, it follows that $\langle e^{\beta\delta\Psi} \rangle = \langle e^{\beta\Psi} \rangle / e^{\langle \beta\Psi \rangle} \geq 1$. Hence, the excess entropy associated with solute-solvent energy fluctuations, $s_\mu = -k_B \ln \langle e^{\beta\delta\Psi} \rangle$, is necessarily negative, raising the free energy, whereas the mean solute-solvent interaction energy, $\langle \Psi \rangle$, is usually (but not necessarily) negative and favorable.

For a constant volume solvation process, the excess solvation energy, $\epsilon_u^x|_V$, may be derived from μ_u^x by using the Gibbs-Helmholtz relation and Eq. (2.2)

$$\begin{aligned}
\epsilon_u^x|_V &= \left[\frac{\partial \beta \mu_u^x}{\partial \beta}\right]_{V,N_v,N_u} \\
&= \langle U \rangle - \langle U \rangle_0 \\
&= \langle \Phi + \Psi \rangle - \langle \Phi \rangle_0 \\
&= \langle \Psi \rangle + \langle \Phi \rangle - \langle \Phi \rangle_0 \\
&= \langle \Psi \rangle + \Delta \langle \Phi \rangle|_V, \qquad (2.6)
\end{aligned}$$

where the quantity $\Delta\langle\Phi\rangle|_V \equiv \langle\Phi\rangle - \langle\Phi\rangle_0 = \epsilon_u^x|_V - \epsilon_\mu$ is the constant volume solvent reorganization energy, representing the solute-induced changes in the solvent-solvent interaction energies. Noting that $Ts_u^x|_V = \epsilon_u^x|_V - \mu_u^x$ and combining the result of Eq. (2.6) with Eq. (2.4) and Eq. (2.5) we obtain the following expressions for the constant volume solvation entropy

$$\begin{aligned}
Ts_u^x|_V &= \langle \Psi \rangle + \Delta \langle \Phi \rangle|_V + \frac{1}{\beta} \ln \langle e^{-\beta \Psi} \rangle_0 \\
&= \Delta \langle \Phi \rangle|_V - \frac{1}{\beta} \ln \langle e^{\beta \delta \Psi} \rangle. \qquad (2.7)
\end{aligned}$$

It should be emphasized that although the solvent reorganization energy appears explicitly in both the expression for the solvation energy and for the solvation entropy, it cancels when combining the two terms to obtain μ_u^x. That is, the solvent reorganization energy does not contribute to the solvation free energy, a result first derived by Yu and Karplus and subsequently derived by others [7, 10, 41, 85, 105]. Thus, the driving force for hydrophobicity is purely

a solute-solvent effect. As we shall see, however, the solvent reorganization energy plays a key role in the temperature dependence of the solubility.

If the solvation process is carried out at constant pressure, then there is in general a change in system volume upon accommodation of the solute. This is the partial molar volume, and it is expressed as

$$v_u \equiv \left(\frac{\partial \mu_u}{\partial P}\right)_{T,N_v,N_u} = \langle V \rangle - \langle V \rangle_0. \tag{2.8}$$

We may further write

$$\begin{aligned} v_u &= \left(\frac{\partial \mu_u}{\partial P}\right)_T = \left(\frac{\partial \mu_u}{\partial \rho}\right)_T \left(\frac{\partial \rho}{\partial P}\right)_T = \kappa_T \rho \left(\frac{\partial \mu_u}{\partial \rho}\right)_T \\ &= \kappa_T \left[\rho \left(\frac{\partial \mu_u^x}{\partial \rho}\right)_T + k_B T\right] = v_u^x + v_u^{(ig)} \end{aligned} \tag{2.9}$$

where ρ is the solvent number density, $\kappa_T = 1/\rho \left(\partial \rho / \partial P\right)_T$ is the isothermal compressibility of the fluid, $v_u^x = \kappa_T \rho \left(\partial \mu_u / \partial \rho\right)_T$ is the partial molar volume of a stationary solute in the fluid phase, and $v_u^{(ig)} = \kappa_T k_B T$ is the additional volume obtained by liberating the particle's translational motion. In the second to last equality of Eq. (2.9) we have assumed the translational degrees of freedom may be treated classically so that $\mu_u^{(ig)} = k_B T \ln\left\{\rho_u \Lambda_u^3\right\} = k_B T \ln\left\{x_u \rho \Lambda_u^3\right\}$, where x_u is the solute number fraction and $\Lambda_u = h/\sqrt{2\pi m_u k_B T}$ is the thermal de Broglie wavelength, where h is Planck's constant, and m_u is the mass of the solute.

The solvent reorganization energy for a constant pressure solvation process differs from that for a constant volume process by the energy associated

with a volume relaxation at constant pressure. Specifically, for a stationary solute,

$$\Delta\langle\Phi\rangle|_P - \Delta\langle\Phi\rangle|_V = \left(\frac{\partial U}{\partial V}\right)_T v_u^x = \left[T\left(\frac{\alpha_P}{\kappa_T}\right) - P\right] v_u^x, \tag{2.10}$$

where $(\partial U/\partial V)_T = T\alpha_P/\kappa_T - P$ is the internal pressure of the solvent and, $\kappa_T = -1/V\,(\partial V/\partial P)_T$, and $\alpha_P = 1/V\,(\partial V/\partial T)_P$ is the thermal expansivity of the solvent. Using this result, we may write the excess solvation energy in a constant-pressure system as

$$\begin{aligned}\epsilon_u^x|_P &= \langle U\rangle - \langle U\rangle_0 \\ &= \langle\Psi\rangle + \Delta\langle\Phi\rangle|_P \\ &= \langle\Psi\rangle + \Delta\langle\Phi\rangle|_V + (T\frac{\alpha_P}{\kappa_T} - P)v_u^x. \end{aligned}\tag{2.11}$$

Hence, the excess enthalpy of solvation at constant pressure is

$$\begin{aligned}h_u^x|_P &= \epsilon_u^x|_P + Pv_u^x = \langle\Psi\rangle + \Delta\langle\Phi\rangle|_P + Pv_u^x \\ &= \langle\Psi\rangle + \Delta\langle\Phi\rangle|_V + T\frac{\alpha_P}{\kappa_T}v_u^x, \end{aligned}\tag{2.12}$$

and, using $Ts_u^x|_P = h_u^x|_P - \mu_u^x$, the excess entropy for a constant pressure process is

$$\begin{aligned}Ts_u^x|_P &= \langle\Psi\rangle + \Delta\langle\Phi\rangle|_P + Pv_u^x + k_BT\ln\langle e^{-\beta\Psi}\rangle_0 \\ &= \Delta\langle\Phi\rangle|_P + Pv_u^x - k_BT\ln\langle e^{\beta\delta\Psi}\rangle. \end{aligned}\tag{2.13}$$

Most experimental measurements of solubility are carried out at constant pressure along the liquid-vapor coexistence curve (also known as the saturation curve, binodal line, or orthobaric path) of the solvent, a locus of

states which we will denote by σ. This is also the set of states explored in the theoretical studies of solvation in Chapters 3 and 4 of this document. Temperature derivatives along the saturation curve may be related to those at constant pressure through the state variable relation [74]

$$\left(\frac{\partial \mu_u^x}{\partial T}\right)_\sigma = \left(\frac{\partial \mu_u^x}{\partial T}\right)_P + \left(\frac{\partial \mu_u^x}{\partial P}\right)_T \left(\frac{\partial P}{\partial T}\right)_\sigma . \tag{2.14}$$

Noting that $(\partial \mu_u^x / \partial P)_T = v_u^x$ we may write

$$s_u^x|_\sigma = -\left(\frac{\partial \mu_u^x}{\partial T}\right)_\sigma = s_u^x|_P - v_u^x \left(\frac{\partial P}{\partial T}\right)_\sigma . \tag{2.15}$$

Similarly,

$$h_u^x|_\sigma = \left(\frac{\partial \beta \mu_u^x}{\partial \beta}\right)_\sigma = h_u^x|_P - T v_u^x \left(\frac{\partial P}{\partial T}\right)_\sigma . \tag{2.16}$$

2.3 Equilibrium Partitioning Thermodynamics and Solubility

Consider the process of transferring a solute molecule (u) between liquid (l) and vapor (v) phases at equilibrium. From the conditions for equilibrium we must have equivalence between the chemical potentials of the solute in each of the two phases, *i.e.*,

$$\mu^{(l)} = \mu^{(v)}. \tag{2.17}$$

Following the definitions in Section 2.2, the total chemical potential of the solute u in phase α may be written

$$\mu_u^{(\alpha)} = k_B T \ln \{\rho_u^{(\alpha)} \Lambda_u^3\} + \mu_u^{x,(\alpha)} \tag{2.18}$$

where $\rho_u^{(\alpha)}$ is the solute number density in the α-phase, and $\mu_u^{x,(\alpha)}$, is the α-phase excess chemical potential as defined in Section 2.2. The first term on the RHS of Eq. (2.18) and arises from an integration over the classical Boltzmann distribution of momenta. Therefore, Eq. (2.18) is valid only for systems where the translational degrees of freedom may be treated classically, which applies to all of the systems of interest in the studies presented here. Substituting Eq.'s (2.4) and (2.18) into Eq. (2.17) one arrives at the following equivalent equilibrium condition

$$L \equiv \frac{\rho_u^{(l)}}{\rho_u^{(v)}} = \frac{\mathbf{B}_u^{(l)}}{\mathbf{B}_u^{(v)}} = \exp\left\{-\beta\left[\mu_u^{x,(l)} - \mu_u^{x,(v)}\right]\right\}, \tag{2.19}$$

where the quantity L is known as the Ostwald coefficient, which is a common experimental measure of solubility.

If the vapor phase may be assumed ideal, then $\mu_u^{x,(v)} = 0$ and $L = \mathbf{B}_u^{(l)} = \exp\left\{-\beta(\mu_u^{x,(l)})\right\} \equiv \gamma$. In this case, γ is often referred to as the "solubility parameter", and solubilities are reported as [41]

$$\ln\gamma = -\beta\mu_u^{x,(l)}. \tag{2.20}$$

Thus, a solute could be termed "hydrophobic" if $\ln\gamma$ is negative and "hydrophilic" if $\ln\gamma$ is positive.

Also note that under ideal vapor conditions the solute number density in the vapor phase is given by the ideal gas law

$$\rho_u^{(v)} = \beta y_u P = \beta P_u, \tag{2.21}$$

where y_u is the solute number fraction in the vapor phase and P_u is the corresponding partial pressure. The aqueous solute number density is then given by Henry's law

$$\rho_u^{(l)} = \mathbf{B}_u^{(l)} \beta P_u. \tag{2.22}$$

This equation provides the basis for a second common experimental measure of solubility, Henry's constant, k_H, which is defined as the ratio of the partial pressure of the solute in the vapor phase, P_u to the concentration in the liquid phase, c_u,

$$k_H \equiv \frac{P_u^{(exp)}}{c_u^{(exp)}} = \frac{f P_u}{\rho_u^{(l)}} = \frac{f}{\beta \mathbf{B}_u^{(l)}} = \frac{f k_B T}{L}. \tag{2.23}$$

Here, f is a constant that relates units between the quantities defined here and experimentally measured (exp) quantities. (Note that Henry's "constant" is actually a function of temperature).

The temperature dependence of the solubility may be seen in the temperature derivatives of the aforementioned measures, *viz.*,

$$\begin{aligned} \left(\frac{\partial \ln \gamma}{\partial T}\right)_\sigma &= \frac{\mu_u^x}{k_B T^2} - \frac{1}{k_B T}\left(\frac{\partial \mu_u^x}{\partial T}\right)_\sigma = \frac{h_u^x|_\sigma}{k_B T^2} \\ &= \frac{\langle \Psi \rangle + \Delta \langle \Phi \rangle|_P}{k_B T^2} + \frac{v_u^x}{k_B T^2}\left[P - T\left(\frac{\partial P}{\partial T}\right)_\sigma\right], \end{aligned} \tag{2.24}$$

and

$$-\left(\frac{\partial \ln k_H}{\partial T}\right)_\sigma = \left(\frac{\partial \ln \gamma}{\partial T}\right)_\sigma - \frac{1}{T}. \tag{2.25}$$

For molecular-sized solutes at ambient conditions, v_u^x and P are sufficiently small that

$$\left(\frac{\partial \ln \gamma}{\partial T}\right)_\sigma \simeq \frac{\langle \Psi \rangle + \Delta \langle \Phi \rangle|_P}{k_B T^2}. \tag{2.26}$$

Thus, we see that the characteristic decrease in solubility with increasing temperature for small hydrophobes in water at ambient conditions may only occur if $\langle\Psi\rangle + \Delta\langle\Phi\rangle|_P < 0$.

2.4 The Special Case of Cavity / Hard Sphere Solutes

In all of the studies in the following chapters, we seek to characterize the equilibrium solvation properties of solvophobic solutes, where the term "solvophobic" means here that the solute is less attracted to the solvent than the solvent is attracted to itself. The simplest model of a solvophobic solute is a hard sphere, or equivalently, a spherical region of radius

$$R = (\sigma_c + \sigma_v)/2 \tag{2.27}$$

devoid of solvent centers, henceforth referred to as a cavity and denoted by a subscript c. Here, σ_v is the effective solvent hard core diameter and σ_c is the solute hard sphere diameter. Eq. (2.27) establishes the correspondence between hard sphere and cavity solutes depicted in Fig. (2.1).

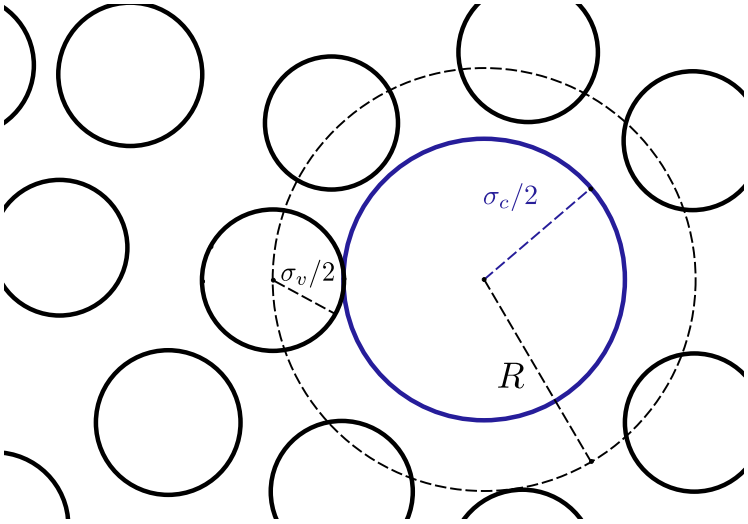

Figure 2.1: A two-dimensional system showing a cavity solute with a hard sphere diameter of σ_c in a solvent with an effective hard sphere diameter σ_v. The distance of closest approach is the cavity radius, R.

For a cavity solute the hard sphere interaction ensures that $\langle \Psi \rangle = 0$, and thus μ_c^x is entirely entropic in origin and strictly positive. Moreover, since Ψ is either infinity or zero in the uncoupled ensemble (either there is overlap of hard sphere radii or not), the insertion factor reduces to $p_0(R)$, the probability of finding exactly zero solvent centers in a spherical volume of radius R. With these simplifications, the following equations summarize the results for excess solvation properties of interest derived in Section 2.2 for the case of cavity

solutes:

$$\mu_c^x = -k_B T \ln p_0(R) = -T s_\mu, \tag{2.28}$$

$$\epsilon_c^x|_P = \Delta\langle\Phi\rangle|_P = \langle U\rangle - \langle U\rangle_0, \tag{2.29}$$

$$v_c^x = v_c - k_B T \kappa_T = \langle V\rangle - \langle V\rangle_0 - k_B T \kappa_T, \tag{2.30}$$

$$h_c^x|_P = \epsilon_c^x|_P + P v_c^x = \Delta\langle\Phi\rangle|_P + P v_c^x, \tag{2.31}$$

$$T s_c^x|_P = \Delta\langle\Phi\rangle|_P + P v_c^x - \mu_c^x, \tag{2.32}$$

$$T s_c^x|_\sigma = -\left(\frac{\partial \mu_c^x}{\partial T}\right)_\sigma = T s_c^x|_P - T v_c^x \left(\frac{\partial P}{\partial T}\right)_\sigma, \tag{2.33}$$

$$h_c^x|_\sigma = \left(\frac{\partial \beta \mu_c^x}{\partial \beta}\right)_\sigma = h_c^x|_P - T v_c^x \left(\frac{\partial P}{\partial T}\right)_\sigma \tag{2.34}$$

It is important to emphasize again that these solvation quantities are associated with the transfer of a *stationary* solute from the ideal gas phase into the fluid phase. In addition, note that for molecular-sized cavity solutes [see Eq. (2.26)]

$$\left(\frac{\partial \ln \gamma}{\partial T}\right)_\sigma \simeq \frac{\Delta\langle\Phi\rangle|_P}{k_B T^2}. \tag{2.35}$$

Thus, the solubility of such small cavity solutes can be a non-monotonic function of temperature if and only if $\Delta\langle\Phi\rangle|_P$ changes sign. However, for transfer from an ideal vapor, $\Delta\langle\Phi\rangle|_P$ is expected to be always positive [62].

2.5 Mean-Field Theory for Weak Attractive Interactions

To create a more realistic picture of solvophobic solvation, we will be interested in adding small corrections to the solvation free energy of dilute cavity solutes to model realistic solutes with weak attractive interactions. Here,

we will only consider the specific case of spherically symmetric solute and solvent particles with pairwise-additive interaction potentials. Further, we consider the case that the solute-solvent pair interaction energy, $\Psi(r)$, may be separated using a Weeks-Chandler-Andersen decomposition [96] into a purely repulsive cavity term (c) and a purely attractive (a) term

$$\Psi(r) = \Psi^c(r) + \Psi^a(r), \tag{2.36}$$

where

$$\Psi^c(r) = \begin{cases} \Psi(r) - \Psi(r_0) = \infty, & r \leq r_0 \\ 0, & r > r_0, \end{cases} \tag{2.37}$$

$$\Psi^a(r) = \begin{cases} \Psi(r_0), & r \leq r_0 \\ \Psi(r), & r > r_0, \end{cases} \tag{2.38}$$

and r_0 is the location of the minimum in $\Psi(r)$. The excess chemical potential may then be calculated from [99, 107]

$$\exp\left[-\frac{(\mu_u^x - \mu_c^x)}{k_B T}\right] = \left\langle \exp\left(\frac{-\Psi^a}{k_B T}\right)\right\rangle, \tag{2.39}$$

where the ensemble average is taken in the cavity reference system. Expanding Eq. (2.39) in terms of cumulants of the Ψ^a distribution in the reference ensemble yields

$$\mu_u^x = \mu_c^x + \langle \Psi^a \rangle + \ldots \tag{2.40}$$

For weak attractions, we expect only the first two terms to contribute significantly. Taking advantage of the spherical symmetry we may write the attractive contribution in Eq. (2.40) as [7]

$$\langle \Psi^a \rangle = \rho \int_0^\infty dr 4\pi r^2 \Psi^a(r) g_{cv}(r), \tag{2.41}$$

where $g_{cv}(r)$ is the cavity-solvent pair correlation function. Thus, the procedure to add weak attractive corrections to cavity solvation free energy requires only the knowledge of the functional form of the attractive interactions, Ψ^a, and the cavity-solvent pair correlation function.

2.6 Conclusions

The excess chemical potential of a dilute solute was defined for the process of transferring a stationary solute from an ideal phase into a fluid phase. Temperature derivatives of the excess chemical potential were related to solvation thermodynamic functions such as the enthalpy and the entropy. The simplifications of the solvation functions for the case of cavity solutes were outlined, and weak attractive contributions to the free energy were derived.

Chapter 3

Cavity Formation Along the Saturation Curve

3.1 Introduction

The decreasing solubility of small apolar solutes with increasing temperature is one of the well-known peculiarities of hydrophobic solvation. Traditional explanations of hydrophobic behavior and water-like anomalies in general place emphasis on the orientational interactions of water molecules (hydrogen bonding) and the accompanying tendency to adopt tetrahedral structures at low temperatures. However, a recently introduced family of spherically symmetric potentials consisting of two characteristic length scales (the Jagla model [52, 53]) has demonstrated thermodynamic, dynamic, and structural water-like anomalies [103, 104]. The Jagla model has also been shown to have water-like solvation thermodynamics [16]. In particular, the solubility of simple hard sphere solutes in the Jagla liquid is a non-monotonic function of the temperature, and furthermore, a polymer composed of such solutes has a solvent-induced collapsed state with a stability diagram in the pressure-temperature plane similar to that of a globular protein in water. These results confirm that orientational interactions are not a prerequisite for water-like solvation behavior and suggest that the presence of two competing length scales could be a fundamental physical feature of hydrophobic hydration.

In this chapter we present the results of extensive Monte Carlo (MC) simulations of cavity formation in the Jagla liquid and address some of the remaining questions regarding the similarities between solvophobic solvation in the Jagla liquid and water. Specifically, cavity solvation free energies and corresponding entropic and enthalpic contributions are calculated along the saturation curve of the Jagla liquid for cavities ranging in diameter from one to six times the size of the Jagla particle. A separate set of MC simulations was performed to identify and characterize state points along the liquid-vapor coexistence curve of the Jagla liquid. Accurate identification of the liquid-vapor equilibria permits the cavity solvation calculations to be performed in the saturated liquid in analogy to typical apolar solvation experiments in water. Liquid-vapor surface tensions are also calculated. Solvation free energies are obtained using the cavity-solvent structural correlations measured in the MC simulations and the revised scaled particle theory (RSPT) of Ashbaugh and Pratt [2]. The entropic and enthalpic contributions to the solvation free energies are obtained from the temperature dependence of the free energies and reorganization energies as outlined in Chapter 2.

The results of cavity solvation in the Jagla liquid are compared to identical calculations along the saturation curves of the Lennard-Jones (LJ) liquid and water. The same methodology used in the Jagla liquid calculations is also used for the LJ liquid. The cavity equation of state (CEOS) [6] is used to predict cavity solvation thermodynamics in water. The comparisons between the Jagla liquid, water, and the simple liquid (LJ) serve to illuminate

the features of hydrophobic hydration that are unique to water and water-like liquids.

This chapter is organized as follows. Sections 3.2 and 3.3 detail the mathematical models and computational methods used in the calculations. Results are discussed in section 3.4, and conclusions and future directions are given in section 3.5.

3.2 Theoretical and Computational Methods

3.2.1 Revised Scaled Particle Theory

As shown in Chapter 2, all solvation properties may be obtained once the excess chemical potential is known. Thus, our calculations focus on the evaluation of μ_c^x, which for a cavity solute is formally given by

$$\beta\mu_c^x(R) = -\ln p_0(R), \tag{3.1}$$

where $p_0(R)$ is the probability of finding a cavity of size R or larger around a randomly located point in solution. For sufficiently small cavities, $p_0(R)$ may be evaluated directly via the test particle insertion method [97, 99].

In dense liquids, however, the probability of observing density fluctuations large enough to accommodate cavities of size $R \gg \sigma_A$ is vanishingly small, and test particle insertion is known to fail in this case [30]. There are several methods available for the evaluation of chemical potentials for large cavities (see *e.g.*, [56]), but for the Jagla and LJ fluids in this study we choose to use the RSPT [2, 3]. RSPT improves upon classical SPT [75] by including

multi-body correlations. The essential idea behind both RSPT and SPT is that the excess chemical potential must be equal to the work required to inflate a cavity against the solvent from size zero to R. This work must oppose the pressure due to the solvent molecules at the cavity boundary, and thus scaled particle theories require knowledge of the contact correlation function, $G(R)$, defined to be the density of solvent molecules, relative to the bulk, at the cavity-solvent boundary. With $G(R)$ known, the excess chemical potential is calculated as

$$\mu_c^x(R) = \int_0^R k_B T \rho G(r) 4\pi r^2 dr, \tag{3.2}$$

where ρ is the bulk solvent number density. For $R \gg \sigma_A$, the contact correlation function may be expanded in curvature, R^{-1}, with phenomenological coefficients

$$G(R) = \frac{\beta P}{\rho} + \frac{2\beta\gamma_\infty}{\rho R} - \frac{4\beta\gamma_\infty\delta}{\rho R^2} + \dots \tag{3.3}$$

Here, P is the bulk pressure, γ_∞ is the surface tension of a flat solvent-cavity interface, and δ is the first-order curvature correction to the surface tension [1]. An expression for the excess chemical potential of large cavity solutes is then be obtained by expanding Eq. (3.3) to fourth order and integrating to get

$$\begin{aligned}\mu_c^x(R)|_{\text{large}} =& \frac{4\pi R^3 P}{3} + 4\pi R^2\gamma_\infty - 16\pi\gamma_\infty\delta R \\ &+ 4\pi k_B T\rho\kappa - \frac{4\pi k_B T\rho\lambda}{R},\end{aligned} \tag{3.4}$$

where λ is the fourth-order curvature correction coefficient and κ is an integration constant. Third order coefficients are typically set to zero so as to

avoid logarithmic contributions to μ_c^x [84, 89], a convention we follow in this work. The results for the test particle insertion calculations for small cavities, $\mu_c^x(R)|_{\text{sim}}$, are interpolated with the large cavity solute expression in Eq. (3.4) by

$$\mu_c^x(R) = \mu_c^x(R)|_{\text{sim}} f(R) + \mu_c^x(R)|_{\text{large}}(1 - f(R)). \tag{3.5}$$

The function $f(R)$ used here is a cubic function designed to smoothly switch between small (R_{sim}) and large (R_{large}) cavity sizes,

$$f(R) = \begin{cases} 1, & R < R_{\text{sim}}, \\ 1 - 3\frac{(R-R_{\text{sim}})^2}{(R_{\text{large}}-R_{\text{sim}})^2} + 2\frac{(R-R_{\text{sim}})^3}{(R_{\text{large}}-R_{\text{sim}})^3}, & R_{\text{sim}} \leq R \leq R_{\text{large}}, \\ 0, & R > R_{\text{large}}. \end{cases}$$

In order to obtain parameters appearing in the expansion for the contact correlation function, we use Eq. (3.5) and differentiate Eq. (3.2) with respect to R to obtain the contact correlation function as

$$\begin{aligned} G(R) =& \frac{f(R)}{4\pi\rho R^2}\frac{\partial \beta\mu_c^x(R)|_{\text{sim}}}{\partial R} + \frac{\beta\mu_c^x(R)|_{\text{sim}}}{4\pi\rho R^2}\frac{\partial f(R)}{\partial R} \\ &+ \left(\frac{\beta P}{\rho} + \frac{2\beta\gamma_\infty}{\rho R} - \frac{4\beta\gamma_\infty\delta}{\rho R^2} + \frac{\lambda}{R^4}\right)[1 - f(R)] \\ &- \left(\frac{\beta P R}{3\rho} + \frac{\beta\gamma_\infty}{\rho} - \frac{4\beta\gamma_\infty\delta}{\rho R} + \frac{\kappa}{R^2} - \frac{\lambda}{R^3}\right)\frac{\partial f(R)}{\partial R}, \end{aligned} \tag{3.6}$$

and fit this function to the contact values calculated from the MC simulations, as demonstrated in Fig. 3.1. The pressure is set equal to the saturation pressure, and the parameters γ_∞, δ, κ, and λ are fit to the simulation results.

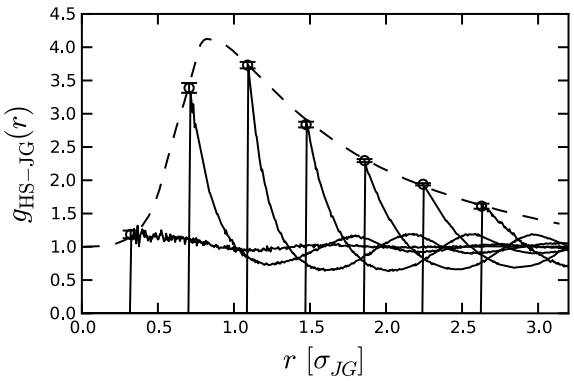

Figure 3.1: Demonstration of a fit of Eq. (3.6) for the cavity contact correlation function to calculated contact values for several cavity sizes in the Jagla liquid at $T = 0.6\ [\varepsilon_2/k_B]$. The contact correlation function, $G(R)$ (dashed line), is fit to the maxima (open circles) in the cavity-solvent pair correlation functions, $g_{HS-JG}(r)$ (solid lines).

3.2.2 The Virial Route to the Surface Tension

Most solvation experiments are carried out at liquid-vapor coexistence. For states near coexistence, the liquid-vapor surface tension has been shown to be closely related to the free energy cost of interface formation near a solvophobic surface [18]. Thus, we are interested not only in obtaining the state points along the coexistence curve but also the liquid-vapor surface tension of the Jagla liquid. This is accomplished simulating, in the canonical ensemble, a system consisting of a slab of liquid Jagla particles bounded on either side by its vapor.

The surface tension, γ_{lv}, is calculated from the profiles of the pressure

tensor using the mechanical definition [55, 92],

$$\gamma_{lv} = \frac{1}{2}\int_0^{L_z} dz[P_N(z) - P_T(z)], \tag{3.7}$$

where $P_N(z)$ and $P_T(z)$ are the local normal and tangential pressures given by

$$P_N(z) = \rho(z)k_BT - \frac{1}{A}\left\langle \sum_{i<j} \frac{z_{ij}^2}{r_{ij}} \frac{du_{JG}(r_{ij})}{dr_{ij}} \frac{1}{|z_{ij}|} H\left(\frac{z - z_i}{z_{ij}}\right) H\left(\frac{z_j - z}{z_{ij}}\right) \right\rangle \tag{3.8}$$

$$P_T(z) = \rho(z)k_BT - \frac{1}{A}\left\langle \sum_{i<j} \frac{x_{ij}^2 + y_{ij}^2}{2r_{ij}} \frac{du_{JG}(r_{ij})}{dr_{ij}} \frac{1}{|z_{ij}|} H\left(\frac{z - z_i}{z_{ij}}\right) H\left(\frac{z_j - z}{z_{ij}}\right) \right\rangle. \tag{3.9}$$

In the above equations, $A = L_xL_y$ is the area of the interface, $u_{JG}(r_{ij})$ is the interparticle potential, and H is the Heaviside step function. The simulation cell is divided into a number of slabs to perform the analysis, and the density profile $\rho(z)$ is estimated from a fit of the average slab densities to

$$\rho(z) = \frac{1}{2}(\rho_l + \rho_v) - \frac{1}{2}(\rho_l - \rho_v)\tanh\left[\frac{2(z - z_0)}{d}\right], \tag{3.10}$$

where ρ_l and ρ_v are the number densities of the liquid and vapor phases, respectively, z_0 is the position of the Gibbs dividing surface, and d is an estimate of the width of the interface. To account for hard-core contributions to the pressure, the pressures are obtained as a function of Δr_0 and extrapolated to contact as in [23, 68].

3.2.3 The Cavity Equation of State

The contact density calculations for the Jagla and LJ liquids demand significant amounts of computer time to obtain good statistics, and performing

similar calculations for typical multi-site water models that have electrostatic interactions is not desirable. We may, however, estimate the excess chemical potential of large cavities in water over a broad range of thermodynamic states by using the recently developed cavity equation of state (CEOS) [6]. The CEOS is an analytical equation of state parameterized to fit experimental and simulation results for water, and it has been shown to accurately reproduce hydrophobic solvation thermodynamics of simple hydrophobes when combined with a first-order perturbation theory. The functional form of the CEOS is given by

$$\beta\mu_c = a + b\beta + c\ln\beta, \tag{3.11}$$

where the coefficients, a, b, and c are assumed to be temperature independent. Thus, the CEOS assumes that the enthalpy of cavity formation depends linearly upon temperature and that the associated heat capacity is temperature independent. The dependence of μ_c on the cavity size, R, is obtained by expanding in powers of $1/R$ and requiring that $\beta\mu_c$ approach $\gamma_{lv}a_0$ in the large cavity limit, where γ_{lv} is the experimental liquid-vapor surface tension and $a_0 = 4\pi R^2$ is the cavity surface area,

$$\beta\mu_c/a_0 = \sum_{i=0}^{3} A_i(1/R)^i + \left[\sum_{i=0}^{3} B_i(1/R)^i\right]\beta + \left[\sum_{i=0}^{3} C_i(1/R)^i\right]\ln\beta. \tag{3.12}$$

The remaining coefficients A_i, B_i, and C_i are obtained from fits to simulation data.

3.3 Model Potentials and Simulation Details

MC simulations of cavity solvation in the Jagla and LJ fluids were performed. The Jagla potential is given by

$$u_{JG}(r) = \begin{cases} \infty, & r < r_0, \\ m_1 r + b_1, & r_0 < r \leq r_1, \\ m_2 r + b_2, & r_1 < r \leq r_2, \\ 0, & r > r_2, \end{cases} \tag{3.13}$$

where

$$m_1 = \frac{-(\varepsilon_2 + \varepsilon_1)}{r_1 - r_0}, \tag{3.14}$$

$$b_1 = -\varepsilon_2 - m_1 r_1, \tag{3.15}$$

$$m_2 = \frac{\varepsilon_2}{r_2 - r_1}, \tag{3.16}$$

$$b_2 = -\varepsilon_2 - m_2 r_1. \tag{3.17}$$

This potential, shown in Fig. 3.2, demonstrates a wide range of behavior for varying parameters, including limiting cases of hard sphere, triangle well, and ramp potentials. Here we choose $r_1 = 1.72r_0$, $r_2 = 3.0r_0$, and $\varepsilon_1 = 3.5\varepsilon_2$, as this particular parameterization manifests a cascade of water-like anomalies [16, 101, 103].

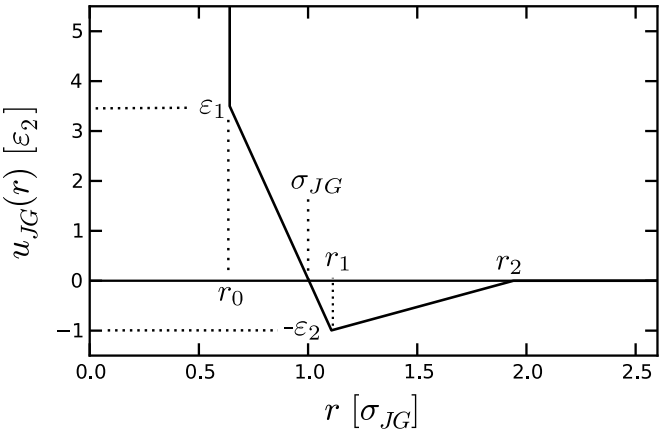

Figure 3.2: The Jagla two-ramp potential. The parameters used here are the same as in [16], *viz.*: $r_1 = 1.72r_0$, $r_2 = 3.0r_0$, and $\varepsilon_1 = 3.5\varepsilon_2$. The relative values of the hard core (r_0) and the soft core (r_1) positions roughly correspond to the same ratio between the positions of the first and second solvation shells of liquid water. The effective size of the Jagla particle, σ_{JG}, is estimated from plots of the radial distribution to be the minimum separation at which $u_{JG}(r) = 0$ (see Chapter 4 and Fig. 4.1).

For the LJ fluid we use the cut-shifted LJ interaction given by

$$u_{LJ}^{cut}(r) = \begin{cases} u_{LJ}(r) - u_{LJ}(r_c), & r < r_c, \\ 0, & r \geq r_c, \end{cases} \tag{3.18}$$

where $u_{LJ}(r) = 4\varepsilon_{LJ}\left(\sigma_{LJ}^{12}/r^{12} - \sigma_{LJ}^{6}/r^{6}\right)$ is the full LJ interaction, ε_{LJ} and σ_{LJ} are the well depth and solvent diameter, respectively, and the cutoff distance, r_c, used is chosen as $2.5\sigma_{LJ}$.

Three different sets of Monte Carlo simulations were performed on the Jagla liquid (Tables A.1, A.2, and A.3). In the first, saturation properties of the Jagla fluid were estimated from canonical ensemble MC simulations of a liquid slab in equilibrium with its vapor for selected temperatures ranging

from near the triple point to just below the critical point. From these slab simulations we estimate saturated liquid and vapor densities, the saturation pressure, and the liquid-vapor surface tension along the binodal line. The surface tension, γ_{lv}, is calculated from the profiles of the pressure tensor using Eq. (3.7). All data for the LJ liquid are obtained from [1].

3.4 Results and Discussion

3.4.1 Surface Tension and Vapor-Liquid Equilibria

In the first set of MC simulations, saturation properties of the Jagla fluid were estimated from canonical ensemble MC simulations of a liquid slab in equilibrium with its vapor for selected temperatures ranging from near the triple point to below the critical point. From these simulations we estimate liquid and vapor densities, the saturation pressure, and the liquid-vapor surface tension along the binodal line.

The results for the liquid-vapor slab simulations of the Jagla fluid are summarized in Table A.1. The saturated liquid densities and the equilibrium vapor densities are in close agreement with those reported by Lomba *et al.* [60]. Fig. 3.4 shows the temperature dependence of the liquid-vapor surface tensions along the binodal curve. The surface tension decreases as a function of temperature and approaches zero near the critical temperature, $T_c = 1.487$ [60]. We expect that our estimates of the coexistence properties of the Jagla fluid may be improved upon by taking finite size effects into account, as it is known, *e.g.*, that large wavelength fluctuations may be suppressed by the

system size [14]. Nevertheless, the solvation behavior we seek to characterize occurs for states at or near coexistence [46], and we therefore expect the present estimates from the slab simulations to suffice for this study.

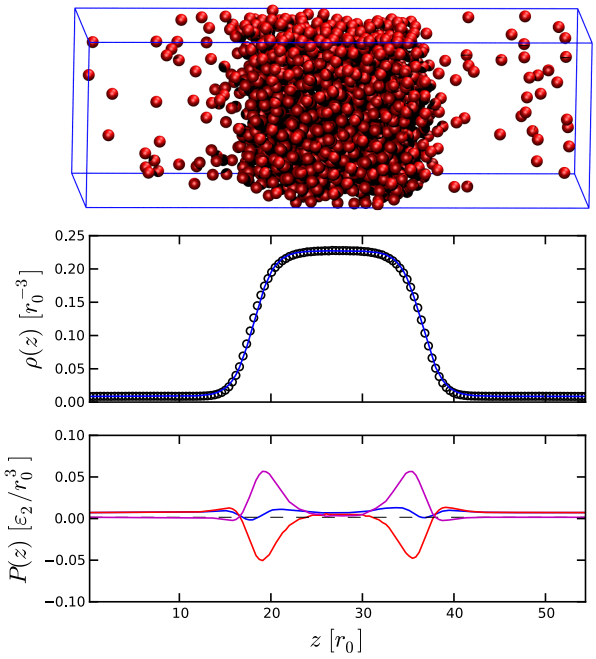

Figure 3.3: (*Top*) A single configuration from the Jagla liquid-vapor slab trajectory at $T = 1.0$ $[\varepsilon_2/k_B]$. (*Middle*) The density profile of the system. Simulation data (open circles) is plotted along with the hyperbolic tangent fitting equation (blue line). Statistical errors are smaller than symbol size. (*Bottom*) Normal (blue) and tangential (red) pressure profiles and their difference (magenta) along the simulation cell length.

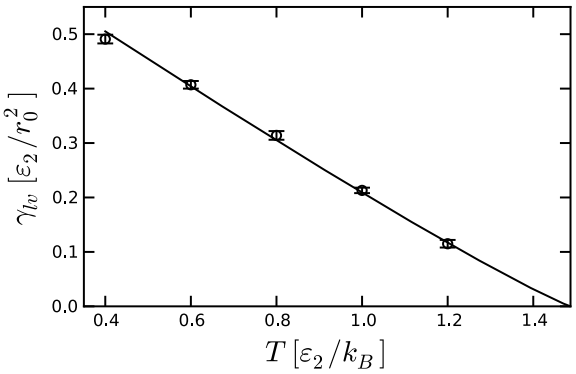

Figure 3.4: Jagla liquid-vapor surface tension versus temperature calculated via slab simulations (open circles). The solid line is the fit of the slab simulation data to $\gamma_{lv} = \gamma_{lv_0}|1 - T/T_c|^{2\nu}$, an expected functional form for the surface tension in three dimensions [98]. The parameters obtained from the fit are $\gamma_{lv_0} = 0.713$ and $2\nu = 1.10$.

3.4.2 Cavity Solvation Thermodynamics

3.4.2.1 Contact Densities

The results of the MC calculations for the cavity contact correlation functions are shown in Fig. 3.5. In both fluids, as the solute size grows from zero, the solvent packs increasingly tightly until the contact density peaks at a value of R on the order of the solvent size. At this point the solvent begins to pull away from the solute, and for sufficiently large solutes, $G(R)$ will be less than one. The contact correlation function is a decreasing function of temperature for all solute sizes studied here, but for sufficiently large solute sizes $G(R)$ will increase with temperature since $\lim_{R\to\infty} G(R) = \beta P/\rho$, which increases with temperature along the saturation curve.

The results for the fit of Eq. (3.6) to the Jagla liquid $G(R)$ simulation

data are presented in Table A.4. The surface tension of the flat interface, γ_∞, is slightly higher than the liquid-vapor surface tension measured in the slab simulations at all temperatures. This discrepancy has also been observed for the LJ liquid [1], and is possibly due to quenched fluctuations at the solvent-wall interface. The first order curvature correction, δ, is negative and decreases with increasing temperature, also consistent with the results for the LJ liquid.

Unlike the LJ liquid, the Jagla liquid $G(R)$ peaks at values of R that are greater than the solvent size. This is again consistent with a greater propensity for void formation in the Jagla liquid—solvent-sized cavities are more readily accommodated in the Jagla liquid than the LJ liquid. Similarly, the cavity sizes where $G(R)$ decreases below one are larger relative to the solvent size in the Jagla liquid, meaning that the Jagla liquid resists dewetting of hard surfaces more than the LJ liquid. Lastly, the spacing between temperatures for a fixed cavity size in the LJ liquid $G(R)$ appears constant, suggesting a linear dependence upon temperature. This is not the case in the Jagla liquid, however, as the temperature spacing clearly decreases with increasing temperature.

3.4.2.2 Chemical Potentials

With the fitted parameters to $G(R)$ the excess chemical potentials for the Jagla and LJ liquids may be obtained from Eq. (3.5). In the case of water we use Eq. (3.12). The results of the chemical potential calculations are shown in Figs. 3.5 and 3.6. The excess chemical potential is a positive, monotonically

increasing function of cavity size at all temperatures in all three liquids.

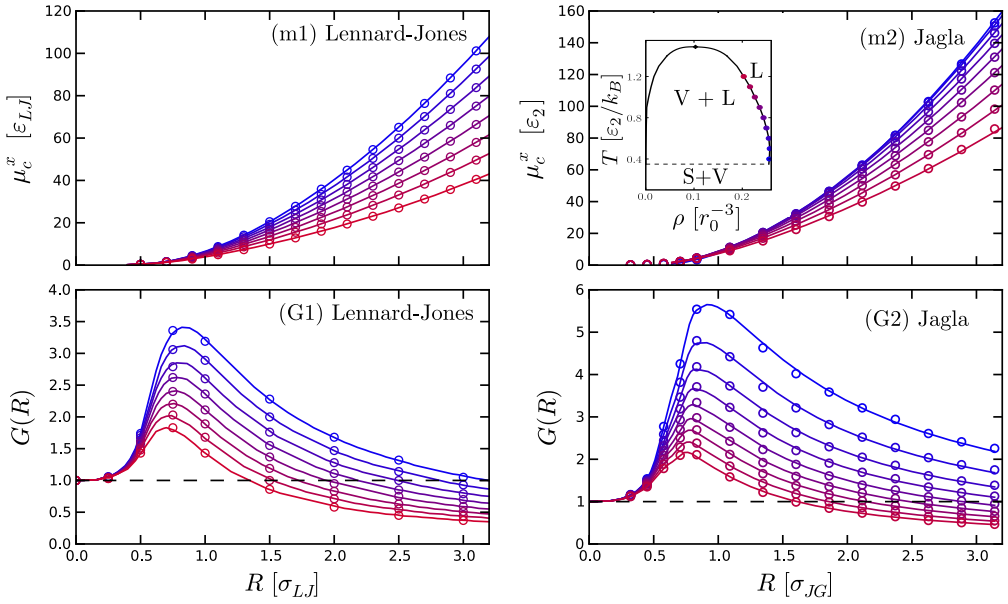

Figure 3.5: (m1) and (m2) Excess chemical potential versus cavity size for states along the saturation curves of the LJ and Jagla liquids ranging from near the triple point (blue) to just below the critical point (red). The thermodynamic states for the Jagla liquid are the same as those in Table A.2. The inset in (m2) shows the locations of each of the Jagla states along the liquid-vapor coexistence curve. Points are calculated from Eq. (3.5), while lines are fits to the data. The Jagla liquid data are fit using the cavity equation of state, while the data for the LJ liquid are fit to Eq. (3.19). (G1) and (G2) Cavity contact correlation functions used to calculate the chemical potentials in (m1) and (m2). Points are simulation data and lines are fits of Eq. (3.6) to the simulation data. Statistical errors are smaller than symbol size. All LJ data are obtained from [1].

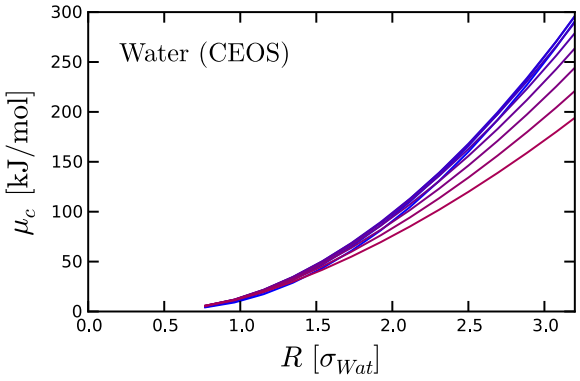

Figure 3.6: Cavity chemical potential versus cavity size for states along the saturation curve of water as predicted by the cavity equation of state. The temperatures of the states are (from blue to red) 273, 304, 335, 366, 398, 429 460, 491 and 522 K.

In the LJ liquid, the chemical potential is a decreasing function of temperature for all cavity sizes greater than $\sigma_{LJ}/2$. Furthermore, the spacing between temperatures for any fixed cavity size appears roughly constant in the LJ liquid, which, as pointed out by Ashbaugh [1], suggests that along the saturation curve the excess chemical potential may be modeled as

$$\mu_c^x(R) = h_c^x(R)|_\sigma - T s_c^x(R)|_\sigma, \tag{3.19}$$

where $h_c^x(R)|_\sigma$ and $s_c^x(R)|_\sigma$ are the temperature independent orthobaric enthalpy and entropy of solvation. The enthalpy is positive and increases with cavity size, indicating the loss of favorable solvent-solvent interactions near the cavity solute. Except for cavities smaller than $\sigma_{LJ}/2$, the entropy is also a positive, increasing function of cavity size, indicating that solvent molecules near the cavity experience a net gain in configurational space. The excellent fit

of Eq. (3.19) to the simulation data [Fig. 3.5(m1)], indicates that that the enthalpy of solvation is approximately temperature-independent, and therefore the heat capacity of cavity solvation in the LJ liquid is approximately zero.

In the Jagla liquid, in contrast, the chemical potential is an increasing function of temperature for small, solvent-sized cavities and a decreasing function of temperature for large cavities. The temperature derivative of the excess chemical potential for a fixed cavity size is not constant [Fig. 3.5(m2)], but is evidently nonlinear. The qualitative behavior of the chemical potential of cavity solvation in the Jagla liquid is remarkably similar to that predicted for liquid water by the CEOS, shown in Fig. 3.6. This suggests that the Jagla liquid data might be fit to the CEOS as well. Using the surface tension data from Table A.4 and a least-squares fit of the excess chemical potentials calculated from the $G(R)$ data, we obtained a set of CEOS parameters for the Jagla liquid (Table A.5). The fit is excellent for all cavity sizes and temperatures considered, with slight deviations occurring only for the largest cavities at the highest temperature. The CEOS fit to the simulation data permits exploration of the thermodynamic contributions to μ_c^x in the Jagla liquid using analytical derivatives of Eq. (3.12).

3.4.2.3 The Solubility of Small Solvophobes

For cavities close to the size of the Jagla particle, the chemical potential is a concave function of temperature with a maximum that shifts to lower temperatures as the cavity size is increased, as in water [33]. This non-monotonic

behavior is distinct from the LJ liquid and mimics cavity solvation in liquid water, as shown in Fig. 3.7. The figure shows the excess chemical potential and solubility of small solutes as a function of temperature in all three liquids. Over a given temperature range, non-monotonic behavior of μ_c^x does not necessarily imply non-monotonic behavior in the solubility. Cavity solubilities monotonically increase over the temperature range considered for all three liquids. Decreasing cavity size and increasing solute-solvent attractions are both known to shift the solubility minimum towards higher temperatures in water [33], and such attractions would cause non-monotonic behavior of the solubility in the temperature range considered here as well for water. We expect the same behavior for the Jagla liquid.

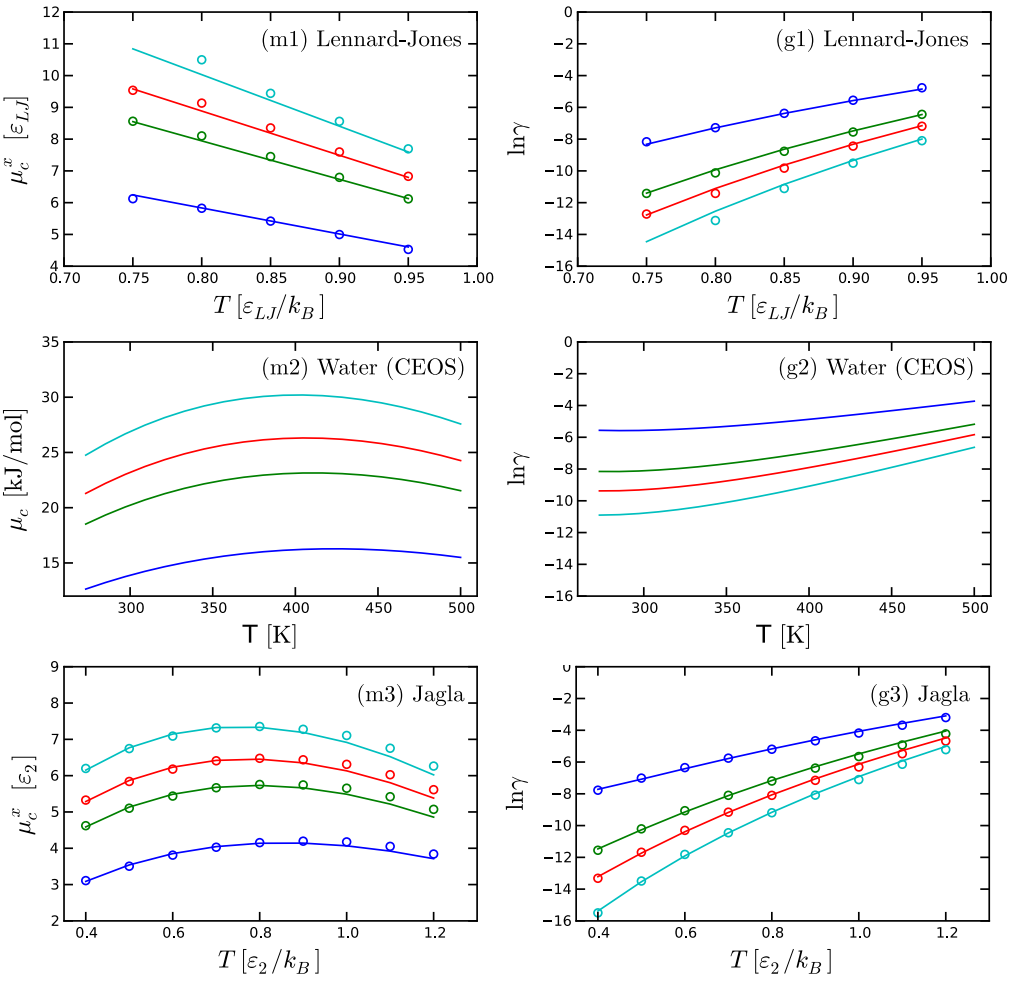

Figure 3.7: Temperature dependence of solubility for small cavities in water, the Jagla liquid, and the LJ liquid along the saturation curves of each fluid. The relative size of the cavities to the solvent molecule is the same in all three fluids and roughly corresponds to the relative sizes of neon (blue), argon (green), krypton (red), and xenon (cyan) to the size of a water molecule. Points are simulation data from test particle insertions, while lines are fits to the simulation data. The fits in the case of water and the Jagla liquid use Eq (3.12), while the LJ data are fit to Eq. (3.19). The excess chemical potential (m1-m3) is non-monotonic over the temperature range for the Jagla liquid and water but monotonic for the LJ liquid. The solubility (g1-g3) increases monotonically with temperature for all states considered in all three fluids.

3.4.2.4 Enthalpic and Entropic Behaviors

The orthobaric enthalpic and entropic contributions to the excess chemical potential for the Jagla liquid and water may be obtained from analytical temperature derivatives of the CEOS. The orthobaric enthalpy and entropy of cavity solvation are compared in Fig. 3.8. The most obvious distinction between the three liquids is that the LJ liquid has temperature independent enthalpic and entropic contributions to the solvation free energy, while the contributions for the Jagla liquid and water both show a strong temperature dependence.

For all three fluids, the enthalpy is a positive, monotonically increasing function of the cavity radius. The unfavorable enthalpy results from the disruption of the liquid structure in the vicinity of the solute and the concomitant formation of an interface which on average has fewer favorable solvent-solvent interactions than an equivalent volume in the bulk.

For any fixed cavity size in the size ranges considered in this study, the enthalpy is an increasing function of temperature in the Jagla liquid and in water. A possible interpretation for this result in water is given by the Muller model [38, 67], which uses a simple two-state hydrogen bond (H-bond) model parameterized by empirical solvation data to argue that the fraction of broken H-bonds in the solvation shell of apolar solutes is always greater than that in the bulk, and furthermore, that this disparity increases with temperature. Thus, for a fixed cavity size an increase in temperature decreases the number of H-bonds in the solvation shell relative to the bulk, which leads to a greater

enthalpy.

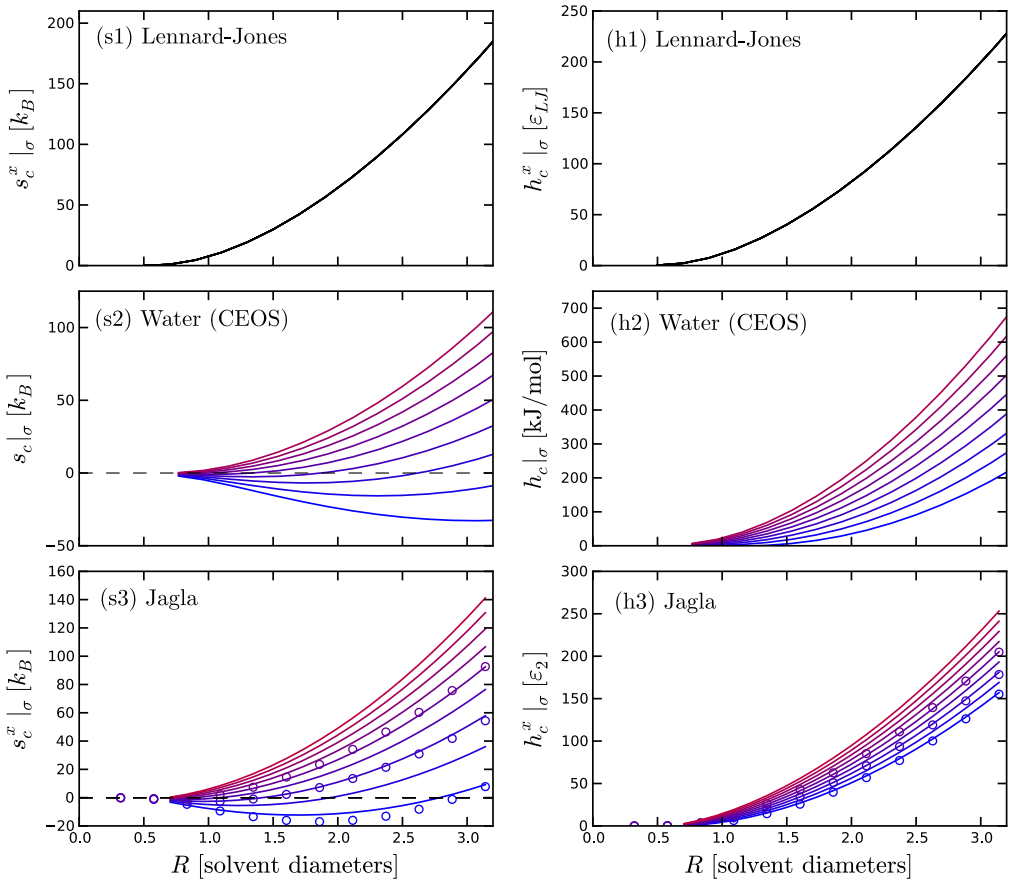

Figure 3.8: Orthobaric (s1-s3) entropy and (h1-h3) enthalpy of cavity solvation for the LJ liquid, water, and the Jagla liquid as a function of cavity size for the same states as in Fig. 3.5. For water and the Jagla liquid, entropies are calculated from temperature derivatives of the cavity equation of state (lines), $s_c^x|_\sigma = -(\partial\mu_c^x/\partial T)_\sigma$, while for the LJ liquid, the entropy is given by the assumed temperature-independent form of μ_c^x in Eq. (3.19). The enthalpy is calculated from $h_c^x|_\sigma = \mu_c^x + Ts_c^x|_\sigma$. Points in (s3) and (h3) are numerical derivatives of cubic spline fits to the excess chemical potentials in Fig. 3.5.

A distinguishing feature of hydrophobic hydration is that the transfer

of small apolar solutes to water proceeds with a *decrease* in entropy. This negative entropy of transfer increases with temperature until about 400 K, at which point the entropies of small apolar solutes converge to zero [34]. This phenomenon supports the widely held view that hydrophobic forces govern protein stability, as it is also known that the hydrophobic contributions to the entropies of unfolding of globular proteins are negative and converge to zero near 385 K [15, 72]. Interestingly, the Jagla liquid captures this water-like entropy behavior—the entropy of solvation for small cavities given by the CEOS is *negative* in both the Jagla liquid and water at low temperatures (Fig. 3.8, s2 and s3), and these entropies converge to zero as temperature is increased (Fig. 3.9). The loci at which the entropy curves in Fig. 3.8 (s3) cross zero are the entropy convergence temperatures for cavities of a given size. For example, the entropy convergence temperature for cavities on the order of the size of the Jagla particle is around 0.9 $[\varepsilon_2/k_B]$, as seen in Fig. 3.9.

Unlike the enthalpy, the entropy of cavity formation in both the Jagla liquid and water becomes less unfavorable upon increasing the temperature at a fixed cavity size. It is possible that this behavior in water may be connected to the breaking of H-bonds. An increase in temperature causes an overall decrease in the number of H-bonded pairs, which gives more configurational freedom to the water molecules, thus creating the favorable entropy increase. However, this cannot explain the Jagla model behavior.

It is remarkable that the Jagla liquid, which contains no orientational dependence in its interaction potential and therefore no H-bonding, reproduces

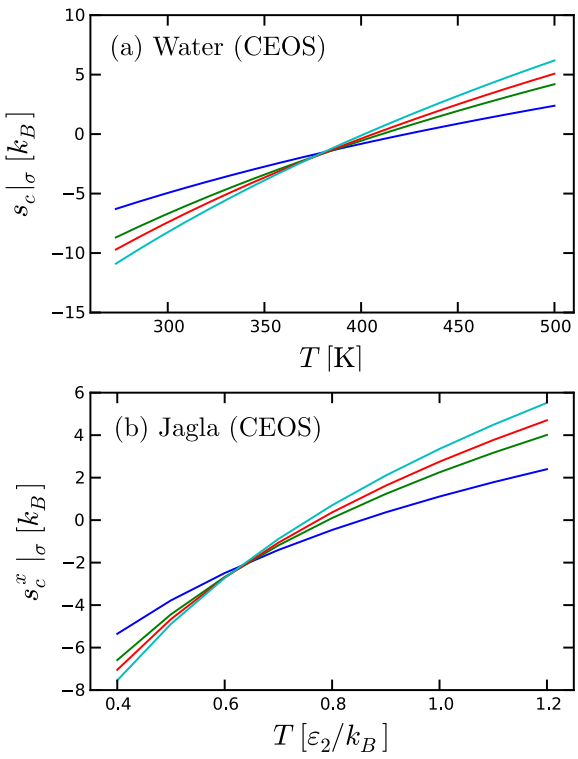

Figure 3.9: Entropy convergence for the small solutes in Fig. 3.7 observed along the saturation curves (σ) of water and the Jagla fluid. Entropies are computed as temperature derivatives of the cavity equation of state for each fluid. Differences between the orthobaric entropies and constant pressure entropies for the two fluids are negligible for small cavity sizes.

the qualitative behavior of hydrophobic hydration thermodynamics. The underlying physical origins for this behavior in the Jagla liquid may be analogous to those of water, however. It has been shown in computer simulations of SPC/E water that the energetics of H-bonding are dependent upon local crowding effects. In particular, H-bonded pairs with a small number of neighbors will on average have a stronger H-bond than bonded pairs with a greater

number of neighbors [64]. Furthermore, the fraction of H-bonded pairs in interfacial regions of apolar moieties is lower than in the bulk liquid, and the bonded pairs that do exist in these regions tend to have fewer neighbors and stronger bonds than the average H-bonded pair in the bulk. The interpretation is that density fluctuations that create small cavities select against weak H-bonds, leaving only the stronger bonds to survive. Thus, the interfacial region experiences less H-bonding on the whole than equivalent volumes in the bulk, but maintains on average stronger hydrogen bonds. This does not necessarily imply the existence of "ice-like" structure, but rather suggests that the hydration shells of small apolar solutes consist of small numbers of strongly H-bonded water molecules with bonding vectors oriented tangentially to the solute surface. The presence of the solute in a previously accessible region of space and the rigidity of the strong H-bonds are sufficient to cause the decrease in entropy.

A plausible analogy in the Jagla liquid to H-bonding in water is the interaction of particle pairs at the potential minimum distance, r_1. As temperature is lowered, the liquid prefers to adopt configurations that maximize the number of particle pairs near a separation of r_1, which in the limit of the crystal is an fcc lattice [53]. Under these conditions, density fluctuations that create small cavities more often disrupt weakly interacting Jagla particles and therefore leave a solvation shell that consists of fewer pair interactions near r_1. The interactions that do remain are on average more favorable than those in equivalent bulk volumes. If this is indeed the case, we would expect to see

a more sharply peaked maximum and a lower coordination number near r_1 in the solvation shell pair distribution function than in the same for the bulk liquid. This conjecture is investigated further in Chapter 4.

The LJ liquid demonstrates enthalpic and entropic behaviors in sharp contrast to those of water and the Jagla liquid. The entropy is strictly positive for all cavities of size $R > 0.5\sigma_{LJ}$ in the LJ liquid, and the heat capacity increment is negligible. This latter phenomenon is consistent with the argument for the temperature dependence of the relative fraction of broken H-bonds in solvation shell water compared to bulk water—*i.e.*, the absence of a second energy scale in the LJ liquid precludes a temperature-dependent enthalpy of cavity formation analogous to that of water. Similarly, the presence of a solute cannot stabilize fluctuating structures of strongly interacting solvent pairs at a second, lower energy scale. This prevents a negative entropy of cavity formation in the LJ liquid. This argument implies that it is two energy scales, rather than two liquid length scales, that is the underlying feature in common to water and Jagla fluids.

3.4.2.5 Constant Pressure Reorganization Energy

A solvation quantity of interest in the context of protein stability is the partial molar volume. It was recognized by Kauzmann that the partial molar volume implied by the pressure-induced denaturation of proteins is generally negative. He attributed this to the hydrophobic effect [54]. Kumar *et al* argued that the partial molar volume contributes little to the aqueous solubility of gas-phase solutes, but that it plays an important role in the solubility of chain-like organic solutes [57].

In addition to the partial molar volume, recent simulation studies of the solubility of small apolar solutes in a family of modified water models have shown that the solvent reorganization energy in water is anomalously low compared to more typical solvents and is responsible for the relatively weak temperature dependence of the solubility of apolar solutes in water [62].

Here we consider the solute size dependence of the partial molar volumes and reorganization energies of apolar solvation. In Fig. 3.10 we show the constant pressure solvent reorganization energy and partial molar volume for cavities ranging from one-half to six solvent diameters in the Jagla liquid. Both quantities are strictly positive and increase monotonically with cavity size. Increasing the solvent temperature increases both the reorganization energy and the partial molar volume. Comparing the relative magnitudes of the partial molar volume and reorganization energies, we expect that for large cavities the second term in Eq. (2.24), which will be large and positive, will dominate the temperature-dependence of the solubility.

In Fig. 3.11 the partial molar volumes and solvent reorganization energies for cavities in the LJ and Jagla liquids are compared as a function of cavity size. The thermodynamic states are "corresponding" in that the reduced temperature, T/T_{crit}, where T_{crit} is the temperature at the liquid-vapor critical point, is the same (0.7) in both liquids. The reorganization energies (scaled by k_BT) for the Jagla liquid are systematically lower than those in the LJ liquid, but not dramatically so, compared to behavior seen in the modified water models study. The behavior is opposite in the case of partial molar volumes, with the molar volumes of cavities being consistently lower in the LJ liquid than in the Jagla liquid with the disparity growing as a function of cavity size.

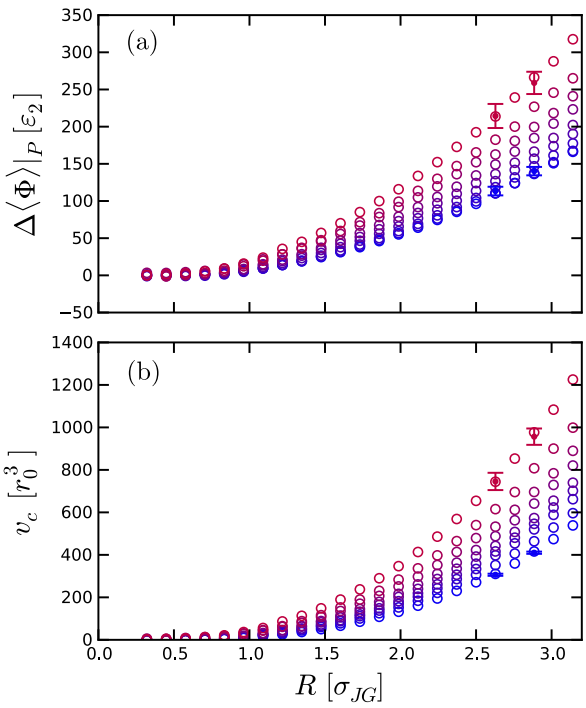

Figure 3.10: (a) Constant pressure solvent reorganization energy due to the presence of a cavity in the Jagla liquid as a function of cavity size and temperature. The coloring and state points are the same as those in Fig. 3.5. The reorganization energy is computed from Eq. (2.29). (b) Partial molar volume as a function of cavity size and temperature in the Jagla liquid for the same state as in (a). The partial molar volume is computed from Eq. (2.30). For both calculations a system of 4000 Jagla particles was tested at the highest and lowest temperatures for cavity sizes of $R = 4.1$ and $R = 4.5$ (solid points with error bars) to test the dependence of the results on system size. There are no statistically significant differences.

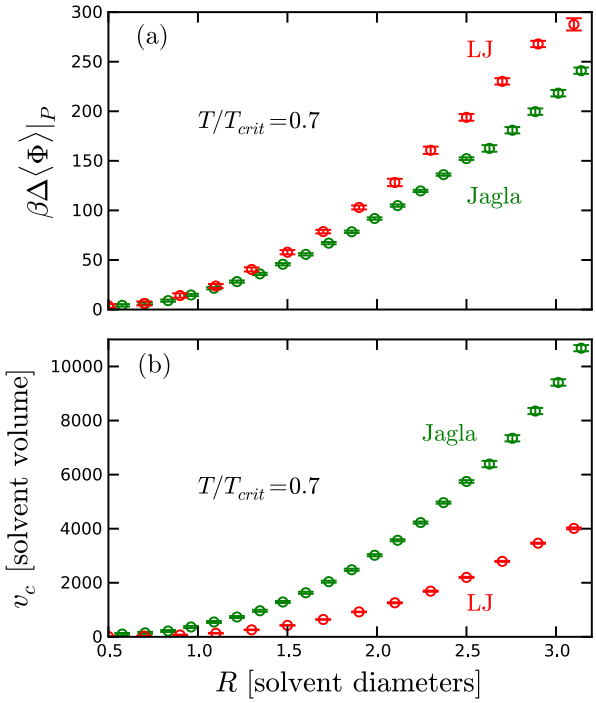

Figure 3.11: A comparison of (a) constant pressure solvent reorganization energy and (b) partial molar volume as a function of cavity size in the Jagla and LJ liquids. Calculations are performed for a reduced temperature of $T/T_{crit} = 0.7$ on the saturation curve of each liquid.

3.5 Conclusions

The results of exhaustive MC simulations of cavity formation along the saturation curves of the LJ liquid and the Jagla liquid were presented. The temperature-dependence of the solvation thermodynamics of cavities ranging from one-half to six times the solvent particle size were compared between the two simple liquids and to predictions for cavity formation in water given by the CEOS. The comparisons between the Jagla liquid, water, and the simple liquid (LJ) serve to illuminate the features of hydrophobic hydration that are unique to water.

The Jagla liquid demonstrates water-like behavior in its resistance to dewetting of large cavity surfaces. In the presence of the largest cavity sizes considered (six solvent diameters), the LJ liquid showed a dewetting transition at all thermodynamic states on the saturation curve, whereas the Jagla liquid resists dewetting at low temperature saturation states.

The Jagla liquid is also water-like in its enthalpic and entropic behavior in the sense that the solvation entropy of small cavities is negative and the heat capacity increment is positive. Moreover, the Jagla liquid reproduces the phenomenon of entropy convergence observed in water. The LJ liquid on the other hand manifests a strictly positive entropy for all cavities larger than half the solvent size and shows a negligible heat capacity increment.

It is speculated that the solvation shell of small cavities in the Jagla liquid will be less crowded and consist of fewer particles separated by a dis-

tance close to the potential minimum, r_1, than equivalent volumes in the bulk liquid. This is analogous to results from molecular simulations of water, which show that on average the solvation shell of apolar moieties contains a lower coordination number and fewer H-bonds than equivalent bulk volumes, but that the H-bonds that remain are on average stronger [64, 106].

We infer that it is the existence of two energy scales in the Jagla liquid and water (potential minimum / ramp height energies, and H-bonded / not H-bonded, respectively) and the fact that at low temperatures the energetically favorable interaction necessitates an increase in void space, that gives rise to the anomalous solvation behavior. Of course, the ability of the fluid to access the low energy structures without excessive expansion implies that the length scales are closely coupled to this observation [103].

Chapter 4

Distribution Functions, Void Statistics, and Density Fluctuations on a Molecular-Scale

4.1 Introduction

The striking similarities in the macroscopic solvation thermodynamics of cavity solutes in the Jagla liquid and water were revealed in Chapter 3. In this chapter we seek to understand the molecular-level origins of those similarities. In particular, we are interested in the liquid structure, the distribution of void space, and the fluctuations of solvent particles in and out of molecular-scale volumes in the liquid. Several studies of this kind exist in the literature for water. For example, the seminal computer study of liquid water by Guillot and Guissani [42] considers pair distribution functions along the liquid-vapor coexistence curve. They were able to demonstrate water's strong preference for tetrahedral order at low temperatures and show that this structure breaks down between 423-473 K. in't Veld *et al.* considered cavity size distributions in water and hard sphere systems. The authors concluded that water has a strong propensity to cluster, creating larger tails in its void space distribution than seen in distributions for more typical liquids. Hummer *et al.* have developed an information theory [48–50] for hydrophobic effects that accurately describes density fluctuations in molecular-sized cavities when

Gaussian statistics are assumed.

Comparatively few studies for other liquids exist, however, and the uniqueness of water is often lost in the over-abundance of studies focusing only on water. Furthermore, there are doubts about the validity of the comparisons between cavity size distributions in water and the hard sphere systems of in't Veld's study [39], and there is increasing evidence that the Gaussian behavior seen in water is not a general feature of molecular-scale density fluctuations in liquids [32, 43, 44].

In the present chapter, we perform a comparative analysis of the aforementioned molecular-scale statistical quantities for water and the two simple liquids of Chapter 3, *viz.,* the Lennard-Jones (LJ) liquid and the Jagla model of Eq. (3.13). The model used for water is the SPC/E model [11], which is known to accurately model the phase behavior and solvation thermodynamics of water over a broad range of states [41, 42]. In Section 4.2 we describe the simulation methods used to analyze the liquids. Results are discussed in Section 4.3 beginning with a discussion of liquid structure and continuing with a discussion of cavity size distributions and density fluctuations. Conclusions and future directions are given in Section 4.4.

4.2 Methods

Constant pressure NPT MC Simulations of the pure Jagla liquid [Eq. (3.13)] at saturation were performed for each of the states listed in Table A.2. A system consisting of $N = 1000$ Jagla particles in a cubic cell with periodic

boundary conditions was equilibrated for 2×10^5 MC cycles, where one MC cycle corresponds to N MC moves. In each MC move, there is a $1/N$ chance of attempting a volume move and $(N-1)/N$ chance of attempting to move a randomly selected particle. Particle and volume trial displacements were adjusted to achieve acceptance ratios of 0.5 during the equilibration run. The system was simulated for 6×10^5 MC cycles after equilibration and statistics were gathered. Frames were output every 5 MC cycles for analysis. Identical simulations were performed for the cut-shifted LJ liquid for the states listed in Table A.6.

The SPC/E model was used to model water [11]. A system consisting of 512 SPC/E water molecules was simulated in a cubic box with periodic boundary conditions in the canonical ensemble for 20 ns using the GROMACS molecular dynamics engine [12, 90] at each of the states listed in Table A.7. The time step was chosen as 2 fs, and bonds were constrained with the SETTLE algorithm [65]. The velocity rescaling thermostat was used to control temperature with a time constant of 0.1 ps [17]. Particle mesh Ewald summation was used to treat long range electrostatic interactions [26] with a real space cutoff of 1.2 nm and a mesh spacing of 0.18 nm. The Ewald tolerance was set to 10^{-5}, and fourth order interpolation was used.

Test particle insertions were performed on each of the liquid trajectories. For each frame in each trajectory, spherical volumes ranging from $R = 0.5$ to $R = 1.7$ solvent diameters were analyzed. Each volume was placed 4×10^4 times at random points in the fluid. For each placement the number of solvent

centers contained in the volume was recorded, and the distributions of $p_n(R)$, the probability of finding exactly n solvent centers in a spherical volume of radius R, were accumulated. In the case of SPC/E water, only the locations of the oxygen atoms were recorded. Statistical errors were estimated using the method of Flyvbjerg and Peterson [28].

Additionally, $P(R)$, the probability that the nearest solvent particle to a randomly located point in solution is a distance R away, was measured. For each frame in each trajectory, the nearest solvent particle to 5×10^4 random points was binned.

Pair distribution functions were also measured. In the case of the Jagla liquid, the pair distribution function for a solvent particle located in the solvation shell was compared to that for the bulk solvent. The solvation shell was defined as solvent molecules within 1.45 solvent diameters of the cavity surface. Here, the solvent diameter is defined as the minimum separation at which the bulk solvent-solvent pair distribution function reaches a value of unity. We regard this definition as a reasonable choice since the density is depleted at shorter distances, and we use this definition consistently between all liquids considered in this study. The definition of the solvation shell is consistent with similar definitions for the solvation shell of liquid water [64], and includes only the first peak in the cavity-solvent pair distribution function (see Fig. 3.1).

In all of the analyses presented in this Chapter except for the last section on density fluctuations, only three saturated liquid states were selected for comparison between the liquids. This is done for clarity in the presentation

of graphical results. For each liquid, we consider a low-temperature state close to the triple point, a state midway between the triple and critical points, and a state approaching the critical region. These states are not corresponding in the van der Waals sense, *i.e.*, the reduced temperatures, $T^* = T/T_{crit}$, where T_{crit} is the liquid-vapor critical temperature, are not the same between the liquids. This type of classical corresponding states comparison is hindered by the fact that the stable liquid region of the phase diagram differs considerably in size between the three liquids. The triple point occurs in the LJ liquid at a reduced temperature of approximately $T^* \approx 0.6$ [82], in the Jagla liquid at $T^* \approx 0.24$ [60], and in SPC/E water at $T^* \approx 0.33$ [91]. Nevertheless, we believe the choice of states compared here suffices for highlighting the similarities and differences in the temperature dependence of the statistical quantities of interest in this chapter.

4.3 Results and Discussion

4.3.1 Pair Distribution Functions

A comparison of the pair correlation function, $g(r)$, for the three liquids is shown in Fig. 4.1. The maximum in $g(r)$ for the LJ liquid occurs at a pair separation slightly larger than σ_{LJ}, and at a separation of exactly σ_{LJ} the pair distribution function assumes a value of approximately one for all states on the saturation curve. The nearest separation at which $g(r)$ is unity is a common estimate for the size of a particle since the surrounding fluid is depleted from all shorter distances. We adopt this approach here and use σ_{LJ} as an estimate

for the size of the LJ particle.

In the case of SPC/E water, the pair distribution function peaks at about 0.28 nm at ambient temperature and slightly larger distances at higher temperatures. These distances are smaller than the LJ diameter for oxygen due to H-bonding. The nearest separation at which $g(r)$ is unity is about 0.26 nm, which, to be consistent, is our choice for the size of the SPC/E molecule, σ_{Wat}.

The maximum peak in the Jagla liquid $g(r)$ occurs at a distance significantly larger than the hard core diameter, r_0. This reflects the preference of Jagla particles to maintain separation at the minimum in $u_{JG}(r)$, r_1, which creates a greater void space in the Jagla liquid. This preference is diminished as temperature increases. However, the minimum separation at which the Jagla $g(r)$ is unity is found to be insensitive to temperature [see Fig. 4.1 (c)] and closely corresponds to the minimum separation at which the pair potential is zero. This distance, σ_{JG}, is the estimate for the size of the Jagla particle; $\sigma_{JG} = 1.56r_0$ for the parameterization considered here.

It should be emphasized that the choice of solvent size is crucial for proper comparisons between liquids. For example, cavities required to accommodate typical small apolar solutes such as neon, argon, methane, and xenon range in size from 1 to 1.25 water diameters by the definition used here. Previous studies on the Jagla liquid have investigated hard sphere solutes with diameter equivalent to r_0 in Eq. (3.13), which requires a substantially smaller cavity size of only $0.82\sigma_{JG}$ [16].

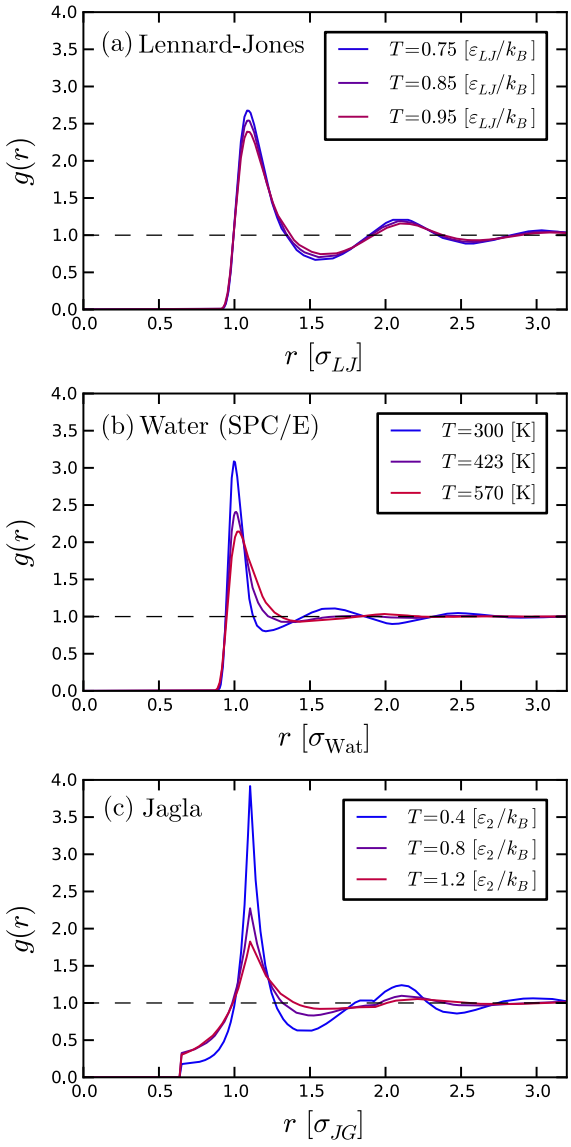

Figure 4.1: Solvent-solvent pair distribution functions for states along the saturation curves of (a) the LJ liquid, (b) SPC/E water, and (c) the Jagla liquid. The minimum separation at which $g(r)$ is unity is used as an estimate for the solvent size. For the SPC/E model this corresponds to $\sigma_{Wat} = 0.26$ nm, for the LJ liquid it is σ_{LJ}, and for the Jagla liquid it is $\sigma_{JG} = 1.56r_0$ (the minimum separation at which $u_{JG}(r) = 0$). These sizes are assumed to be independent of temperature for the states considered here, in accord with the data shown.

In an effort to further investigate the origins of the enthalpic and entropic behaviors described in Section 3.4.2.4, we have also computed the pair distribution functions for solvation shell Jagla particles. The solvation shell is defined as solvent molecules within 1.45 Jagla diameters of the cavity surface, where the cavity surface is simply the exclusion diameter. The pair correlation function within the shell is normalized by the product of the shell volume, *excluding* any intersection with the cavity, and the bulk density. Fig. 4.2 (s1-s3) show the pair distributions for solvation shell Jagla particles as a function of cavity size and saturation state. The pair distribution functions for Jagla particles in the solvation shell of small cavities are indistinguishable from the bulk pair distributions functions at all temperatures considered. This result is consistent with the fact that small, solvent-size cavities are naturally formed by the liquid and that the liquid structure is undisturbed by the presence of a cavity. Larger cavities, however, show a slightly depleted solvation layer at the lowest temperatures that grows in size as temperature is raised. This is a manifestation of the incipient dewetting transition for large cavities at high temperatures, which, as shown in Chapter 3, occurs for $R \geq\sim 1.75\sigma_{JG}$ [see Fig. 3.5 (G2)].

The results neither confirm nor deny the conjectures for the origins of the enthalpic and entropic behaviors suggested in Section 3.4.2.4. A full investigation of orientational order within the solvation shell compared to bulk could prove illuminating in further studies. However, it is clear that in the solvation shell the relative loss of density for $r < \sigma_{JG}$, where $u_{JG}(r) > 0$,

is greater than that for $r \sim 1.1\sigma_{JG}$, near the potential minimum, which is consistent with the earlier hypothesis.

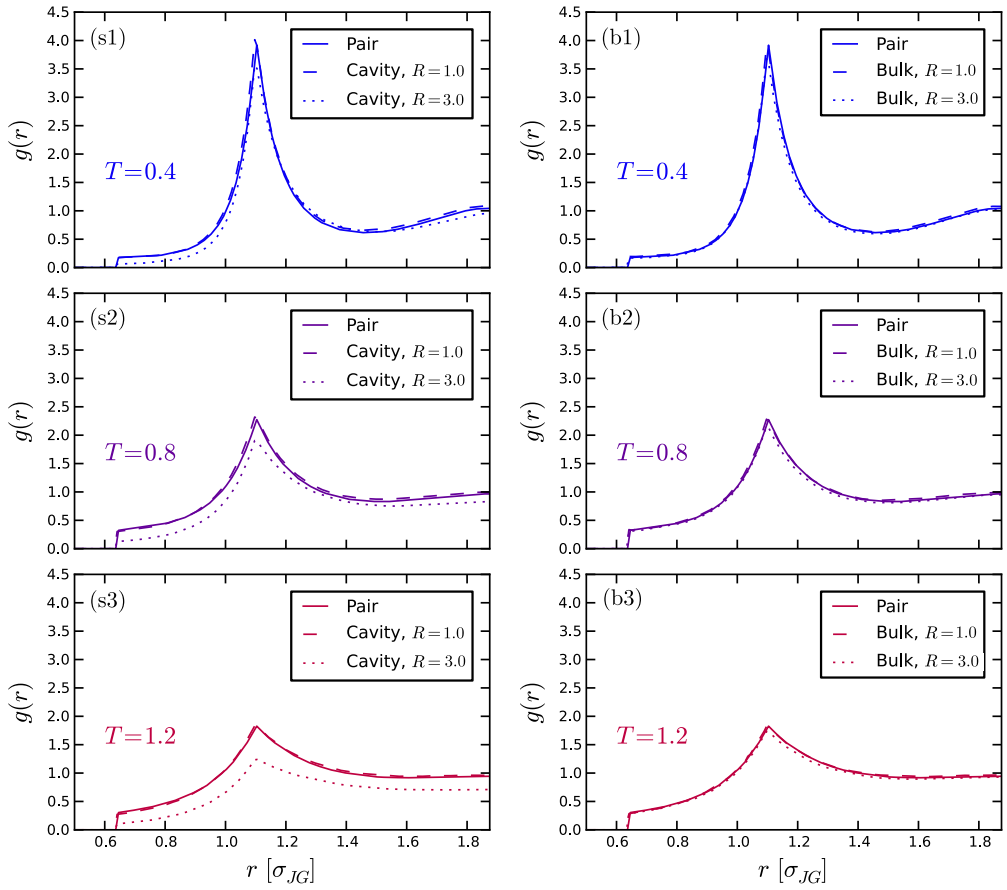

Figure 4.2: (s1-s3) Pair distribution functions for solvation shell Jagla particles for small and large cavity sizes for various saturation temperatures. The solvation shell includes all solvent particles within 1.45 Jagla diameters of the cavity surface. The solid lines, labeled "Pair", are the bulk pair distribution functions shown for comparison. The dashed line is the pair distribution function for Jagla particles in the solvation shell of a small, solvent-sized cavity, and the dotted lines are the same for a larger cavity. (b1-b3) Pair distribution functions for Jagla particles in spherical shells equivalent in size to those in (s1-s3) but in the bulk Jagla liquid. This is shown to verify that the normalization of the pair distribution function is correct.

4.3.2 Cavity Size Distributions

We compare the void space distributions by calculating $P(R)$, the probability that the nearest solvent molecule to a randomly located point in solution is at a distance R. This is equivalent to the probability that the largest cavity that may be inserted at the location is of size R. These cavity size distributions, shown in Fig. 4.3, reveal relatively subtle differences in the nature of void space in the three liquids. We emphasize again that to obtain physically comparable distributions, the physical sizes of the solvent molecules, as defined in the context of the pair correlation functions, must be used.

The void distribution for the LJ liquid is peaked at a size slightly larger than one LJ diameter, and this size increases slightly as temperature is increased. The lowest temperature distribution is slightly skewed, and the skewness decreases as temperature is increased.

The distributions for SPC/E water are also peaked at cavity sizes slightly larger than one solvent diameter, and the average size increases with increasing temperature. Due to the larger range of the stable liquid region in the water phase diagram, the separation between the locations of the peaks at the lowest and highest temperatures considered is greater in water than in the LJ liquid. The distributions are overall more symmetric than those in the LJ liquid.

The peaks in the void distributions for the Jagla liquid are again on the order of one solvent diameter, and the increasing cavity size with temperature

trend is observed. Like water, the difference between the average cavity sizes at the highest and lowest temperatures is more pronounced than the same for LJ liquid due to the broader stable liquid region of the Jagla phase diagram. The Jagla distributions are considerably more skewed than either the LJ liquid or SPC/E distributions for all temperatures.

Further differences between the three fluids emerge from a comparison of each of the cavity size distributions to the same for a *corresponding hard sphere system* (dotted lines in Fig. 4.3), which is defined as a system of hard spheres at the same number density and with the same hard-core diameter as the corresponding solvent distribution. Similar comparisons have been made to suggest that water accommodates solvophobic compounds more readily than simple atomic liquids due to its greater propensity to form "clusters" (regions of higher than average density) which broaden the cavity size distribution [85, 86]. The results presented here, calculated using a different reference system, are consistent with that view, although less pronounced. Specifically, we find that the LJ liquid cavity distributions are nearly identical to those of their corresponding hard sphere systems at all temperatures, while the distributions for SPC/E water are broader than their corresponding hard sphere systems, suggesting greater density inhomogeneity in water relative to hard spheres or LJ fluid. The Jagla distributions are also slightly broader than the corresponding hard sphere systems at all temperatures studied, indicating that the Jagla liquid also has a similar tendency, although the nature of the driving force for clustering appears to differ from water. Jagla particles prefer to push

one another away to a separation corresponding to the potential minimum, whereas water molecules that H-bond prefer to be at short separation.

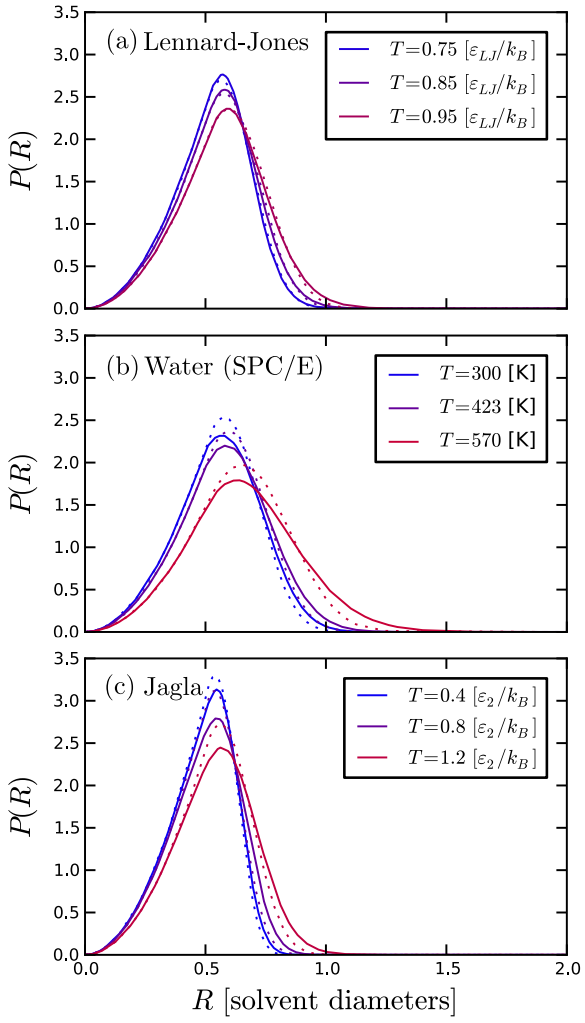

Figure 4.3: Cavity size distributions for selected states along the saturation curves of each of the three liquids (solid lines). $P(R)$ is the probability that the largest cavity that may be inserted at a randomly located point in solution is of size R. Cavity distributions for corresponding hard sphere systems (dotted lines) are also shown. The corresponding hard sphere systems have the same number density and the same hard-core diameter as the solvent (*i.e.*, the same void fraction).

4.3.3 Density Fluctuations

A characteristic of water that has proven useful in theories of the hydrophobic effect is that density fluctuations for molecularly sized volumes obey Gaussian statistics to a good approximation [19, 48, 49, 71]. This behavior permits accurate estimation of p_0 and therefore cavity solubilities from only the first two moments of the p_n distribution (the probability of finding exactly n centers in the volume). The moments, $\langle n \rangle$ and $\langle n^2 \rangle$, may be estimated from knowledge of pair distribution functions, *i.e.*,

$$\langle n \rangle = \rho V \tag{4.1}$$

$$\langle n^2 \rangle = \langle n \rangle + \rho^2 \int_V d\mathbf{r} \int_V d\mathbf{r}' g(|\mathbf{r} - \mathbf{r}'|), \tag{4.2}$$

where V is the cavity volume. p_0 is then given by

$$p_0 \approx \frac{1}{\sqrt{2\pi\sigma_n^2}} \exp\left(-\langle n \rangle^2 / 2\sigma_n^2\right), \tag{4.3}$$

where $\sigma_n^2 = \langle \delta n^2 \rangle = \langle n^2 \rangle - \langle n \rangle^2$ is the mean square occupancy fluctuation.

Although Gaussian-based theories of density fluctuations in water have been successful in describing the solvation properties of small hydrophobes, it is not abundantly clear why occupancy distributions for small volumes in liquids should obey Gaussian statistics. After all, the average number of molecules fluctuating in and out of molecularly-sized volumes is not nearly large enough to appeal to the central limit theorem. In addition, for the limiting cases of very small and very large cavities density fluctuations are known *not* to obey Gaussian statistics. It was first pointed out by Stillinger that the solvation

properties of hard spheres much larger than the size of a water molecule could be quantitatively predicted by assuming that the solvation process consists of two steps: cavitation in a region large enough to accommodate the solute and subsequent insertion of the solute into the vaporized volume [83]. Gaussian statistics dramatically *underestimate* the probability of these large-scale density fluctuations [44]. Furthermore, in the limiting case of volumes smaller than the solvent molecule, the Gaussian prediction is known to *overestimate* p_0 [34, 50]. Given these facts, it is reasonable to question whether the Gaussian behavior observed in water arises fortuitously or whether there is a fundamental physical reason why it is observed.

We have computed the p_n distributions for the LJ liquid, SPC/E water, and the Jagla liquid for cavity volumes equivalent to the solvent size at states along the saturation curves of the three liquids. The results are shown in Fig. 4.4. The Gaussian behavior of p_n in water is clearly observed in Fig. 4.4 (b), where the Gaussian estimate is accurate for all occupancy numbers at all thermodynamic states. The Gaussian estimate for the LJ and Jagla liquids is accurate only near the peaks of the p_n distributions, and significant deviations are seen in the tails, particularly for low-temperature states. In the Jagla liquid, p_0 is overestimated by the Gaussian prediction by more than four orders of magnitude at the lowest temperature considered. The differences between the temperature-dependence of the Gaussian estimates for p_0 in the three liquids is seen more clearly in Fig. 4.5 (a). Gaussian estimates of p_0 for solvent-sized cavities are accurate over all saturation states in water, while

they are poor in the LJ and Jagla liquids except for the highest temperatures. It should be noted that the more skewed the $P(R)$ distribution (Fig. 4.3), the poorer the Gaussian estimate in the LJ and Jagla liquids [1].

It has been demonstrated that the Gaussian estimate for p_0 in water becomes unreliable for cavity sizes approaching 0.5 nm [73]. Fig. 4.5 (b) shows the size dependence of p_0 in the three liquids plotted along with the Gaussian estimates. In the case of SPC/E water the Gaussian estimate for p_0 is in good agreement with the CEOS data for cavity sizes less than about 1.5 water diameters. For small cavity sizes in the Jagla liquid the Gaussian assumption overestimates p_0. This trend reverses at about 2.2 Jagla diameters, where dewetting of cavities becomes increasingly important. Consequently, Gaussian estimates increasingly underestimate p_0 as the cavity size grows larger. The same behavior is seen for the smallest cavities in the LJ liquid, but with the reversal occurring at quite small sizes, about 1.3 LJ diameters.

The first four standardized moments of the p_n distributions for the three liquids are plotted in Fig. 4.6. There are slightly more particles in solvent-sized volumes in the Jagla liquid than in the LJ liquid or SPC/E water, and fluctuations are also consistently larger. For macroscopically large cavity volumes, the isothermal compressibility is related to the variance in occupancy number through $\sigma_n^2 = \langle n \rangle \rho k_B T \kappa_T$. This relation has not been demonstrated to hold true for molecularly-sized cavity volumes, but it is reasonable to sus-

[1] Note that $p_0(R) = \int_R^\infty P(r)dr$.

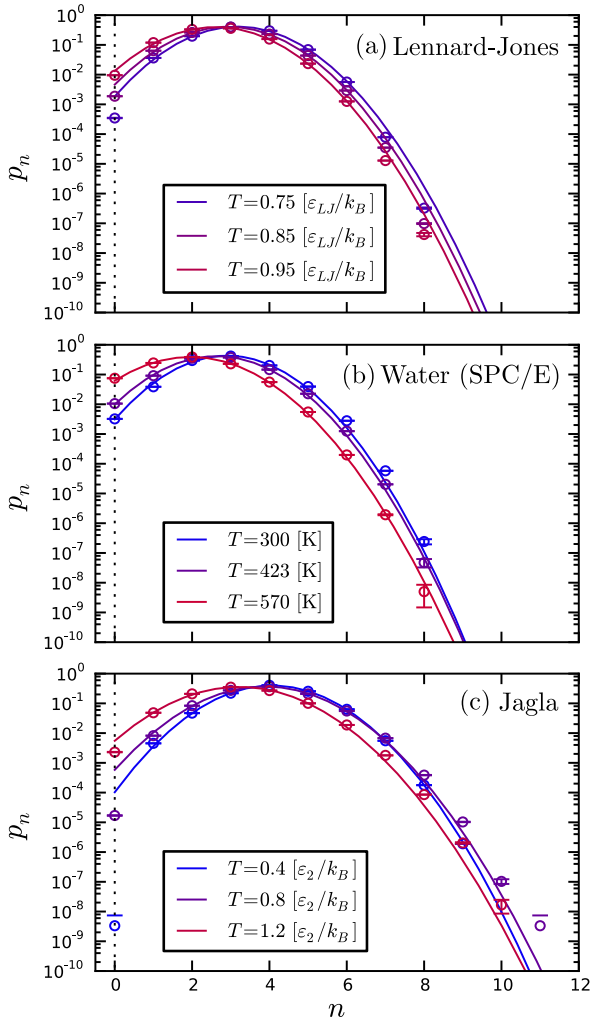

Figure 4.4: The probability of observing exactly n solvent centers in a spherical, solvent-sized cavity along the saturation curves of each of the three liquids. Open circles are simulation data obtained from test-particle insertion. Solid lines are Gaussian estimates of p_n, where the mean, $\langle n \rangle$, and variance, $\sigma_n^2 = \langle \delta n^2 \rangle = \langle n^2 \rangle - \langle n \rangle^2$, are calculated from simulation data and Eq.'s (4.1) and (4.2). The Gaussian estimate for p_0 is poor at low temperatures in both the Jagla and LJ liquids.

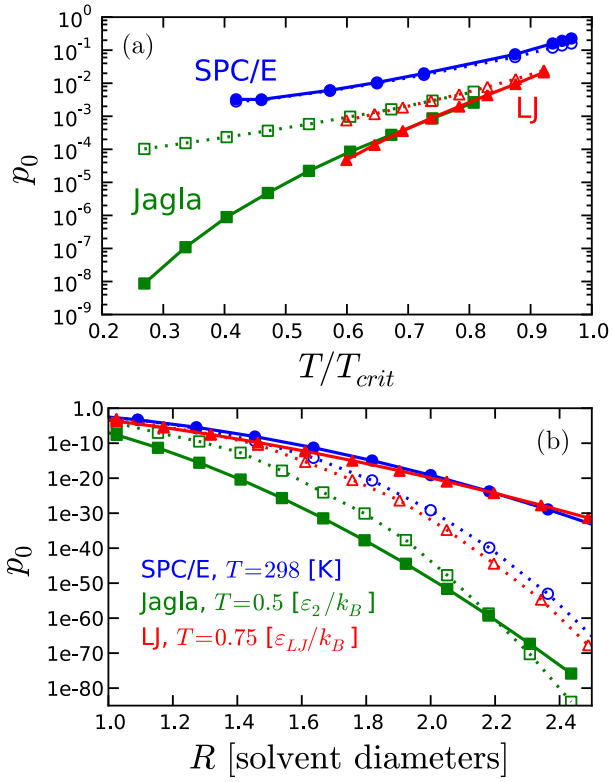

Figure 4.5: (a) $p_0(R)$ for a solvent-sized cavity as a function of temperature along the saturation curve of each of the LJ liquid, SPC/E water, and the Jagla liquid ranging from the triple point to the critical point (T_{crit}). Open symbols are the Gaussian predictions of p_0. Closed symbols for the Jagla and LJ liquids are obtained from simulation data and test particle insertion. Lines are guides to the eye. (b) p_0 plotted as a function of the cavity size for a low temperature state on the saturation curve of each liquid. Closed symbols for the Jagla and LJ liquids are obtained from test particle insertion and revised scaled particle theory, while closed symbols for water are obtained from the cavity equation of state.

pect that the soft ramp of the Jagla liquid may be responsible for a greater compressibility.

The most significant differences are seen in the skewness and kurtosis

of the distributions. Note that a Gaussian distribution has zero skewness and zero kurtosis. SPC/E water first becomes less skewed as temperature increases and then more skewed as the temperature approaches the critical point, while the skewness progressively increases in both the Jagla and LJ liquids. Furthermore, the skewness is always positive in SPC/E water, indicating more probability at low occupancy states for all temperatures. Low temperature states in the LJ liquid and the lowest temperature state in the Jagla liquid on the other hand have negative skewness, or relatively reduced probability of low occupancy numbers, consistent with earlier data. The kurtosis is positive (indicating tails narrower than Gaussian) for the low temperature states of SPC/E water and the Jagla liquid. As temperature is increased, the tails of the p_n distributions of SPC/E water grow fatter at a much higher rate than either the LJ or Jagla liquids. It is interesting to note that none of the distributions shown satisfy those criteria.

A recent study of occupancy statistics in a family of modified water models also reveals that Gaussian density fluctuations are not generally observed in liquids [63]. The authors show that as the hydrogen bond in SPC/E water is systematically weakened, the Gaussian estimate for p_0 becomes poor. Interestingly, destroying the tetrahedral network by bending the water molecule while maintaining interaction strength does not significantly affect the accuracy of the Gaussian estimate for p_0. Thus, it seems that the liquids studied which have extensive hydrogen bonding and/or electrostatic interactions tend to obey Gaussian statistics while those lacking such interac-

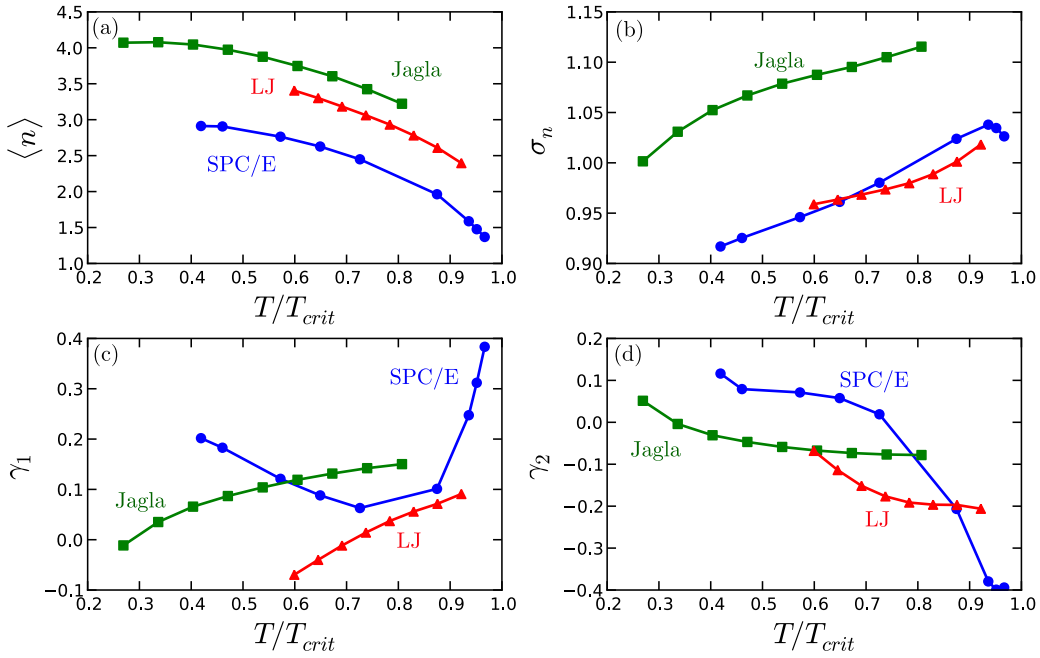

Figure 4.6: Standardized moments for the occupancy distributions in Fig. 4.4: (a) mean occupancy number, $\langle n \rangle = \sum np_n$, (b) width, $\sigma_n = \sqrt{\sum (n - \langle n \rangle)^2 p_n}$, (c) skewness, $\gamma_1 = \sum (n - \langle n \rangle)^3 p_n / \sigma_n^3$, and (d) kurtosis, $\gamma_2 = \sum (n - \langle n \rangle)^4 p_n / \sigma_n^4 - 3$.

tions do not. Further theoretical and simulation work is needed to ascertain whether there is a fundamental physical origin of the Gaussian behavior in networked liquids or whether it is fortuitous. One possible calculation that could shed light on the issue is the calculation of p_n for "Molinero water" (mW) [66], which is a spherically symmetric model that contains a three body term to enforce a preference for tetrahedral structure. Thus, like the Jagla and LJ liquids, it is short-ranged, but it is also water-like in its tetrahedral structure.

4.4 Conclusions

Molecular-level structure, void space, and density fluctuations in the LJ liquid, SPC/E water, and the Jagla liquid were investigated using MC simulations. The results show that while some similarities may exist, each liquid has its own character.

The pair distribution functions for several saturated liquid states were presented for each liquid. The solvent size was estimated as the minimum pair separation at which $g(r)$ is unity. In the LJ liquid, this closely corresponds to the LJ sigma parameter, σ_{LJ}, in SPC/E water it is 0.26 nm, and in the Jagla liquid it is $\sigma_{JG} = 1.56r_0$. The $g(r)$ plots for the Jagla liquid reveal a strong preference for molecular configurations that maximize the number of Jagla particles at a separation corresponding to the potential minimum, r_1. This preference increases with decreasing temperature. The pair distribution functions for solvation shell Jagla particles were investigated for small and large cavities and compared to the bulk pair distribution functions. The solvation shell of large cavities is depleted relative to bulk densities. In addition the solvation shell of large cavities is slightly depleted, relative to the bulk, of particles interacting repulsively. The number of particles separated by the potential minimum is not as depleted however, which is consistent with the ideas presented in Chapter 3 on the origins of water-like enthalpy and entropy.

The void distributions for the three liquids were compared to those of corresponding hard sphere systems (systems of hard spheres with the same void fraction as the solvent). The void distribution in the LJ liquid was indistin-

guishable from that of its corresponding hard sphere system, while the SPC/E water void distributions were slightly broader, revealing a greater propensity for density inhomogeneities in SPC/E water than a hard sphere system or LJ liquid. The Jagla liquid, like water, tends to cluster slightly more than its corresponding hard sphere system. Low temperature cavity size distributions in the LJ and Jagla liquids are skewed, and the skewness decreases with increasing temperature.

Occupancy distributions for molecular-scale volumes were measured and compared to Gaussian predictions. While the Gaussian predictions for p_0 in SPC/E water are accurate across all thermodynamic states considered, p_0 is consistently less than what would be expected if density fluctuations in the LJ and Jagla liquids were Gaussian. The deviation from Gaussian behavior worsens as temperature is lowered. It is noted that the greater the skewness of the cavity size distribution, the worse the estimate for p_0.

Gaussian estimates for p_0 are accurate in SPC/E water for cavity volumes ranging from 1.0 to 1.5 water diameters (or 0.26 to 0.40 nm). The Gaussian estimate underestimates p_0 for large volumes in all three liquids. Solvent-sized volumes are overestimated by Gaussian predictions in the LJ and Jagla liquids. The results suggest that the Gaussian behavior seen in the density fluctuations in molecular-sized volumes in water is not a general feature of liquids.

Chapter 5

The Length Scale Crossover and the Thermodynamic Stability of Solvophobic Aggregates

5.1 Introduction

Over the last several decades apolar solvation and the interaction of hydrophobic solutes in aqueous media have attracted considerable attention as a result of the discovery of the importance of hydrophobic phenomena in biological assembly and the advances in computer simulation technology [5, 54, 87]. Much of the recent research focuses on understanding the peculiar temperature and pressure dependence of the phase behavior of proteins and assemblies of amphiphilic molecules. Although much progress has been made in connecting this behavior to basic theories of hydrophobic solvation [34, 47, 72], controversy still exists over the importance of the scaling behavior of solvation free energies with solute size to hydrophobic stabilization. For example, the "iceberg" picture of Frank and Evans, which attributes the negative solvation entropy of small hydrophobes in water to ordered, ice-like clathrate structures around the solute, is seen as overly simplistic. Although clathrate-like structure may exist [106], the hydrogen bond (H-bond) structure is flexible and still undergoes considerable fluctuations in adjacent solvation shells [5]. In addition, at larger

length scales, the relevance of the "dewetting transition" to the aggregation of extended hydrophobic surfaces has generated much debate [5, 18, 21, 22, 70]. That interfaces between idealized hydrophobic surfaces and water share similarities with the liquid-vapor interface is well established [59, 83, 100], but the presence of weak van der Waals attractions, surface roughness, and surface heterogeneity in realistic interfaces is believed in general to suppress the formation of a microscopic vapor layer [35–37, 76]. However, there is consensus emerging over the general behavior of hydrophobic solvation at small and large length scales. Molecular-sized solutes are able to fit into available space in liquid water's H-bonding network without disrupting H-bonds, and the free energy cost for solvation of these small hydrophobes is entropic in origin. Larger solutes on the other hand, disrupt the H-bonding network and necessitate the formation of an interface that, at ambient conditions, is analogous to the liquid-vapor interface in terms of its structure, fluctuations, and free energy cost of its formation [13, 45, 69, 100].

In the present chapter, we investigate the temperature and pressure dependence of the scaling behavior of the solvation free energies of cavity solutes with cavity size in the Jagla liquid. To gain a clearer picture of what is particular to water-like solvation, and to keep consistent with previous chapters, we compare this behavior to the same in the Lennard-Jones (LJ) liquid and in water using the cut-shifted LJ potential and cavity equation of state (CEOS) [6], respectively. Furthermore, we build upon simple models for aggregation presented by Chandler [18] and Rajamani *et al.* [73], to make quali-

tative arguments about the stability of solvophobic aggregates in the pressure-temperature plane. In addition, we consider the effect that weak attractive interactions have on this picture of solvophobic stabilization.

This chapter is organized as follows. In Section 5.2 we outline the details of the additional simulations used to generate results for our analyses in the present chapter, *viz.*, we describe MC simulations at high pressures in the Jagla liquid. Section 5.3 first presents results for the temperature and scaling behavior as a function of solute size of solvation free energies in the LJ liquid, water, and the Jagla liquid. Two definitions of the "crossover" in solvation free energy from small to large cavities are presented and discussed. A simple model for aggregation is introduced and used to qualitatively describe the effects of these scaling behaviors on the thermodynamic stability of solvophobic aggregates. Arguments for why cold-induced dissociation occurs in water-like liquids are presented, and the effects of pressure and weak attractions are also investigated. Conclusions and future directions are given in Section 5.4.

5.2 Methods

In addition to the MC simulations of cavity formation in the saturated LJ and Jagla liquids presented in Chapter 3 (Tables A.2, A.3, A.6), two sets of MC simulations were performed for several pressures along the $T = 0.6$ isotherm of the Jagla liquid. In the first set of simulations, a pure Jagla liquid system of $N = 1000$ Jagla particles was simulated in the NPT ensemble at the following pressures: $P = P_{sat}(1.4 \times 10^{-4}), 0.10, 0.15, 0.20, 0.25, 0.30$. The

system was equilibrated for 1×10^5 MC cycles, where each cycle consists of N MC moves. In each MC move, there is a $1/N$ chance of attempting a volume move and $(N-1)/N$ chance of attempting to move a randomly selected particle. Frames were output every 5 cycles and analyzed to obtain the bulk solvent density and the insertion probabilities for cavity volumes ranging from 0.5 to 2.0 times the size of the Jagla particle. Table B.1 lists the results and details of the pure Jagla liquid simulations.

In the second set of calculations, isothermal-isobaric MC simulations of a single cavity in the Jagla liquid were performed for each of the states listed in Table B.1. Each system was equilibrated for 2×10^5 MC cycles and then run for 1×10^6 MC cycles for collection of statistics. Cavities diameters up to $10\sigma_{JG}$ were considered, and the contact correlation function was measured for each cavity at each state point. The contact correlation function is determined by extrapolating the cavity-solvent pair correlation function to contact. Table B.1 lists the cavity sizes and number of Jagla solvent particles used in each of the systems. The contact correlation data and insertion probabilities are then fit to Eq. (3.6), and the cavity excess chemical potential is computed from Eq. (3.5).

5.3 Results and Discussion

5.3.1 Temperature Dependence and Scaling of Solvation Free Energies with Solute Size

We now compare the qualitative changes in the temperature dependence and scaling with cavity size of cavity solvation free energies in the three liquids. The general features of the scaling of the excess chemical potential with cavity solute size are depicted in Fig. 5.1. We first consider the behavior for the smallest cavity sizes. Recalling the definition of the cavity radius from Eq. (2.27), we see that cavities of size $R = \sigma_v/2$ are actually hard points, *i.e.*, hard spheres of zero radius. The cavity insertion probability, $p_0(R)$, is in general given by the ratio of the free volume, V_{free} (the sum of the volume that can accommodate the cavity) to the total system volume, V_{tot}. In the case of a hard point, the free volume is equivalent to the void fraction, *i.e.*, $V_{free} = 1-\eta$, where $\eta = N_v V_v/V_{tot}$ is the packing fraction. Here, N_v is the number of solvent particles and $V_v = 4\pi(\sigma_v/2)^3/3$ is the effective solvent volume. Cavities of size $0 < R < \sigma_v/2$ correspond to hard spheres with negative diameters. The free volume for cavities in this size range is equivalent to the void fraction seen by a hard point in a solvent with an effective hard core diameter of $\sigma_v' = 2R < \sigma_v$. Therefore, in the limit of these very small cavities such that only one solvent molecule can fit within the cavity boundary, the insertion probability is given by [2]

$$p_0(R) = 1 - \eta(R), \tag{5.1}$$

where $\eta(R) = 4\pi\rho R^3/3$ is the packing fraction of a system of hard spheres at the solvent's liquid number density, ρ, and with a hard-core diameter given by $\sigma_v' = 2R$. Inserting this probability into Eq. (3.1) and dividing by the solute surface area gives

$$\begin{aligned}\mu_c^x/4\pi R^2 &= -k_B T \ln\left(1-\eta(R)\right)/4\pi R^2 \\ &\approx k_B T \eta(R)/4\pi R^2 = k_B T \rho R/3, \end{aligned} \tag{5.2}$$

which results in a linear dependence upon R for the solvation free energy per surface area for the smallest cavity sizes. Note that the dependence upon $T\rho$, which is an increasing function of temperature for all three liquids, always causes the excess chemical potential to increase upon heating for a fixed cavity size in all three liquids (even the LJ liquid). If the measure of solubility used is the Ostwald coefficient and the vapor may be treated as ideal, then the solubility scales as $\ln\gamma \propto -\rho R/3$ (see Chapter 2). Therefore, the solubility increases with temperature in the LJ liquid, but may decrease with temperature for water-like liquids due to the nonmonotonic dependence of the density on temperature.

Cavities of molecular-size lead to the most uncertain region. In water the probability of formation of cavities of this size is well approximated by assuming Gaussian statistics in density fluctuations, as shown in Chapter 4. The Gaussian assumption yields the following form for the excess chemical potential,

$$\mu_c^x = k_B T \rho^2 V^2 / 2\sigma_n^2 + k_B T \ln(2\pi\sigma_n^2)/2, \tag{5.3}$$

where $V = 4\pi R^3/3$ is the cavity volume and $\sigma_n^2 = \langle \delta n^2 \rangle = \langle n^2 \rangle - \langle n \rangle^2$ is the mean square occupancy fluctuation. The second term is only logarithmically sensitive to the variance and can be reasonably neglected. Dividing by the cavity surface area and keeping only the first term gives

$$\mu_c^x / 4\pi R^2 \approx 2\pi k_B T \rho^2 R^4 / 9\sigma_n^2. \tag{5.4}$$

The particle number variance, σ_n^2, is only slightly temperature dependent, and is expected to scale approximately linearly with the volume of the solute [18]. Thus, the temperature dependence of μ_c^x is dictated by $T\rho^2$ [49], which for water increases with temperature until around 400 K, and $\mu_c^x/4\pi R^2$ scales linearly with the cavity radius. The Jagla and LJ liquids do not in general obey Gaussian statistics for cavity sizes in this range, and thus the functional dependence upon R is uncertain.

For mesoscopic cavities in low-pressure liquids, scaled particle theory predicts that the solvation free energy per surface area will be dominated by the solvent-cavity interfacial free energy, which, for states near coexistence, is well approximated by the liquid-vapor surface tension, γ_{lv}. Increasing the temperature decreases the excess chemical potential in this size range since γ_{lv} is a decreasing function of temperature.

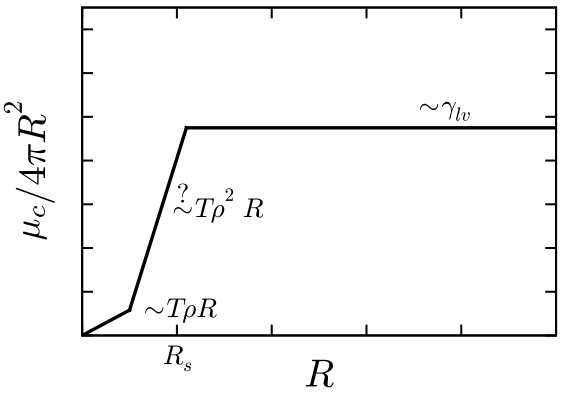

Figure 5.1: Caricature of the temperature and size dependence of the solvation free energies of cavity solutes in liquids. The smallest cavities with $R < 1/2$ may be modeled as hard points (see text). The solvation free energy of these smallest solutes scales linearly with R and has a temperature dependence of $T\rho$. The middle region is less certain; if molecular-scale density fluctuations obey Gaussian statistics, as in water, then the solvation free energy again scales linearly with R but has a temperature dependence of $T\rho^2$. For the largest cavities, the free energy cost of interface formation dominates and the solvation free energy scales with the area of the cavity.

In Fig. 5.2 the solvation free energy scaled by the cavity surface area is plotted versus the cavity size for several temperatures along the saturation curves of the LJ liquid, water, and the Jagla liquid. Cavity diameters ranging from one to over 6 solvent diameters were considered, and the thermodynamic states are the same as those presented in Tables A.2, A.8, and A.6. As seen in Chapter 3, the chemical potential decreases with temperature along the coexistence curve for all cavity sizes considered in the LJ liquid. However, in water and the Jagla liquid, the chemical potential increases with increasing temperature for solvent-sized cavities and decreases with temperature for mesoscopic cavities. Qualitatively, the temperature dependence of the solvation free en-

ergy is identical in the Jagla liquid and water.

An important consequence of the similarities between the temperature-dependence of the solvation free energies in the Jagla liquid and water is that the water-like characteristic of negative solvation entropy for small cavities is observed in the Jagla liquid (Fig. 3.8). As the cavity size increases from $R = 0.5\sigma_{JG}$, the curves along each saturation state first decrease, then pass through a minimum before increasing monotonically for larger cavities. For cavities large enough that $s_c^x|_\sigma > 0$, the solvation shell is more disordered, and for sufficiently large cavities a dewetting transition will occur. This "entropic crossover" from negative to positive solvation entropy may therefore be viewed as a measure of the length scale at which interface formation begins to dominate the solvation free energy. In this view, the crossover for the LJ liquid occurs at cavity sizes less than σ_{LJ} in diameter for all saturation states, which is smaller than the smallest cavities explicitly studied here. In water and the Jagla liquid however, the entropic crossover grows many times larger than the solvent diameter as temperature is decreased, as shown in Fig. 5.3. Although the entropic crossover is similar in the Jagla liquid and water, the crossover in water occurs at sizes larger relative to the solvent diameter.

We now formulate a second definition of the crossover in terms of a simple thought experiment for the aggregation of solvophobic solutes, which combines ideas from Chandler [18] and Rajamani *et al.* [73]. Consider a solvophobic aggregate composed of n identical hard sphere particles with cavity radius r such that the total volume of the aggregate is $V = nv/\eta$, where v is

the volume of a single constituent hard sphere particle and η is the packing fraction of the spheres. If the aggregate is treated as a large spherical cavity of radius R, then Fig. 5.4 (a) shows that the aggregation Gibbs energy of such an aggregate may be modeled as

$$\Delta G = \mu_R - n\mu_r, \tag{5.5}$$

where μ_R is the aggregate's chemical potential and μ_r is the chemical potential of a single constituent solvophobe at infinite dilution. The relationship between the number of hard spheres composing the aggregate and its radius, R, is $n = 4\pi\eta R^3/3v$. Combining the expressions for n and ΔG and dividing by the aggregate surface area, we have

$$\Delta G(R)/4\pi R^2 = \mu_R(R)/4\pi R^2 - \mu_r \eta R/3v. \tag{5.6}$$

The first term on the RHS of Eq. (5.6) is approximately the constant interfacial tension for sufficiently large R [46], and the second term is a linear function of the aggregate radius. The intersection of these two lines is the aggregation radius, R_a—aggregates of size larger than R_a are thermodynamically stable (Fig. 5.4 (b)) within this model free energy. The smaller the constituent hydrophobes, the larger R_a will be. We define a length scale crossover, R_a^{min}, in the context of this model as the size of the smallest thermodynamically stable aggregate, *i.e.*, the smallest aggregate size, R, for which $n\mu_r(r) > \mu_R[R(r)]$, where r is the radius of one of the constituent solvophobes. This relation follows from Eq. (5.5), where we have minimized R under the constraint that $\Delta G < 0$.

Using this definition, the crossover lengths were computed from the simulation data in Fig. 5.2. The results are shown in Fig. 5.5. As expected, the LJ liquid experiences a crossover in solvation behavior on length scales that are smaller relative to the solvent size than the Jagla liquid or water. Moreover, the crossover length is slightly more sensitive to temperature in the water-like liquids.

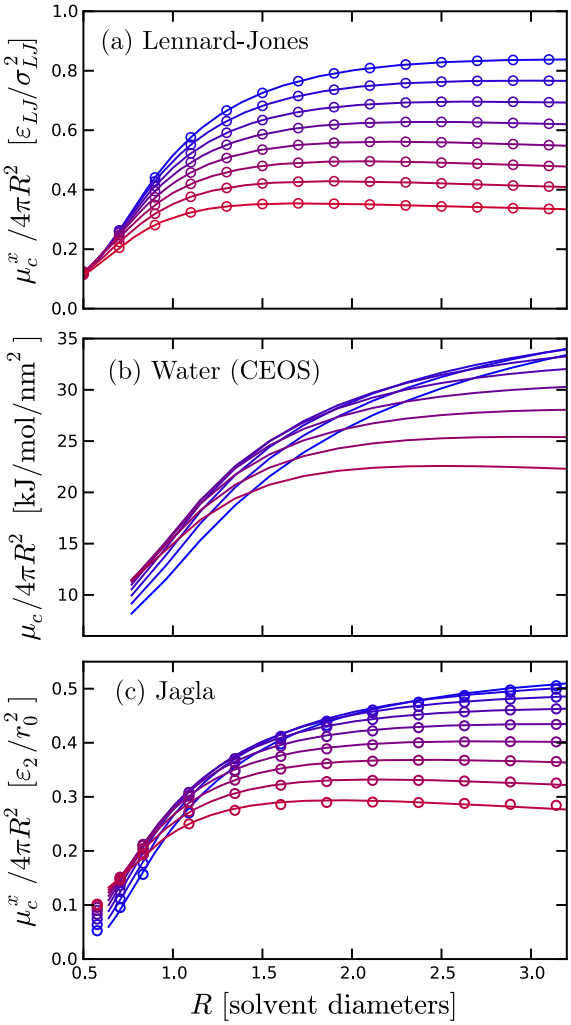

Figure 5.2: Excess chemical potential per surface area versus cavity size for states along the saturation curves of (a) the LJ liquid, (b) water, and (c) the Jagla liquid. Temperatures range from the triple point (blue) to just below the critical point (red). Points in the Jagla and LJ plots are obtained from simulation data and scaled particle theory. Lines in the LJ plot are fits using Eq. (3.19), while lines in the Jagla plot are fits of the simulation data to the cavity equation of state [Eq. (3.12)]. Lines in (b) are predictions for water from the cavity equation of state [6].

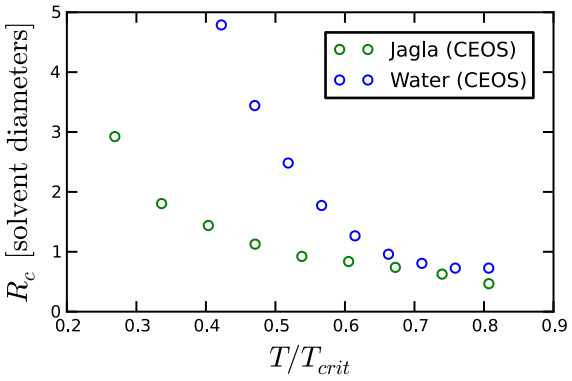

Figure 5.3: Entropic crossovers for cavity solutes in the Jagla liquid and water as predicted by the cavity equation of state. The crossovers are plotted as a function of reduced temperature (T_{crit}) is the liquid-vapor critical point). Open circles indicate the cavity radius at which the solvation entropy changes sign from negative to positive. The crossover lengths are scaled by the size of the solvent molecules. The entropic crossovers for cavities in the LJ liquid occur at cavity radii less than 0.5 for all states on the saturation curve (not shown).

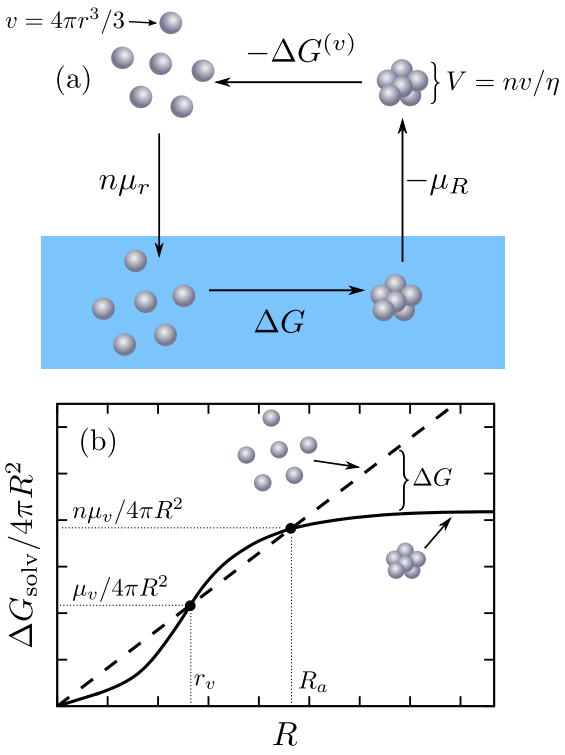

Figure 5.4: (a) A thermodynamic cycle for aggregation / dissociation of hard sphere solutes. The aggregate is modeled as a single large cavity with a volume equal to the sum of the volume of the constituent spheres divided by a packing fraction. Note that $\Delta G^{(v)}$ is zero for hard spheres. (b) Solvation free energy per surface area for the aggregate (solid line) and dispersed solvophobes (dashed line). Only aggregates larger than the aggregation radius, R_a, are thermodynamically stable.

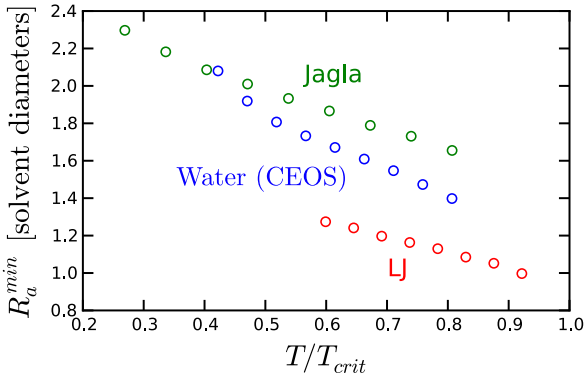

Figure 5.5: The length scale crossover, R_a^{min} (in units of solvent diameters) plotted as a function of reduced temperature, T/T_{crit}, where T_{crit} is the liquid-vapor critical point. In this context, the length scale crossover is defined as the minimum aggregate size for which $n\mu_r(r) > \mu_R[R(r)]$ (see text and Fig. 5.4).

5.3.2 The Thermodynamic Stability of Solvophobic Aggregates

In order to gain a better understanding of the implications in the differences in the crossover behaviors between water-like and typical liquids, we return to the aggregation model of Eq. (5.6).

5.3.2.1 Effect of Temperature

We first focus on the process of cooling the aggregate from a warm temperature, T_H, to a lower temperature, T_L, and in particular, the effect that this process has on the thermodynamic stability of the aggregate.

A qualitative picture of the dependence of the aggregation radius, R_a, on temperature for a water-like and a reference LJ-like fluid is shown in Fig. 5.6. The differences in crossover behavior arise due to the fact that for small solutes in water-like solvents, increasing the temperature decreases the solubility. This has two effects: the first is that the crossover length scale is more sensitive to temperature, and the second is that the slope of the dispersed solvophobes line for high temperature is greater than the corresponding line at low temperature. These effects combine to produce a range of aggregate sizes that are thermodynamically stable at T_H but become unstable upon cooling a to T_L. It is interesting that such a region also appears in a typical LJ-like liquid. However, the crossover length scale in LJ-like liquids is less sensitive to temperature and the slope of the dispersed solvophobes line is greater at lower temperatures, causing the region of destabilization to shrink or altogether disappear. Fig. 5.7 shows quantitative measures of the dissociation

size range in the LJ and Jagla liquids for cavities equivalent to the solvent size and aggregate packing fractions equivalent to the solvent packing fraction. The dissociation region in the Jagla liquid is orders of magnitude larger than that in the LJ liquid. Note that aggregates of a sufficiently large size should not cold-dissociate since the hard sphere fluid is immiscible with both model liquids (a planar interface is thermodynamically stable).

It is important to note that the model describes only the stability of an aggregate of size R, and says says nothing about the stability of an aggregate of size $R + \Delta R$, *i.e.*, an unstable aggregate could become stable by swelling to the stable aggregate size at the given temperature. An interpretation of cold-induced dissociation in this model that follows is that if the required amount of swelling is such that the solvent particles may interpenetrate the void space, then the aggregate will dissociate. Thus, the key difference between water-like and typical liquids in this context is that in water-like fluids the destabilization region is sufficiently wide to preclude the possibility of swelling to the stable aggregate radius without solvent penetration.

In general, the range of the destabilization region is extended by cooling to lower temperatures or by composing aggregates of smaller constituent particles. A prediction made by this model is the possibility of cold-induced dissociation of solvophobic aggregates in LJ-like solvents. Aggregates composed of sufficiently small cavity solutes will in fact, in this model, have a range of sizes for which cooling will destabilize the aggregate and induce its thermodynamic decomposition. It would indeed be striking if such a limit were

faithfully captured by this thought experiment in spite of its overall simplicity.

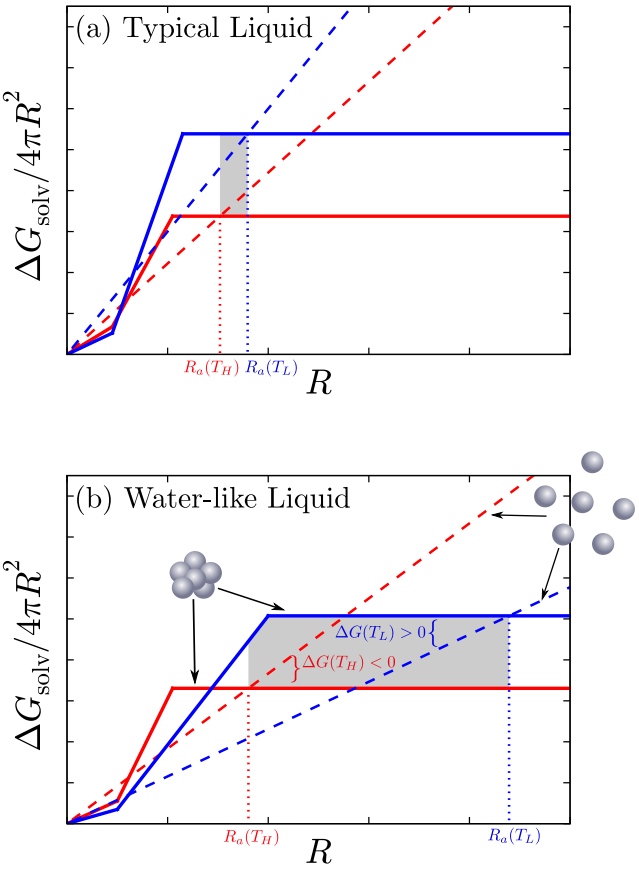

Figure 5.6: Qualitative depiction of solvation free energy per surface area of large solvophobic aggregates and dispersed small solutes in (a) typical and (b) water-like solvents. Red and blue correspond to warm (T_H) and cold temperatures (T_L), respectively. Solid lines correspond to the solvation free energy per surface area of a cavity of size $V = 4\pi R^3/3$, which is used to model an aggregate of $n = V/v$ smaller cavities of size $v = 4\pi r^3/3$, where r is the size of the solvent particle. Dashed lines represent the solvation free energy per aggregate surface area of the n constituent solvophobes dispersed in solution. The shaded region highlights the aggregate size range where cooling from T_H to T_L destabilizes the aggregate.

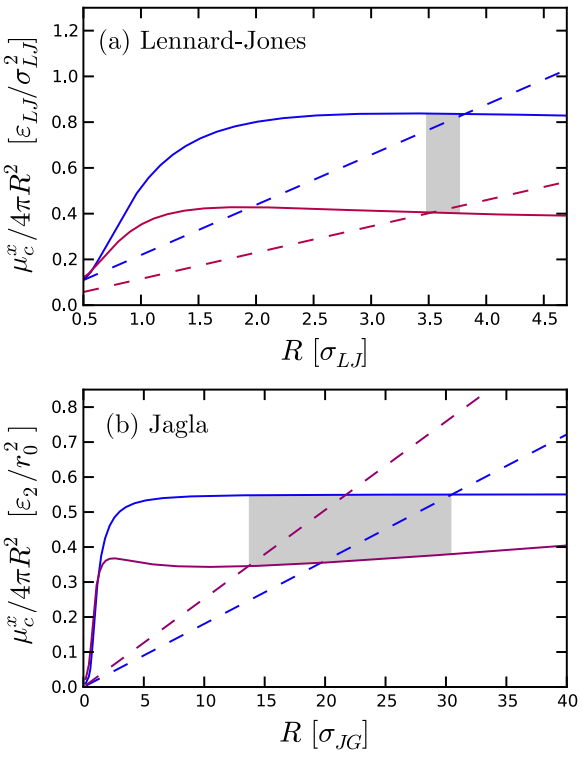

Figure 5.7: The specific case of Fig. 5.6 for the temperature dependence of solvophobic solvation free energies in (a) the LJ liquid for $T = 0.65$ (blue) and $T = 0.95$ $[\varepsilon_{LJ}/k_B]$ (red) and (b) the Jagla liquid for $T = 0.4$ (blue) and $T = 1.0$ $[\varepsilon_2/k_B]$ (red). The constituent solvophobes are equivalent in size to the solvent diameter and the aggregate packing fraction is taken equivalent to the solvent packing fraction. Both liquids have a range of cavity sizes (shaded region) where cooling from the warm temperature (red lines) to the cool temperature (blue lines) destabilizes the aggregate (solid lines) relative to the dispersed spheres (dashed lines). The size range in the Jagla liquid is far more pronounced, however (note the order of magnitude difference in the abscissa scales).

5.3.2.2 Effect of Pressure

We have seen that temperature affects the stability of solvophobic aggregates and that not only will heating cause dissociation, but under certain circumstances, cold-induced dissociation may also occur. Another well-known factor influencing the stability of hydrophobic aggregates is pressure. For example, globular proteins, which are widely believed to be stabilized by hydrophobic forces [87], may be denatured at pressures of a few hundred MPa [81]. The negative volume change upon unfolding is explained by considering the transfer of water to an apolar phase instead of the converse [47].

For sufficiently high pressures, the pressure-volume term in Eq. (3.4) is expected to dominate the solvation free energy. When scaled by the cavity surface area, this term becomes linearly dependent on the cavity radius. Although structural and dynamic properties are expected to be anomalous functions of pressure for low temperature states in water-like liquids [103], we do not expect qualitative differences in the behavior of μ_c^x as a function of pressure along isotherms in the three liquids compared in this study. We have therefore only computed high pressure cavity solvation properties for the Jagla liquid.

Using revised scaled particle theory, we have computed the solvation free energy of cavities ranging from one to ten σ_{JG} in diameter for several pressures along the $T = 0.6$ isotherm in the Jagla liquid. The results for the fit of the RSPT equations to the contact correlation function are presented in Table B.3. The interfacial free energy increases monotonically as pressure

is increased and reaches a value of more than twice the liquid-vapor surface tension at the highest pressure considered. The first order correction to the interfacial free energy, δ, is strictly positive and also increases monotonically. Although the values reported in our fit provide sufficient agreement with our simulation data for our purposes, it is expected that more accurate estimates of the phenomenological fitting parameters could be obtained if more data points were used near the peak in $G(R)$ where the most pronounced changes occur. At high pressures, the results of the fit are very sensitive to the choice of R_{sim} and R_{large} in Eq. (3.5). Nevertheless, we expect our results to suffice for the current purpose of investigating the qualitative behavior of the solvation free energy as a function of pressure.

Fig. 5.8 (c) shows the values for $G(R)$ measured by MC simulation along with the curves of the RSPT fit. The maximum peak in $G(R)$ increases and sharpens rapidly as pressure is increased. At this temperature, only the lowest pressure, corresponding to the saturation pressure, shows a truly dewet cavity surface for the largest cavities. At the higher pressure states, there is an increased adsorption of solvent at the cavity surface which prevents dewetting.

The excess chemical potential is calculated from Eq. (3.5) and plotted in Fig. 5.8 (a) and (b) (scaled by the cavity surface area). As expected, the pressure-volume term dominates the behavior of the solvation free energy for large cavities at high pressure. This is evidenced by the linear behavior of the scaled solvation free energy for large cavities at high pressure in Fig. 5.8 (b). For a given cavity size, the solvation free energy is approximately linearly

dependent on the pressure, as expected from Eq. (3.4) and the results for γ_∞ in Table B.3.

The effect of pressure on ΔG in Eq. (5.6) is shown in Fig. 5.8 (d). Here, we consider the case of isothermally pressurizing a solvophobic aggregate from the saturation pressure to the highest pressure studied, $P = 0.30$. The constituent solutes are of the same size of the solvent and the packing fraction is chosen equivalent to the solvent packing fraction. We again see the dissociation region that appeared in the temperature dependence plots of Fig. 5.7 (b). The shaded region of the plot represents an aggregate size range where pressurizing from the saturation pressure to $P = 0.30$ causes the aggregate to become thermodynamically unstable with respect to individual solutes. This time the dissociation region results not from the difference in state-dependence of μ_c^x for small solutes, but rather from the substantial difference in the solvation free energies of large cavities due to the PV term in Eq. (3.4).

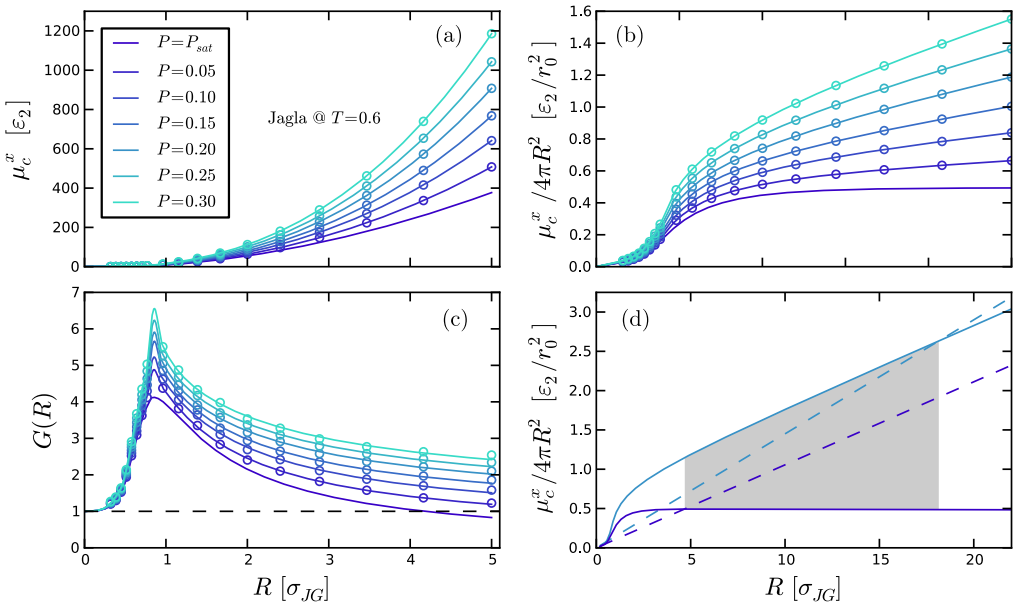

Figure 5.8: Effects of pressure on the solvation of cavity solutes in the Jagla liquid at $T = 0.6$. (a) The excess chemical potential of cavity solvation as a function of pressure and cavity size, and (b) the same scaled by the cavity surface area. Points are obtained from MC simulation data and Eq. (3.2). Lines are obtained from Eq. (3.5). (c) Cavity-solvent contact correlation functions for increasing pressures and cavity sizes. Points are obtained from MC simulations, and lines are fits of Eq. (3.6) to the data. (d) Stability of a solvophobic aggregate using the model from Fig. 5.4. Dashed lines represent the dispersed solvophobes and solid lines the aggregate. The shaded region represents an aggregate size-range where pressurizing at constant temperature from the low (P_{sat}) to the high ($P = 0.3$) pressure destabilizes the aggregate.

5.3.2.3 Effect of Weak Attractive Interactions

Although water is more strongly attracted to itself than to hydrophobic solutes, it nevertheless experiences attractive interactions with even the most hydrophobic entities. It has been shown that, relative to purely repulsive interactions, weak attractions have the effect of increasing the temperature of minimum solubility [33] and increasing the "cold-denaturation" temperature of hydrophobic polymers [4]. In the present section, we investigate the effects of weak attractive interactions on our picture of solvophobic solvation in the Jagla liquid by using the mean-field equations of Section 2.5. In particular, we model the aggregate as a collection of particles that have square-well interactions with themselves and with the Jagla solvent. The square-well hard core diameter is set equivalent to r_0, and the attractive range is $1.5r_0$. To obtain an effective aggregate-solvent interaction potential, we evaluate the mean interaction potential at points ranging from the cavity (aggregate) surface to the point where the potential decays to zero. The resulting potential is well modeled by a triangle well potential (see Fig. 5.9).

Eq.'s (2.40) and (2.41) were applied to the resulting attractive potential for all cavity sizes at high and low temperature states on the saturation curve as well as high and low pressure states on the $T = 0.6$ isotherm. The results are shown in Fig. 5.10. Attractive interactions necessarily make negative contributions to the overall solvation free energy and therefore $\mu_u^x < \mu_c^x$ for all cavity sizes and states considered. The effect is stronger for larger cavities and lower temperatures, as shown in Fig. 5.10 (a).

The resulting effect on the simple picture of cold-induced aggregate dissociation is shown in Fig. 5.10 (b). Note that in the case of attractive solutes, $\Delta G^{(v)}$ is no longer zero in the cycle shown in Fig. 5.4 (a). Therefore,

$$\Delta G = \mu_R - n\mu_r - \Delta G^{(v)}, \tag{5.7}$$

and the shaded region now corresponds to where the difference in the first two terms on the RHS is becomes positive upon decreasing temperature. This range is larger than that for the purely repulsive spheres of Fig. 5.7 (b). The broadening is due to the balance of attraction of many small solutes to the solvent with that for a single aggregate. Although the vapor-phase aggregation term contributes negatively to ΔG, it is insufficient to overcome the driving force for dissociation given by the first two terms for the square-well model considered here. Similarly, Fig. 5.7 (d) shows that weak attractions have the effect of broadening the pressure-dissociation region (again, the $\Delta G^{(v)}$ contribution is insufficient to overcome the difference between μ_R and $n\mu_r$).

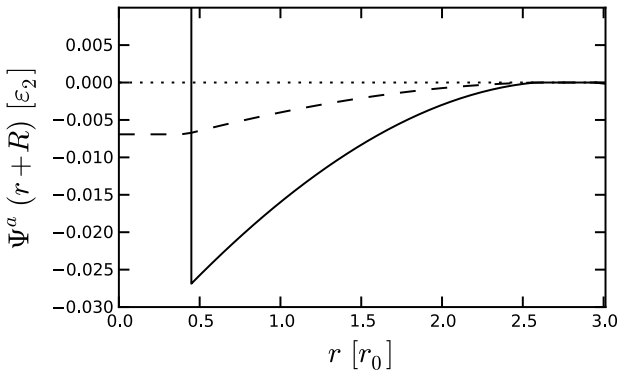

Figure 5.9: The mean attractive potential of an aggregate of square-well particles for an aggregate size of $R = 4.0$. The square well particles have the same hard core diameter as the Jagla solvent particles, r_2 [Eq. (3.13)]. The potential is decomposed according to Eq. (2.36), where the repulsive component is a hard core potential. The solid line is the full potential, and the dashed line is the attractive part of the WCA decomposition.

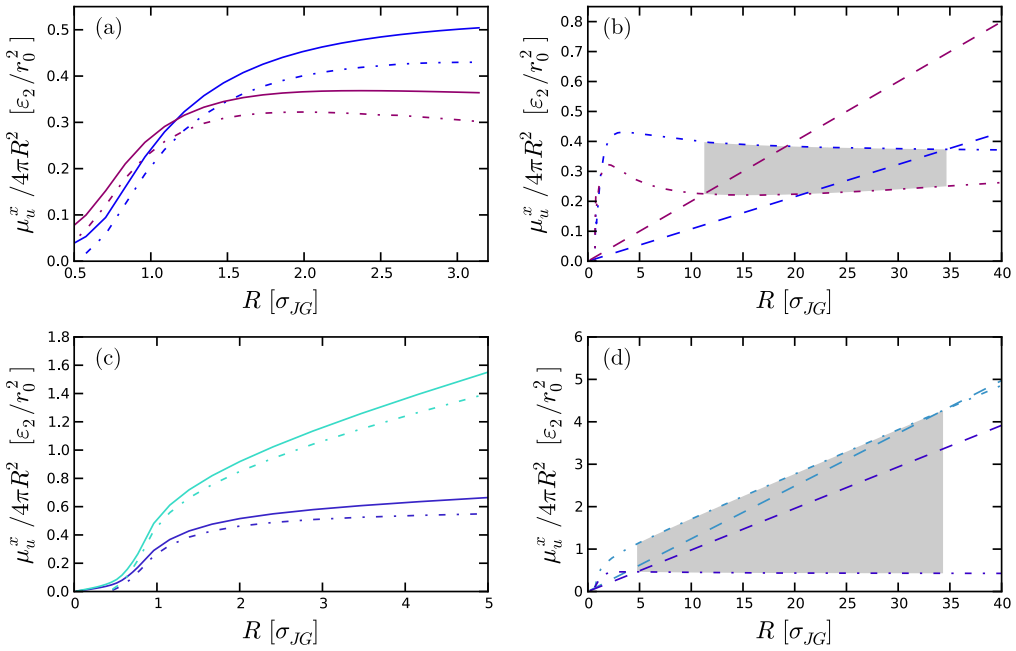

Figure 5.10: Effect of weak solute-solvent attractive interactions on the length scale crossover and the aggregate stability model for states along the saturation curve and the $T = 0.6$ isotherm of the Jagla liquid. Solid lines correspond to cavities and dash-dot lines correspond to weakly attractive spheres. (a) Scaled solvation free energies versus cavity size for temperatures of $T = 0.4$ (blue) and $T = 1.0$ (red) on the saturation curve. (b) Application of the aggregate model in Fig. 5.4 to the curves for attractive spheres in (a). (c) Scaled solvation free energies for pressures of $P = P_{sat}$ and $P = 0.3$ and (d) the aggregate model results for the attractive curves in (c).

5.4 Conclusions

We have demonstrated that the scaling and temperature dependence of the solvation free energies of cavity solutes in Jagla liquid is qualitatively similar to that of water. Both liquids have negative solvation entropies for small cavities that crossover to positive with increasing cavity size. The entropic crossovers for the Jagla liquid occur at a shorter length scale relative to the solvent size than those of water.

Combining ideas from Chandler [18] and Rajamani *et al.* [73], a simple thought experiment for aggregate dissociation was introduced by modeling an aggregate as a single large hard sphere with a volume equal to the sum of the volumes of the constituent spheres divided by a packing fraction. The consequences of the different scaling and temperature dependence of solvation free energies is clearly demonstrated in the context of this simple model for aggregation. It is shown that cold-induced dissociation will occur for aggregates composed of sufficiently small spheres in water-like liquids.

The effects of pressure on the stability of solvophobic aggregates is also investigated in the context of the aggregate model. Large cavities at high pressure have a cubic dependence on the cavity size, which causes the solvation free energy to grow large as pressure is increased from the saturation pressure. This scaling behavior exposes a range of aggregate sizes to destabilization upon pressurization.

Weak attractive interactions are added to the cavity solvation results

using a simple mean-field theory. The results show that attractive interactions broaden the destabilization regions, which is equivalent to increasing the cold-dissociation temperature. Similarly, the range of aggregate sizes exposed to pressure dissociation is broadened, which is equivalent to lowering the pressure required to dissociate an aggregate.

The results are consistent with what is known about the stability of proteins and other assemblies stabilized by hydrophobic interactions. This provides an interpretation of those phenomena in terms of the change in scaling behavior of solvation free energies with hydrophobic surface area, which is connected to changes in interfacial structure.

Chapter 6

Solvent Effects on the Sequence Energy Landscape of Rigid Rod Heteropolymers

6.1 Introduction

In this chapter we will use the Jagla liquid as a proxy to investigate solvent effects on the problem of molecular design—that is, given a target structure of a molecule and an alphabet of monomers, what is the sequence arrangement that produces a stable molecule with the desired structure? This problem is one of the grand challenges of computational biology and protein engineering, as well as materials science; its solution holds promise for far-reaching applications in areas ranging from materials assembly to targeted drug design. The problem poses the formidable tasks of characterizing both the protein configurational space and amino acid sequence space to determine if the target structure is indeed the ground state of a particular sequence. In other words, for each possible sequence, all configurations of the molecule must be searched to determine if the target configuration is thermodynamically stable. For a single N monomer protein composed of the common 20 amino acids, there are 20^N possible sequences that must be searched. Typical proteins are hundreds of monomers long, and the largest protein assemblies contain tens of thousands of amino acids [31]. Characterizing the energy landscape of a single

sequence is no small task, and to date only a small number of proteins have been successfully folded *in silico* using atomistic models and explicit solvent [77].

Thus, due to its extraordinary computational complexity and scope, most models for the design problem have focused on reducing the computational demand by coarse-graining solvent effects through the use of contact potentials, which are in essence monomer-monomer potentials of mean force. One such model is the simple HP model of Lau and Dill [58], which consists of a two-letter alphabet of only hydrophobic and hydrophilic monomers. Hydrophobic pairs within a certain distance make a negative contribution to the overall system energy, and no other types of interactions are considered. Despite its simplicity, the HP model captures the essential features of hydrophobic collapse—those sequences which permit the polymer to largely isolate hydrophobic interactions in the core will form stable globular structures. Contact potentials such as those used in the HP model are valid at only one thermodynamic state however, since potentials of mean force are in general state-dependent [80]. Furthermore, it is known that potentials of mean force are not, in fact, pairwise-additive [94]. Among other things, this means that HP polymers cannot exhibit cold or pressure denaturation.

To gain understanding of the limitations of these assumptions, we seek to characterize the explicit effects of solvent-solute interactions on the *sequence energy landscape* (the energy landscape of all possible sequences for a given target structure) of simple heteropolymers consisting of only solvophilic and solvo-

phobic monomers in the Jagla solvent. The models we use in this exploratory study are extraordinarily simple—the "polymers" are simple rigid rods composed of only Jagla (solvophilic) and hard sphere (solvophobic) monomers. The effects of aggregation on the sequence landscape are investigated by simulating the rods positioned either close together or dispersed at infinite dilution.

It is important to emphasize again that in the present study we are concerned with evaluating the sequence landscape for only two configurations—aggregated and dispersed. Determining the true fitness of a mutation requires an exhaustive exploration of the entire configurational space, and we do not address that here. Nevertheless, we believe such an investigation will prove useful in illuminating the state-dependence of the sequence space [78].

This chapter is organized as follows. Section 6.2 details the sampling methods used to investigate the sequence energy landscape and describes the models used. The results of the explorations of sequence space for two solvent temperatures and two configurational states (aggregated and dispersed) are presented in Section 6.3. Conclusions and future directions are given in Section 6.4.

6.2 Methods

6.2.1 Model Details

The model system is shown in Fig. 6.1. The system consists of two polymer solutes immersed in a solvent of 1600 Jagla particles [Eq. (3.13)] in a cubic box with periodic boundary conditions. The solutes are modeled as rigid

rods composed of ten monomers each. The monomers are selected from a two-letter alphabet consisting of only solvophilic Jagla particles and solvophobic hard sphere particles. The hard sphere (HS) diameter is σ_{JG}. Pairs of Jagla particles interact according to Eq. (3.13), and HS pairs interact according to

$$u_{HS}(r) = \begin{cases} \infty, & r \leq \sigma_{JG}, \\ 0, & r > \sigma_{JG}, \end{cases}$$

where r is the pair separation. Jagla-HS interactions are treated as HS interactions with HS diameter σ_{JG} [see Fig. 3.2 and Eq. (3.13)]. Bonds between monomers are fixed at $1.6r_0$ irrespective of monomer composition. Two configurational states are considered for the pair of rods. The first is the aggregated state, in which the rods are perfectly aligned so that each monomer is separated from its pair in the other rod by a distance corresponding to the minimum in the Jagla potential well depth, r_1. In the second configuration, we separate the rods to a distance sufficiently large to approximate infinite dilution. In both solute configurations, the solvation shell consists of all Jagla solvent particles close enough to interact with either of the solutes [*i.e.*, solvent within r_2 (see Fig. 3.2) of any solute particle].

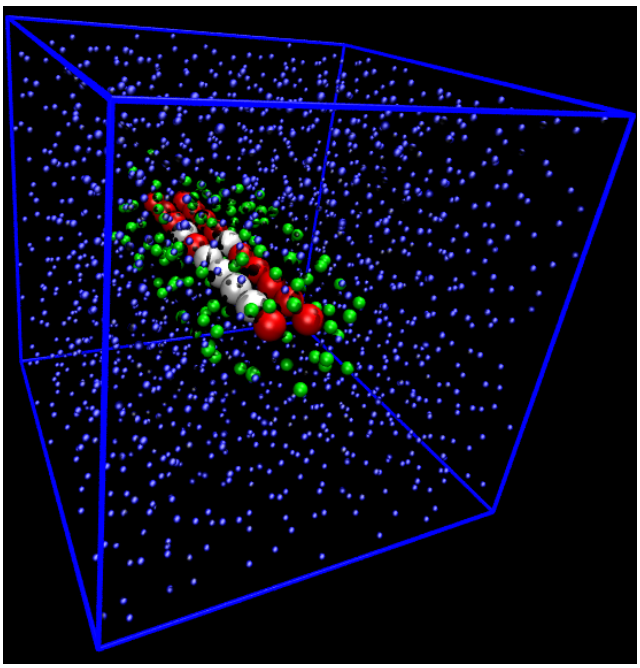

Figure 6.1: Snapshot of a single configuration from a trajectory of aggregated rod-like heteropolymers in Jagla solvent at $T = 0.6$. The two polymers are perfectly aligned atom by atom and separated by a distance corresponding to the minimum in the Jagla well depth, r_1. The bond length of each monomer-monomer pair (for any pairing of Jagla and hard spheres) is $1.6r_0$ (see Fig. 3.2). Jagla monomers are colored red while hard spheres are shown in white. Jagla solvent in the solvation shell, *i.e.*, sufficiently close to interact with the solute, is colored green. The small blue spheres are Jagla solvent sufficiently far from the polymers that there is no solvent-solute interaction. Image generated using VMD [51].

6.2.2 Flat-Histogram Sampling of the Density of States

We first consider the hypothetical case where the is ideal (non-interacting with itself). The sampling methods and derivations presented here closely follow [78]. For each of the two configurations considered in this study, we seek to calculate the distribution in energy of all possible sequences with the Jagla/HS monomer alphabet. We define $\Omega_{seq}(E_{seq})$ as the density of states (DOS) in sequence energy, *i.e.*, the number of states with energy E_{seq}. In our system, the sequence energy, $E_{seq} = E_{uu} + E_{uv}$, where E_{uu} is the solute-solute interaction energy, and E_{uv} is the solute-solvent interaction energy, and includes all terms in the potential energy that depend explicitly on the sequence. The quantity $\Omega_{seq}(E_{seq})$ is analogous to other thermodynamic systems in that it is sharply peaked with a maximum on the order of the total number of states (sequences). Therefore, it is more natural to work with Boltzmann's equation,

$$S_{seq}(E_{seq}) = k_B \log \Omega_{seq}(E_{seq}), \tag{6.1}$$

where k_B is Boltzmann's constant. It should be noted that $\Omega_{seq}(E_{seq})$ counts the number of sequences of energy E_{seq} for a fixed configuration, which is in contrast to the usual configurational DOS which counts the number of configurations with a given energy for a fixed sequence. The same tools of statistical mechanics will still apply to the hypothetical situation considered here, *viz.*, that the polymer backbone is held fixed while its monomers are allowed to mutate. If this system is connected to a heat bath, then the temperature of the system will mediate the observed ensemble of mutated sequences, and each

sequence will appear with a probability weight given by the Boltzmann factor, $\exp(-\beta_{seq}E_{seq})$, where $\beta_{seq} = 1/k_B T_{seq}$. The canonical partition function for the system is then

$$Q(T_{seq}) = \sum_{E_{seq}} \Omega_{seq}(E_{seq}) e^{-\beta_{seq}E_{seq}} = \sum_{E_{seq}} e^{S_{seq}(E_{seq})/k_B - \beta_{seq}E_{seq}}. \tag{6.2}$$

It is useful to approximate the sequence energy distribution as continuous, which is appropriate given the high number density of sequences in the energy ranges we consider. Consequently, the sum in Eq. (6.2) will be dominated by one particular energy E^*_{seq}, whose value is obtained by maximizing the argument of the exponential. This yields the familiar thermodynamic relation

$$\frac{\partial S_{seq}(E_{seq})}{\partial E_{seq}}(E^*_{seq}) = \frac{1}{T_{seq}}. \tag{6.3}$$

Thus, the slope of the sequence entropy curve at that point is the reciprocal sequence temperature, *i.e.*, the temperature at which sequences of that energy are spontaneously produced. This is analogous to the definition of the configurational temperature in classical statistical thermodynamics, only in this situation the sequence composition is being thermalized instead of the configurational degrees of freedom.

Evaluation of the sequence entropy for the rods is computationally demanding. The usual Metropolis MC method would rarely sample compositions with high number fractions of HS's at the solvent conditions in which we are interested. Further, we are interested in the full range of compositions and the situation where each rod has a unique composition. Therefore, we use

a flat-histogram algorithm developed by Shell and Debenedetti [79] to explore the entire range of sequence space. The algorithm is a derivative of the Wang-Landau method [93], and it calculates the entropy directly by continuously adapting an initial guess based on the current state of the system. The method proceeds as follows. At every sequence move, the sequence is altered either by a mutation or by swapping a monomer pair. Mutations and swaps occur with equal probability. Each move is accepted or rejected based on the current estimate for the density of states:

$$\begin{aligned} P_{acc} &= \min\left\{1, \exp\left[S_{seq}(E_{seq})/k_B - S_{seq}(E'_{seq})/k_B\right]\right\} \\ &= \min\left\{1, \exp\left[-\Delta S_{seq}/k_B\right]\right\}, \end{aligned} \tag{6.4}$$

where E_{seq} and E'_{seq} are the initial and final energies, respectively. This criterion ensures a random walk in sequence energy [79, 93], permitting a broad exploration of sequence space. The initial estimate for the sequence entropy is zero everywhere. Over the course of the simulation, as the estimate improves, each sequence energy will be visited with equal probability. This is the criterion for convergence of the sequence entropy estimate. This requires systematic modification of the entropy estimate as the system evolves, which is exactly the Wang-Landau component of the algorithm. The refinement of the entropy estimate works as follows. After each MC step, the entropy of the current energy is incremented by a small amount, g. As the histogram of visited states flattens, this incrementing procedure only serves to shift the entire entropy curve upward. The shifting is ultimately irrelevant because it

only adds a constant to the estimate for the entropy, and we are interested in relative values of the entropy. The parameter g begins at a value of unity, and is tuned over the course of the simulation to successively smaller values. Once the visited states histogram for a given value of g is deemed sufficiently flat, g is modified as $g \leftarrow 0.5g$. In this context, sufficiently flat means that the ratio of the histogram value for the least visited state and the mean value is greater than 80 percent. The simulation is complete when g falls below a value of 10^{-10}.

It is known that although the Wang-Landau method initially explores a large region of phase space, it is slow to converge to an accurate estimate of the DOS [102]. Shell and Debenedetti have therefore augmented the Wang-Landau sampling procedure described above with transition matrix estimators [27, 79, 95]. A matrix of all possible energy pairs, $C(E^{(i)}_{seq}, E^{(j)}_{seq})$ is kept and upon each proposed move from i to j, 1 is added to the corresponding matrix element. As the number of moves grows large, C provides an estimate of the macroscopic move proposal probabilities, $T_{prop}(E^{(i)}_{seq} \rightarrow E^{(j)}_{seq}) \approx C(E^{(i)}_{seq}, E^{(j)}_{seq}) / \sum_k C(E^{(i)}_{seq}, E^{(k)}_{seq})$ [20], which in turn provide estimates for relative values of the entropy:

$$S_{seq}(E^{(i)}_{seq})/k_B - S_{seq}(E^{(j)}_{seq})/k_B = \ln \frac{T_{prop}(E^{(j)}_{seq} \rightarrow E^{(i)}_{seq})}{T_{prop}(E^{(i)}_{seq} \rightarrow E^{(j)}_{seq})}. \tag{6.5}$$

Eq. 6.5 is a consequence of detailed balance and is derived in [79]. In the present algorithm, C is used to provide new improved estimates of the sequence entropy at every change in the value of g for $g < 10^{-5}$.

As previously mentioned, the methods for sampling the sequence energy landscape presented above mirror those presented by Shell and Debenedetti in [78]. In the present calculation however, there is explicit solvent instead of monomer-monomer contact potentials, and we are interested in the effects of solvent conditions on the sequence energy landscape. To generate a flat distribution in the total solvent and solute energy would be largely unproductive. To construct a sampling algorithm that allows us to explore the sequence landscape for a fixed solvent temperature, we first note that the total system energy for a single state with sequence $\mathbf{x}$ and configuration $\mathbf{r}$ may be written in the separable form

$$E_{tot}(\mathbf{x}, \mathbf{r}) = E_{uu}(\mathbf{x}, \mathbf{r}) + E_{uv}(\mathbf{x}, \mathbf{r}) + E_{vv}(\mathbf{r}), \tag{6.6}$$

where the subscripts u and v denote the solute and the solvent, respectively, E_{uu} is the solute-solute interaction energy, E_{uv} is the solute-solvent interaction energy, and E_{vv} is the solvent-solvent interaction energy. We wish to sample the sequence space in such a way that all sequence energies are equally probable, *i.e.*,

$$P_{seq}\{E_{seq}\} = \Omega_{seq}(E_{seq})W_{seq}(E_{seq}) = constant, \tag{6.7}$$

where $W_{seq}(E_{seq})$ is the probability weight factor for a given sequence energy, $E_{seq} = E_{uu} + E_{uv}$. This is achieved with the probability weight factor $W_{seq}\{E_{seq}\} = 1/\Omega_{seq}(E_{seq})$. The solvent degrees of freedom however, are thermalized at the solvent temperature, and thus the weight factor for solvent

configurations is the usual Boltzmann factor,

$$W_{vv}\{E_{vv}\} = \exp\left[-\beta E_{vv}\right], \tag{6.8}$$

where $\beta = 1/k_B T$ is the reciprocal solvent temperature. Noting that the probability weight of a given state for the entire system is $W(E_{tot}) = W_{seq}(E_{seq})W_{vv}(E_{vv})$, detailed balance gives the MC transition probability from a state $(\mathbf{x}, \mathbf{r})$ to a state $(\mathbf{x}', \mathbf{r}')$ as

$$P_{acc} = \min\left\{1, \frac{\Omega_{seq}(E_{seq})}{\Omega_{seq}(E'_{seq})}\exp\left(-\beta\Delta E_{vv}\right)\right\} \tag{6.9}$$

$$= \min\left\{1, \exp\left[-(\Delta S_{seq}/k_B - \beta\Delta E_{vv})\right]\right\} \tag{6.10}$$

where $\Delta E_{vv} = E_{vv}(\mathbf{r}') - E_{vv}(\mathbf{r})$. Note that for solute mutation and swap moves $\Delta E_{vv} = 0$ and for bulk solvent moves $\Delta S_{seq} = 0$.

In addition, since we are interested in a broad range of energies, we expedite the simulation by breaking the total sequence energy space into several windows and running simulations in parallel [20]. Each window slightly overlaps in energy with its neighbors. Periodically, swaps are attempted between configurations of adjacent energy windows to ensure the ergodicity of each simulation. A swap is accepted if both systems have energies in the overlapping region. Each simulation then provides an estimate for the sequence entropy within that particular window. The individual estimates are stitched together by minimizing the following variance,

$$\sigma_{tot} = \sum_{i<j}\sum_{k}\left[S_i(E^k_{seq})/k_B + C_i - S_j(E^k_{seq})/k_B - C_j\right]^2, \tag{6.11}$$

where i and j are the indices of the energy subrange, the constants C_i and C_j are the values by which the entropies are to be shifted, and k is an index for all overlapping points between the i and j energy windows. A more detailed explanation of parallel Wang-Landau methods is given in [20].

6.3 Results and Discussion

The methods described above were applied to model system at two different solvent temperatures, $T = 0.6$ and $T = 1.2$ $[\varepsilon_2/k_B]$. The lowest temperature is "corresponding" to ambient water in that it is near liquid-vapor coexistence, above the temperature of maximum density, and below the temperature of minimum solubility of solvent-sized solvophobes. Six energy windows were used and swaps were attempted every 4 MC cycles. The ergodicity of the simulation is shown in Fig. 6.2. Fig. 6.2 (a) demonstrates that we have achieved random walks in energy for each of the energy windows. Fig. 6.2 (b) shows that the trajectory of a single replica system, *i.e.*, a tagged set of coordinates, moves unpreferentially among the energy windows. This confirms the algorithm is working as expected.

The sequence entropy, scaled by its minimum value, is plotted in Fig. 6.3 for both solvent temperatures and both configurations (aggregated and dispersed). Higher sequence energies indicate a higher fraction of HS's in the sequence (a purely HS solute will have zero sequence energy). At low solvent temperature, the DOS of the aggregate is slightly higher at high energies (high HS fractions) than the dispersed solutes, suggesting that aggregation may

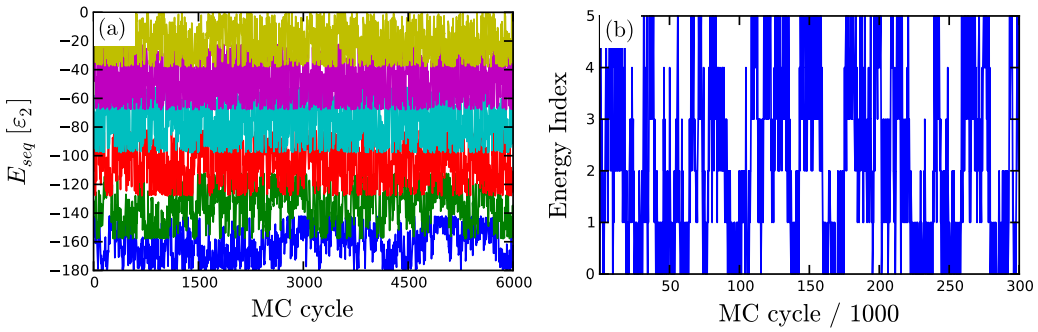

Figure 6.2: (a) A portion of the trajectory from the sequence MC simulations showing flat sequence energy distributions for each of the systems simulated. (b) The trajectory of a single replica system from (a) showing a random-walk in energy space.

reduce the penalty of having multiple HS monomers. As expected, at higher solvent temperatures, both the aggregated and dispersed states show a higher DOS than their low temperature counterparts. This is presumably due to a diminished preference to maintain favorable solvophilic interactions at higher temperatures, and thus greater HS fractions are more common. The difference between the aggregated and dispersed DOS's at the high temperature is too slight to draw the conclusion that the low temperature ordering has been reversed, but the higher sequence entropy for aggregated over dispersed states, evident at lower temperature, is at least, largely eliminated. It is expected that as the temperature grows large, the free energy benefit of solvophobic aggregation tends to zero.

If Fig. 6.4 we plot the conditional probability of observing a sequence energy of E given that the solute has a HS number fraction of $x = \sum_{k=1}^{N} \delta_{1k}/N$, where $N = 20$ is the total number of monomers in both solutes and δ_{1k} is one

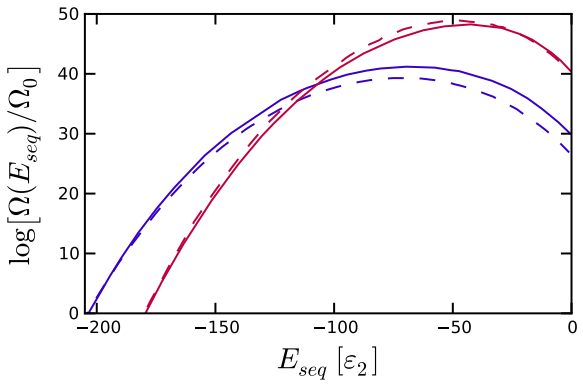

Figure 6.3: Scaled sequence entropy for the aggregated (solid lines) and dispersed (dashed lines) states of the rods at solvent temperatures of $T = 0.6$ (blue) and $T = 1.2$ (red). The entropy is scaled by its minimum value (corresponding to a DOS of Ω_0) in each curve.

if monomer k is a HS and zero otherwise. In general, these distributions shift to higher energies as the number fraction of HS's grows, as expected. Comparing the dispersed and aggregated states reveals that dispersion to infinite dilution broadens the conditional probability distributions. This is due to the fact that there are more solvent molecules interacting with the solutes in the dispersed states, and therefore there are many more possible arrangements of solute-solvent interactions leading to a broader range of possible energies for a given sequence. There are negligible differences between the high and low temperature distributions for this measure.

The average fraction of HS monomers for a given sequence energy is plotted in Fig. 6.5 (a). At low sequence energies, the low temperature state has a higher average fraction of HS monomers than the high temperature state for both aggregated and dispersed configurations. As the sequence energy

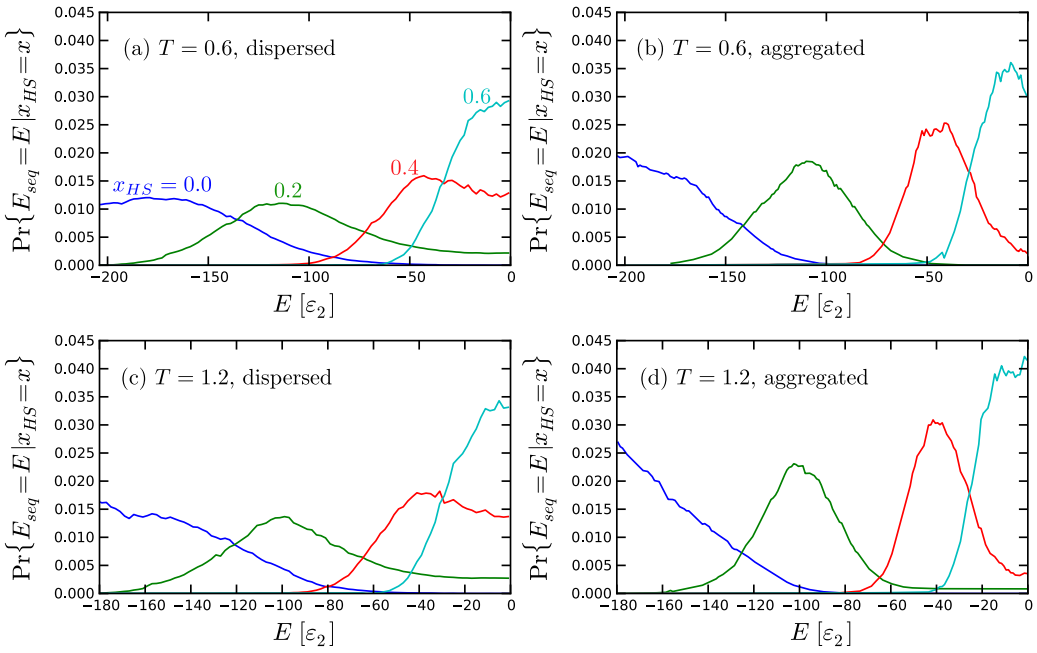

Figure 6.4: The conditional probability of observing a sequence energy E given a hard-sphere fraction x for each solvent temperature and solute state considered.

increases, this behavior crosses over, and the high temperature state has a greater number fraction of HS monomers. At both high and low temperatures, the dispersed states have a nearly equivalent fraction of HS monomers than the aggregated configuration, but as the sequence energy increases, the aggregated state contains a higher average HS fraction. In Fig. 6.5 (b) the average HS fraction is plotted versus the sequence energy for only the monomers on the ends of the solutes. There is little difference between the high and low temperature states, and for high sequence energies, we have determined that there is a slightly lower HS fraction for the end monomers than for the average

over the entire molecule in (a). This suggests that there is a slight preference for HS monomers to be in the interior of the chain, which as we shall see, is not a result of solvophobic aggregation but rather a preference to keep strongly interacting Jagla particles together.

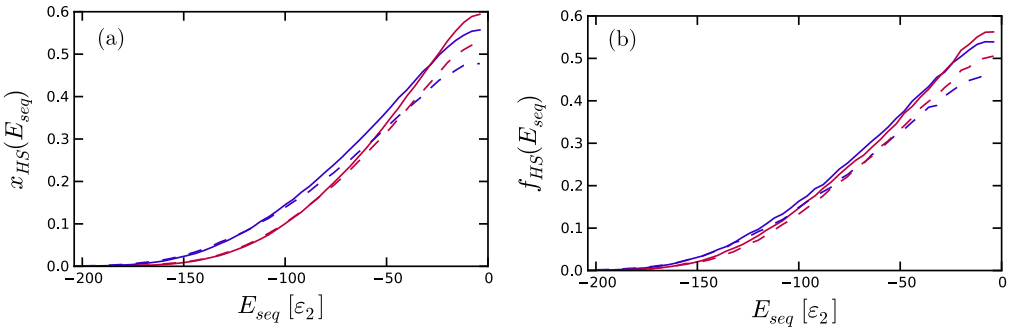

Figure 6.5: (a) The average hard sphere fraction observed as a function of the sequence energy for aggregated (solid lines) and dispersed (dashed lines) rods at solvent temperatures of $T = 0.6$ (blue lines) and $T = 1.2$ (red lines). (b) The same for only the monomers on the ends of the polymers.

To gain a clearer picture of the tendency for HS monomers to appear in neighboring sequence positions, we have analyzed the simulation data and obtained the probability to find at least one instance of the repeat pattern HS-HS or Jagla-Jagla in the sequence of one rod. The results are plotted in Fig. 6.6. As shown in Fig. 6.6 (a), at low sequence energies, there is a greater preference relative to the uniform distribution for neighboring HS monomers in the aggregated rods at both temperatures. This trend reverses at sequence energies of around -60 [ε_2]; for higher energies, it is less likely to find a HS-HS pattern in the sequence than would be predicted by a uniformly distributed sequence (dotted lines). Similar behavior is seen in the distributions for the

dispersed rods in Fig. 6.6 (b), with the difference from the uniform distribution more slight at lower energies and more pronounced at higher energies. In (c) and (d) we see that the Jagla-Jagla pattern is less likely than would be expected for a uniform distribution in all cases. At least in the case of the aggregated configuration, the reasons for these trends become apparent when considering the geometry of solutes and the data for cross-chain pairing in Fig. 6.7.

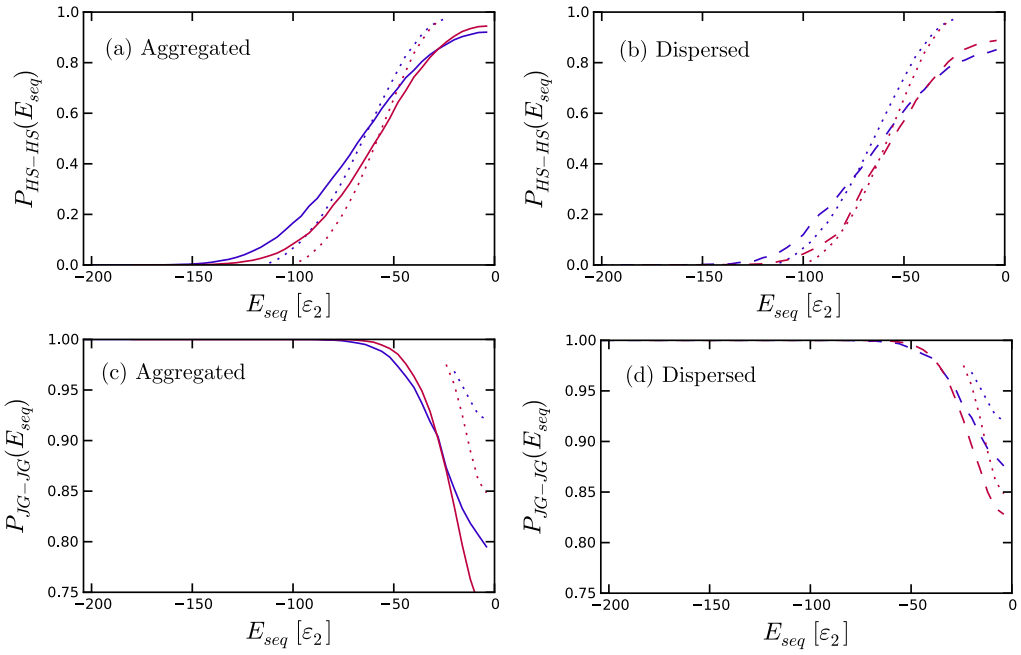

Figure 6.6: The probability of observing [(a) and (b)] HS-HS and [(c) and (d)] Jagla-Jagla at least one time in the sequence as a function of sequence energy at two solvent temperatures, $T = 0.6$ (blue lines) and $T = 1.2$ (red lines). The solid lines in (a) and (c) represent the results of the aggregated rods simulation data, and the dashed lines in (b) and (d) are the dispersed configuration. The dotted lines in both figures are what would be expected from a uniform distribution.

In Fig. 6.7 we have plotted the probability of observing aligned pairs

of monomers in the aggregated rod configuration as a function of the sequence energy. In Fig. 6.7 (a) we show that there is a strong preference for aligning HS monomers relative to a uniform distribution. The lower temperature has a greater preference relative to the uniform distribution for alignment than the higher temperature which diminishes as sequence energy increases. Similarly, in Fig. 6.7 (b) we show the probability of observed aligned Jagla pairs as a function of the sequence energy. The plot reveals the very strong preference to maintain favorable attractive interactions between the solute and solvent, even at high sequence energies. There is a strong preference to pair Jagla particles with one another, which is not surprising given that the pair separation is exactly the minimum in the potential well. The preference for Jagla particles to match cross-sequence pairs is likely the driving force for HS particles to be paired since not pairing HS monomers necessitates the loss of *two* Jagla-Jagla interactions. The increasing preference, relative to the uniform distribution, of matching monomer pairs across the rods explains the reduced tendency to find neighbors seen in Fig. 6.6. The energetic benefit of pairing Jagla particles across from one another in the aggregated configuration outweighs any benefit of pairing sequence neighbors.

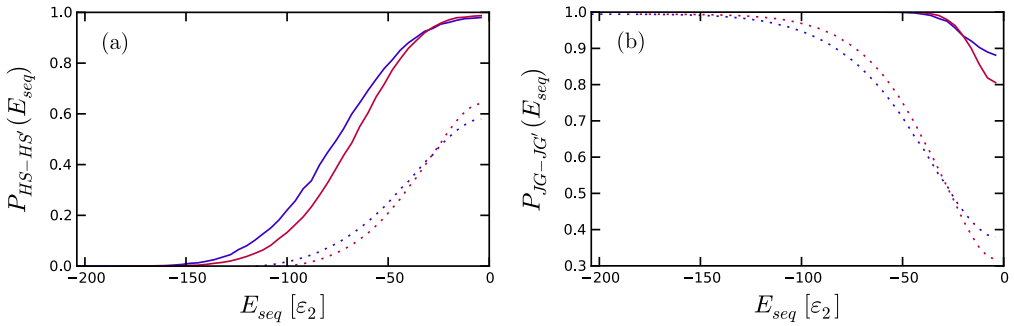

Figure 6.7: The probability of observing at least one cross-chain aligned pair of (a) hard sphere or (b) Jagla monomers in the two aggregated rods as a function of the sequence energy at two solvent temperatures, $T = 0.6$ (blue lines) and $T = 1.2$ (red lines). The solid lines represent the results of the aggregated rods simulation data, while dotted lines are what would be expected from a uniform distribution.

These results are perhaps qualitatively unsurprising when considering the geometry of the configurations chosen. In particular, the alignment of aggregated rods at a separation equivalent to the minimum in the Jagla well-depth, r_1, explains the strong preference to pair Jagla particles across the chain. The choice of monomer alphabet and solute configuration entirely determine the general behavior observed. Nevertheless, the quantitative responses, particularly for the HS distributions manifest non-trivial solvent and temperature effects.

6.4 Conclusions

We have demonstrated the effects of solvent temperature on the sequence landscape of simple rod solutes in the Jagla solvent. An enhanced sampling MC method was used to perform random walks in the sequence energy, which is the solute self-interaction energy plus the solute-solvent interaction energy. The DOS in sequence energy is shown to be sensitive to the solvent temperature, with the maximum in the DOS shifting to higher sequence energies as the solvent temperature is increased. Higher sequence energies are associated with greater number fractions of HS monomers, and the location of HS monomers in the sequence is strongly dependent upon the solute configuration. In particular, it is demonstrated that in an aggregated state, in which the two rods are aligned monomer by monomer and separated by a distance r_1, a strong preference to pair Jagla monomers across the rods exists. This preference diminishes with increasing solvent temperature.

Although rudimentary, the results clearly show that in general the sequence landscape is solvent and state-dependent.

Chapter 7

Conclusions

In this work we have systematically investigated the temperature, pressure and length scale dependence of simple solvophobic solutes in three liquids: the Lennard-Jones (LJ) liquid, the Jagla liquid, and water. We have found that, despite its simplicity, the Jagla liquid reproduces many of the qualitative behaviors of hydrophobic hydration including non-monotonic solubility, negative entropy of transfer, and entropy convergence. Furthermore, we have observed the length scale crossover (the change in scaling of solvation free energy with solute size from solute volume to solute surface area), for the Jagla liquid and noted its similarity to the crossover in water. The Jagla liquid, like water, demonstrates a greater propensity to maintain its liquid structure around large solvophobic solutes than typical simple liquids. Similarly, both the Jagla liquid and water dewet extended surfaces less readily than typical liquids. It is inferred that the presence of two competing energy scales (the potential minimum / ramp height energies in the Jagla liquid, and the hydrogen-bonded / not hydrogen bonded energies in water), coupled to two different length scales in such a way that the energetically favorable interaction increases void space as temperature is lowered, is an essential feature of liquids with water-like solvation behavior. It is hypothesized that the analogy

between the temperature dependence of the enthalpy and entropy in water and the Jagla liquid involves the two energy scales. In particular, it is suggested that Jagla particles within the solvation shell are less crowded and more likely to be at separations close to the minimum in the potential well, and that as temperature is increased the relative number of these favorable interactions to the same in equivalent bulk liquid volumes decreases. This is in analogy to predictions of the temperature dependence of hydrogen bonding in solvation shell water. Future work includes a detailed investigation of solvent orientational order within the solvation shell of small and large solvophobes to more clearly identify the origins of water-like enthalpic and entropic behaviors.

A simple thought experiment on aggregate formation has elucidated the implications of the differences in crossover behavior for cold and pressure-induced dissociation phenomena. Water-like crossover behavior exposes a size range of aggregates to destabilization upon cooling or pressurizing, which may be the driving force for the cold and pressure denaturation of globular proteins. Although this feature is seen both in water-like and simple liquids, the width of the region is substantially broader in the water-like liquids, explaining why the observation of these phenomena is unique to water. It is argued that smaller size of constituent solvophobes as well as the the presence of weak attractive interactions increases the width of the cold-dissociation regions, meaning cold-induced dissociation may occur for a broader range of aggregate sizes. It is suggested that cold-induced dissociation may occur in simple liquids as well for sufficiently small constituent solute particles and

sufficiently strong solute-solvent attractions. This suggests possible investigation of cooling-induced dissociation in simple liquids such as the LJ liquid and square-well liquids, which are known to accurately model simple hydrocarbons and colloidal systems, respectively.

It has been demonstrated that the Gaussian behavior of density fluctuations in molecular-sized volumes in water is not a general feature of liquids, but rather, may be peculiar to water and other networked liquids with electrostatic interactions. It is suggested that investigating density fluctuations in a simple liquid with tetrahedral network structure, "Molinero water" [66], may shed light on upon this issue.

The effects of explicit solvent on the sequence energy landscape of simple rigid heteropolymers was investigated. It was shown that the negation of solvent and temperature effects may have a profound effect on the designability of sequences. Future work includes identifying particular sequences of biological or synthetic relevance and exploring the configurational space for a variety of solvent conditions. There is opportunity for theoretical work on the establishment of correlations between the sequence and configurational energy landscapes.

Appendices

Appendix A

Details of the Monte Carlo Simulations Along the Saturation Curves of the LJ liquid, SPC/E water, and the Jagla Liquid

Included below are tables detailing the Monte Carlo simulations and fitting results used to characterize properties of the Jagla liquid along the saturation curve.

N	T $[\varepsilon_2/k_B]$	ρ_l $[r_0^{-3}]$	ρ_v $[r_0^{-3}]$	P_{sat} $[\varepsilon_2/r_0^3]$	γ_{lv} $[\varepsilon_2/r_0^2]$
1374	0.4	0.256(2)	$5(3)\times10^{-5}$	$3(2)\times10^{-5}$	0.491(8)
1374	0.6	0.255(2)	$2.3(7)\times10^{-4}$	$1.4(4)\times10^{-4}$	0.407(7)
1386	0.8	0.244(2)	0.0018(2)	0.0014(2)	0.314(8)
1444	1.0	0.226(3)	0.0067(6)	0.0056(6)	0.213(5)
1600	1.2	0.203(2)	0.0174(9)	0.015(1)	0.115(7)

Table A.1: Canonical ensemble MC simulations of a liquid slab in equilibrium with its vapor were performed to obtain estimates of saturation properties. N Jagla particles were simulated at five different temperatures for 1.6×10^6 MC cycles, where one cycle corresponds to N MC moves. The liquid and vapor densities were estimated from ensemble averages of the densities in the centers of the liquid and vapor regions, respectively. Similarly, the saturation pressure was obtained by evaluating the pressure tensor in the center of the vapor region. The liquid-vapor surface tension is calculated using the virial relation [55, 92]. Numbers in parentheses are estimates of the statistical error in the last digit of the reported value.

T $[\varepsilon_2/k_B]$	P $[\varepsilon_2/r_0^3]$
0.4	3.2×10^{-5}
0.5	5.4×10^{-5}
0.6	1.4×10^{-4}
0.7	5.0×10^{-4}
0.8	1.4×10^{-3}
0.9	3.0×10^{-3}
1.0	5.6×10^{-3}
1.1	9.5×10^{-3}
1.2	1.5×10^{-2}

Table A.2: Pure Jagla liquid NPT MC simulations were performed for several states along the liquid-vapor coexistence curve. Simulations were performed for both liquid and vapor densities estimated from the data in Table A.1. Each simulation consisted of 1000 Jagla particles which were simulated for 6×10^5 cycles after being equilibrated for at least 2×10^5 cycles. Each cycle consists of N MC moves. In each MC move, there is a $1/N$ chance of attempting a volume move and $(N-1)/N$ chance of attempting to move a randomly selected particle. Coordinates were output to trajectories every 5 cycles. Test particle insertion was performed for cavity sizes ranging from 0.5 to 1.65 Jagla diameters on each frame in the liquid trajectories to obtain the small solute data used in the revised scaled particle theory fit of Eq. (3.5). Test particle insertions were performed on vapor trajectories for all cavity radii listed in Table A.3 to obtain non-ideal gas solubilities and vapor-wall surface tensions.

R $[r_0]$	N	N_{cyc}
0.5	1000	1.76×10^6
0.7	1000	1.76×10^6
0.9	1000	1.76×10^6
1.1	1000	1.76×10^6
1.3	1000	1.76×10^6
1.5	1000	1.76×10^6
1.7	1000	1.76×10^6
1.9	1000	1.76×10^6
2.1	1000	1.76×10^6
2.3	1000	1.76×10^6
2.5	1000	1.76×10^6
2.7	1000	1.76×10^6
2.9	1000	1.76×10^6
3.1	1000	1.76×10^6
3.3	1000	1.76×10^6
3.5	1000	1.76×10^6
3.7	1000	1.76×10^6
3.9	1000	1.76×10^6
4.1	2000^*	9.6×10^5
4.3	2000	9.6×10^5
4.5	2000^*	9.6×10^5
4.7	2000	9.6×10^5
4.9	2000	9.6×10^5

Table A.3: List of NPT MC simulations carried out with N Jagla particles and a single cavity of radius R. For each cavity size, nine simulations were performed—one for each of the thermodynamic states listed in Table A.2. Jagla-cavity contact densities were averaged over N_{cyc} cycles. A superscript $*$ indicates that additional simulations of $N = 3000$ and $N = 4000$ Jagla particles were performed to test dependence of the results on system size. No significant changes were observed.

T $[\varepsilon_2/k_B]$	γ_∞ $[\varepsilon_2/r_0^2]$	δ $[r_0]$	κ $[r_0^3]$	λ $[r_0^4]$
0.4	0.550	-0.010	-8.183	-13.048
0.5	0.514	-0.093	-6.594	-11.444
0.6	0.474	-0.176	-5.530	-10.198
0.7	0.428	-0.271	-4.801	-9.309
0.8	0.381	-0.354	-3.964	-8.128
0.9	0.332	-0.453	-3.376	-7.242
1.0	0.278	-0.592	-2.900	-6.537
1.1	0.222	-0.774	-2.481	-5.832
1.2	0.173	-0.931	-1.901	-4.805

Table A.4: Parameters from the least-squares fit of Eq. (3.6) to the contact densities obtained from the simulations in Table A.3.

i	A_i	B_i	C_i
0	-0.3233	0.6027	0.2090
1	1.9374	-1.2166	1.2624
2	-1.7246	0.0657	-1.7214
3	0.2920	0.4900	0.3738

Table A.5: Cavity equation of state parameters for the Jagla fluid. Parameters were obtained from a least squares fit of Eq. (3.12) to the excess chemical potential solvation data in Fig. 5.2. Units use r_0 for the length scale and ε_2 for the energy scale.

T $[\varepsilon_{LJ}/k_B]$	P $[\varepsilon_{LJ}/\sigma_{LJ}^3]$
0.65	0.0034
0.70	0.0068
0.75	0.0096
0.80	0.0150
0.85	0.0226
0.90	0.0327
0.95	0.0458
1.00	0.0620

Table A.6: Selected states along the liquid-vapor coexistence curve of the LJ liquid [1].

T [K]	ρ [g/cm^3]
273.0	1.000
300.0	0.998
373.0	0.949
423.0	0.902
473.0	0.841
570.0	0.674
610.0	0.545
620.0	0.507
630.0	0.470
640.0	0.426
652.0	0.326
640.0	0.217
630.0	0.162
620.0	0.112
610.0	0.082
570.0	0.036

Table A.7: Selected states along the liquid-vapor coexistence curve of SPC/E water [42].

T [K]	273	304	335	366	398	429	460	491	522

Table A.8: Temperatures along the saturation curve of water used in the cavity equation of state calculations. These are the same reduced temperatures (T/T_{crit}, where T_{crit} is the liquid-vapor critical point) as the temperatures used for the Jagla liquid.

i	A_i	B_i	C_i
0	12.429	40.3713	12.3712
1	51.3577	-91.3713	19.0438
2	-18.7888	28.2881	-7.68791
3	1.74344	-2.46828	0.735148

Table A.9: Cavity equation of state parameters for water [6]. Units use nm for the length scale and kJ/mol for the energy scale.

Appendix B

Details of the High Pressure Monte Carlo Simulations Along the $T = 0.6$ Isotherm of the Jagla Liquid

Included below are tables detailing the Monte Carlo simulations and fitting results used to characterize properties of the Jagla liquid along the $T = 0.6$ isotherm of the Jagla liquid.

$P\ [\varepsilon_2/r_0^3]$	$\rho\ [r_0^{-3}]$
0.05	0.2677(1)
0.10	0.2825(3)
0.15	0.2986(4)
0.20	0.3166(5)
0.25	0.3352(3)
0.30	0.3545(9)

Table B.1: The state points simulated for the Jagla liquid along the $T = 0.6$ isotherm. Isothermal-isobaric MC simulations of a system of $N = 1000$ Jagla particles were performed at each of the pressures listed for 7×10^5 MC cycles. Each cycle consists of N MC moves. In each MC move, there is a $1/N$ chance of attempting a volume move and $(N-1)/N$ chance of attempting to move a randomly selected particle. The first 1×10^5 cycles were treated as equilibration and statistics were obtained from the last 6×10^5 cycles. Frames were output every 5 cycles. Insertion probabilities for cavity volumes ranging from 0.5 to 2.0 times the size of the Jagla particle were obtained by attempting 2×10^4 random insertions per frame.

R $[r_0]$	N
0.500	1000
0.600	1000
0.721	1000
0.866	1000
1.040	1000
1.249	1000
1.500	1000
1.802	1000
2.164	1000
2.599	1000
3.122	2000
3.749	2000
4.503	3000
5.408	4000
6.495	5000
7.800	6000

Table B.2: List of cavity sizes and number of Jagla particles in each of the systems simulated for the high-pressure pressure cavity solvation study in Chapter 5. NPT MC simulations were carried out for each system at all all of the state points in Table B.1. All systems were equilibrated for 2×10^5 MC cycles and then run for 10^6 MC cycles for collection of statistics.

P $[\varepsilon_2/r_0^3]$	γ_∞ $[\varepsilon_2/r_0^2]$	δ $[r_0]$	κ $[r_0^3]$	λ $[r_0^4]$
0.05	0.561	0.062	-1.047	-3.542
0.10	0.631	0.150	0.348	-1.179
0.15	0.693	0.235	2.551	2.020
0.20	0.779	0.311	4.131	4.679
0.25	0.839	0.329	4.687	5.466
0.30	0.918	0.357	5.608	6.790

Table B.3: Results of the least-squares fit of Eq. (3.6) to the cavity contact values measured by the MC simulations in Table B.2.

Bibliography

[1] H.S. Ashbaugh. Blowing bubbles in Lennard-Jonesium along the saturation curve. *The Journal of chemical physics*, 130:204517, 2009.

[2] H.S. Ashbaugh and L.R. Pratt. Colloquium: Scaled particle theory and the length scales of hydrophobicity. *Reviews of Modern Physics*, 78(1):159–178, 2006.

[3] H.S. Ashbaugh and L.R. Pratt. Contrasting nonaqueous against aqueous solvation on the basis of scaled-particle theory. *J. Phys. Chem. B*, 111(31):9330–9336, 2007.

[4] M.V. Athawale, G. Goel, T. Ghosh, T.M. Truskett, and S. Garde. Effects of lengthscales and attractions on the collapse of hydrophobic polymers in water. *Proceedings of the National Academy of Sciences*, 104(3):733, 2007.

[5] P. Ball. Water as an active constituent in cell biology. *Chem. Rev*, 108(1):74–108, 2008.

[6] D. Ben-Amotz. Global thermodynamics of hydrophobic cavitation, dewetting, and hydration. *The Journal of chemical physics*, 123:184504, 2005.

[7] D. Ben-Amotz, F.O. Raineri, and G. Stell. Solvation thermodynamics: Theory and applications. *The Journal of Physical Chemistry B*, 109(14):6866–6878, 2005.

[8] D. Ben-Amotz and B. Widom. Generalized Solvation Heat Capacities. *J. Phys. Chem. B*, 110(40):19839–19849, 2006.

[9] D. Ben-Amotz and B. Widom. Nonideal gas solvation thermodynamics. *The Journal of chemical physics*, 126:104502, 2007.

[10] A. Ben-Naim. *Molecular theory of solutions*. Oxford University Press, USA, 2006.

[11] HJC Berendsen, JR Grigera, and TP Straatsma. The missing term in effective pair potentials. *Journal of Physical Chemistry*, 91(24):6269–6271, 1987.

[12] HJC Berendsen, D. van der Spoel, and R. Van Drunen. Gromacs: A message-passing parallel molecular dynamics implementation. *Computer Physics Communications*, 91(1-3):43–56, 1995.

[13] Bruce J. Berne, John D. Weeks, and Ruhong Zhou. Dewetting and Hydrophobic Interaction in Physical and Biological Systems. *ANNUAL REVIEW OF PHYSICAL CHEMISTRY*, 60:85–103, 2009.

[14] K. Binder. Monte carlo calculation of the surface tension for two- and three-dimensional lattice-gas models. *Phys. Rev. A*, 25(3):1699–1709, Mar 1982.

[15] W. Blokzijl and J.B.F.N. Engberts. Hydrophobic effects. Opinions and facts. *Angewandte Chemie International Edition in English*, 32(11):1545–1579, 1993.

[16] S.V. Buldyrev, P. Kumar, P.G. Debenedetti, P.J. Rossky, and H.E. Stanley. Water-like solvation thermodynamics in a spherically symmetric solvent model with two characteristic lengths. *Proceedings of the National Academy of Sciences*, 104(51):20177, 2007.

[17] G. Bussi, D. Donadio, and M. Parrinello. Canonical sampling through velocity rescaling. *The Journal of chemical physics*, 126:014101, 2007.

[18] D. Chandler. Interfaces and the driving force of hydrophobic assembly. *Nature*, 437(7059):640–647, 2005.

[19] David Chandler. Gaussian field model of fluids with an application to polymeric fluids. *Phys. Rev. E*, 48(4):2898–2905, Oct 1993.

[20] C. Chipot and A. Pohorille. *Free energy calculations: theory and applications in chemistry and biology*, volume 86. Springer Verlag, 2007.

[21] N. Choudhury and B.M. Pettitt. On the mechanism of hydrophobic association of nanoscopic solutes. *Journal of the American Chemical Society*, 127(10):3556–3567, 2005.

[22] Niharendu Choudhury and B. Montgomery Pettitt. The dewetting transition and the hydrophobic effect. *Journal of the American Chemical Society*, 129(15):4847–4852, 2007.

[23] E. De Miguel and G. Jackson. Detailed examination of the calculation of the pressure in simulations of systems with discontinuous interactions from the mechanical and thermodynamic perspectives. *Molecular physics(Print)*, 104(22-24):3717–3734, 2006.

[24] C.L. Dias, T. Ala-Nissila, J. Wong-ekkabut, I. Vattulainen, M. Grant, and M. Karttunen. The hydrophobic effect and its role in cold denaturation. *Cryobiology*, 60(1):91–99, 2010.

[25] Cristiano L. Dias, Tapio Ala-Nissila, Jirasak Wong-ekkabut, Ilpo Vattulainen, Martin Grant, and Mikko Karttunen. "Reply to the comment by Graziano on "The hydrophobic effect and its role in cold denaturation"". *Cryobiology*, 60(3):356 – 357, 2010.

[26] U. Essmann, L. Perera, M.L. Berkowitz, T. Darden, H. Lee, and L.G. Pedersen. A smooth particle mesh ewald method. *Journal of Chemical Physics*, 103(19):8577–8593, 1995.

[27] M. Fitzgerald, RR Picard, and RN Silver. Monte carlo transition dynamics and variance reduction. *Journal of Statistical Physics*, 98(1):321–345, 2000.

[28] H. Flyvbjerg and HG Peterson. Error estimates on averages of correlated data. *The Journal of chemical physics*, 91(1):461–466, 1989.

[29] H.S. Frank and M.W. Evans. Free volume and entropy in condensed systems III. Entropy in binary liquid mixtures; partial molal entropy in

dilute solutions; structure and thermodynamics in aqueous electrolytes. *The Journal of Chemical Physics*, 13:507, 1945.

[30] D. Frenkel and B. Smit. *Understanding molecular simulation: from algorithms to applications*. Academic Pr, 2002.

[31] A.B. Fulton and W.B. Isaacs. Titin, a huge, elastic sarcomeric protein with a probable role in morphogenesis. *Bioessays*, 13(4):157–161, 1991.

[32] S. Garde and H.S. Ashbaugh. Temperature dependence of hydrophobic hydration and entropy convergence in an isotropic model of water. *The Journal of Chemical Physics*, 115:977, 2001.

[33] S. Garde, A.E. García, L.R. Pratt, and G. Hummer. Temperature dependence of the solubility of non-polar gases in water. *Biophysical chemistry*, 78(1-2):21–32, 1999.

[34] S. Garde, G. Hummer, A.E. Garcia, M.E. Paulaitis, and L.R. Pratt. Origin of entropy convergence in hydrophobic hydration and protein folding. *Physical review letters*, 77(24):4966–4968, 1996.

[35] N. Giovambattista, P.G. Debenedetti, and P.J. Rossky. Effect of surface polarity on water contact angle and interfacial hydration structure. *The Journal of Physical Chemistry B*, 111(32):9581–9587, 2007.

[36] N. Giovambattista, C.F. Lopez, P.J. Rossky, and P.G. Debenedetti. Hydrophobicity of protein surfaces: Separating geometry from chemistry. *Proceedings of the National Academy of Sciences*, 105(7):2274, 2008.

[37] N. Giovambattista, P.J. Rossky, and P.G. Debenedetti. Effect of pressure on the phase behavior and structure of water confined between nanoscale hydrophobic and hydrophilic plates. *Physical Review E*, 73(4):041604, 2006.

[38] G. Graziano and B. Lee. On the intactness of hydrogen bonds around nonpolar solutes dissolved in water. *J. Phys. Chem. B*, 109(16):8103–8107, 2005.

[39] Giuseppe Graziano. Water: cavity size distribution and hydrogen bonds. *Chemical Physics Letters*, 396(4-6):226 – 231, 2004.

[40] Giuseppe Graziano. "Comment on "The hydrophobic effect and its role in cold denaturation" Cryobiology 60 (2010) 91-99". *Cryobiology*, 60(3):354 – 355, 2010.

[41] B. Guillot and Y. Guissani. A computer simulation study of the temperature dependence of the hydrophobic hydration. *The Journal of Chemical Physics*, 99:8075, 1993.

[42] Y. Guissani and B. Guillot. A computer simulation study of the liquid-vapor coexistence curve of water. *The Journal of chemical physics*, 98(10):8221, 1993.

[43] T. Head-Gordon, J.R. Dowdle, P.G. Debenedetti, P.J. Rossky, and Lynden-Bell R.M. In preparation. 2011.

[44] D.M. Huang and D. Chandler. Cavity formation and the drying transition in the Lennard-Jones fluid. *Physical Review E*, 61(2):1501–1506, 2000.

[45] D.M. Huang and D. Chandler. The Hydrophobic Effect and the Influence of Solute- Solvent Attractions. *J. Phys. Chem. B*, 106(8):2047–2053, 2002.

[46] D.M. Huang, P.L. Geissler, and D. Chandler. Scaling of Hydrophobic Solvation Free Energies. *J. Phys. Chem. B*, 105(28):6704–6709, 2001.

[47] G. Hummer, S. Garde, A.E. García, M.E. Paulaitis, and L.R. Pratt. The pressure dependence of hydrophobic interactions is consistent with the observed pressure denaturation of proteins. *Proceedings of the National Academy of Sciences*, 95(4):1552, 1998.

[48] G. Hummer, S. Garde, A.E. Garcia, A. Pohorille, and L.R. Pratt. An information theory model of hydrophobic interactions. *Proceedings of the National Academy of Sciences*, 93(17):8951–8955, 1996.

[49] G. Hummer, S. Garde, AE Garcıa, and LR Pratt. New perspectives on hydrophobic effects. *Chemical Physics*, 258(2-3):349–370, 2000.

[50] G. Hummer, S. Garde, A. E. Garca, M. E. Paulaitis, and L. R. Pratt. Hydrophobic effects on a molecular scale. *The Journal of Physical Chemistry B*, 102(51):10469–10482, 1998.

[51] W. Humphrey, A. Dalke, and K. Schulten. Vmd: visual molecular dynamics. *Journal of molecular graphics*, 14(1):33–38, 1996.

[52] EA Jagla. Phase behavior of a system of particles with core collapse. *Physical Review E*, 58(2):1478–1486, 1998.

[53] EA Jagla. Core-softened potentials and the anomalous properties of water. *The Journal of Chemical Physics*, 111:8980, 1999.

[54] W. Kauzmann. Some factors in the interpretation of protein denaturation. *Adv. Protein Chem*, 14(1):63, 1959.

[55] J.G. Kirkwood and F.P. Buff. The statistical mechanical theory of surface tension. *The Journal of Chemical Physics*, 17:338, 1949.

[56] D.A. Kofke and P.T. Cummings. Quantitative comparison and optimization of methods for evaluating the chemical potential by molecular simulation. *Molecular Physics*, 92(6):973–996, 1997.

[57] S.K. Kumar, I. Szleifer, K. Sharp, P.J. Rossky, R. Friedman, and B. Honig. Size dependence of transfer free energies. 1. a flory-huggins approach. *The Journal of Physical Chemistry*, 99(20):8382–8391, 1995.

[58] K.F. Lau and K.A. Dill. A lattice statistical mechanics model of the conformational and sequence spaces of proteins. *Macromolecules*, 22(10):3986–3997, 1989.

[59] C.Y. Lee, J.A. McCammon, and PJ Rossky. The structure of liquid water at an extended hydrophobic surface. *The Journal of Chemical Physics*, 80:4448, 1984.

[60] E. Lomba, NG Almarza, C. Martín, and C. McBride. Phase behavior of attractive and repulsive ramp fluids: Integral equation and computer simulation studies. *The Journal of chemical physics*, 126:244510, 2007.

[61] K. Lum, D. Chandler, and J.D. Weeks. Hydrophobicity at small and large length scales. *J. Phys. Chem. B*, 103(22):4570–4577, 1999.

[62] R. M. Lynden-Bell, N. Giovambattista, P. G. Debenedetti, T. Head-Gordon, and P. J. Rossky. Hydrogen bond strength and network structure effects on hydration of non-polar molecules. *Phys. Chem. Chem. Phys.*, 13:2748–2757, 2011.

[63] R. M. Lynden-Bell, J.R. Dowdle, N. Giovambattista, P. G. Debenedetti, T. Head-Gordon, and P. J. Rossky. Non-gaussian occupancy statistics for molecular volumes in liquids. *In preparation*, 2011.

[64] S. Matysiak, P. Debenedetti, and P.J. Rossky. Dissecting the Energetics of Hydrophobic Hydration of Polypeptides. *In preparation*, 2011.

[65] S. Miyamoto and P.A. Kollman. Settle: an analytical version of the shake and rattle algorithm for rigid water models. *Journal of computational chemistry*, 13(8):952–962, 1992.

[66] V. Molinero and E.B. Moore. Water modeled as an intermediate element between carbon and silicon. *The Journal of Physical Chemistry B*, 113(13):4008–4016, 2008.

[67] N. Muller. Search for a realistic view of hydrophobic effects. *Accounts of Chemical Research*, 23(1):23–28, 1990.

[68] P. Orea, Y. Duda, and J. Alejandre. Surface tension of a square well fluid. *The Journal of Chemical Physics*, 118:5635, 2003.

[69] A.J. Patel, P. Varilly, and D. Chandler. Fluctuations of water near extended hydrophobic and hydrophilic surfaces. *The Journal of Physical Chemistry B*, 114(4):1632–1637, 2010.

[70] Lawrence R. Pratt. Molecular theory of hydrophobic effects: she is too mean to have her name repeated.*. *Annual Review of Physical Chemistry*, 53(1):409–436, 2002.

[71] L.R. Pratt and D. Chandler. Theory of the hydrophobic effect. *The Journal of Chemical Physics*, 67:3683, 1977.

[72] P.L. Privalov. Cold denaturation of protein. *Critical reviews in biochemistry and molecular biology*, 25(4):281–306, 1990.

[73] S. Rajamani, T.M. Truskett, and S. Garde. Hydrophobic hydration from small to large lengthscales: Understanding and manipulating the crossover. *Proceedings of the National Academy of Sciences of the United States of America*, 102(27):9475, 2005.

[74] L.E. Reichl. *A modern course in statistical physics*. Vch Pub, 2009.

[75] H. Reiss, HL Frisch, and JL Lebowitz. Statistical mechanics of rigid spheres. *The Journal of Chemical Physics*, 31:369, 1959.

[76] Peter J. Rossky. Exploring nanoscale hydrophobic hydration. *Faraday Discuss.*, 146:13–18, 2010.

[77] David E. Shaw, Paul Maragakis, Kresten Lindorff-Larsen, Stefano Piana, Ron O. Dror, Michael P. Eastwood, Joseph A. Bank, John M. Jumper, John K. Salmon, Yibing Shan, and Willy Wriggers. Atomic-level characterization of the structural dynamics of proteins. *Science*, 330(6002):341–346, 2010.

[78] M. Scott Shell, Pablo G. Debenedetti, and Athanassios Z. Panagiotopoulos. Computational characterization of the sequence landscape in simple protein alphabets. *Proteins: Structure, Function, and Bioinformatics*, 62(1):232–243, 2006.

[79] M.S. Shell, P.G. Debenedetti, and A.Z. Panagiotopoulos. An improved monte carlo method for direct calculation of the density of states. *The Journal of chemical physics*, 119:9406, 2003.

[80] S. Shimizu and H.S. Chan. Temperature dependence of hydrophobic interactions: A mean force perspective, effects of water density, and nonadditivity of thermodynamic signatures. *The Journal of Chemical Physics*, 113:4683, 2000.

[81] L. Smeller. Pressure-temperature phase diagrams of biomolecules. *Biochimica et Biophysica Acta (BBA)-Protein Structure and Molecular Enzymology*, 1595(1-2):11–29, 2002.

[82] B. Smit. Phase diagrams of lennard-jones fluids. *Journal of chemical physics*, 96(11):8639–8640, 1992.

[83] F.H. Stillinger. Structure in aqueous solutions of nonpolar solutes from the standpoint of scaled-particle theory. *Journal of Solution Chemistry*, 2(2):141–158, 1973.

[84] F.H. Stillinger and M.A. Cotter. Free Energy in the Presence of Constraint Surfaces. *The Journal of Chemical Physics*, 55:3449, 1971.

[85] M.T. Stone, P.J. in 't Veld, Y. Lu, and I.C. Sanchez. Hydrophobic/hydrophilic solvation: inferences from Monte Carlo simulations and experiments. *Molecular physics*, 100(17):2773–2792, 2002.

[86] M.T. Stone, T.M. Truskett, I.C. Sanchez, et al. Liquid Structure via Cavity Size Distributions. *J. Phys. Chem. B*, 104(50):12028–12034, 2000.

[87] C. Tanford. How protein chemists learned about the hydrophobic factor. *Protein science*, 6(6):1358–1366, 1997.

[88] C. Tanford, H. Gunther, WK Paik, and S. Kim. *The hydrophobic effect: Formation of micelles and biological membranes 2nd ed.* John Wiley & Sons, New York, 1980.

[89] DM Tully-Smith and H. Reiss. Further development of scaled particle theory of rigid sphere fluids. *The Journal of Chemical Physics*, 53:4015, 1970.

[90] D. Van Der Spoel, E. Lindahl, B. Hess, G. Groenhof, A.E. Mark, and H.J.C. Berendsen. Gromacs: fast, flexible, and free. *Journal of computational chemistry*, 26(16):1701, 2005.

[91] C. Vega, E. Sanz, and JLF Abascal. The melting temperature of the most common models of water. *The Journal of chemical physics*, 122:114507, 2005.

[92] J. Walton, DJ Tildesley, JS Rowlinson, and JR Henderson. The pressure tensor at the planar surface of a liquid. *Molecular Physics*, 48(6):1357–1368, 1983.

[93] F. Wang and DP Landau. Efficient, multiple-range random walk algorithm to calculate the density of states. *Physical Review Letters*, 86(10):2050–2053, 2001.

[94] Jihang Wang, Dusan Bratko, and Alenka Luzar. Probing surface tension additivity on chemically heterogeneous surfaces by a molecular approach. *Proceedings of the National Academy of Sciences*, 108(16):6374–6379, 2011.

[95] J.S. Wang and R.H. Swendsen. Transition matrix monte carlo method. *Journal of statistical physics*, 106(1):245–285, 2002.

[96] J.D. Weeks, D. Chandler, and H.C. Andersen. Role of repulsive forces in determining the equilibrium structure of simple liquids. *The Journal of Chemical Physics*, 54(12):5237, 1971.

[97] B. Widom. Some topics in the theory of fluids. *The Journal of Chemical Physics*, 39:2808, 1963.

[98] B. Widom. Phase transitions and critical phenomena. 1972.

[99] B. Widom. Potential-distribution theory and the statistical mechanics of fluids. *The Journal of Physical Chemistry*, 86(6):869–872, 1982.

[100] A.P. Willard and D. Chandler. Instantaneous liquid interfaces. *The Journal of Physical Chemistry B*, 114(5):1954–1958, 2010.

[101] L. Xu, S.V. Buldyrev, C.A. Angell, and H.E. Stanley. Thermodynamics and dynamics of the two-scale spherically symmetric Jagla ramp model of anomalous liquids. *Physical Review E*, 74(3):31108, 2006.

[102] Q. Yan and J.J. de Pablo. Fast calculation of the density of states of a fluid by monte carlo simulations. *Physical review letters*, 90(3):35701, 2003.

[103] Z. Yan, S.V. Buldyrev, N. Giovambattista, P.G. Debenedetti, and H.E. Stanley. Family of tunable spherically symmetric potentials that span the range from hard spheres to waterlike behavior. *Physical Review E*, 73(5):51204, 2006.

[104] Z. Yan, S.V. Buldyrev, N. Giovambattista, and H.E. Stanley. Structural order for one-scale and two-scale potentials. *Physical review letters*, 95(13):130604, 2005.

[105] H.A. Yu and M. Karplus. A thermodynamic analysis of solvation. *The Journal of chemical physics*, 89:2366, 1988.

[106] D.A. Zichi and P.J. Rossky. The equilibrium solvation structure for the solvent-separated hydrophobic bond. *The Journal of chemical physics*, 83:797, 1985.

[107] R.W. Zwanzig. High-temperature equation of state by a perturbation method. i. nonpolar gases. *The Journal of Chemical Physics*, 22:1420, 1954.

Vita

John R. Dowdle graduated from James E. Taylor High School in Katy, TX in 1998. He completed a Bachelor of Science degree from The University of Texas at Austin and a Master of Science degree from Stanford University (both in Chemical Engineering) before enrolling in the Ph.D. program in the Department of Chemical Engineering at UT Austin in the fall of 2005.

This dissertation was typeset with LaTeX[†] by the author.

[†]LaTeX is a document preparation system developed by Leslie Lamport as a special version of Donald Knuth's TeX Program.